

การจัดเรียงตัวใหม่บริเวณผิวของผลึกซิลิคอนในระนาบ (001) แบบ c(4×4)

นางสาวรัชฎาภรณ์ ทรัพย์เรืองเนตร

วิทยานิพนธ์นี้เป็นส่วนหนึ่งของการศึกษาตามหลักสูตรปริญญาวิทยาศาสตรมหาบัณฑิต

สาขาวิชาฟิสิกส์

มหาวิทยาลัยเทคโนโลยีสุรนารี

ปีการศึกษา 2549

ISBN 974-533-606-8

Si(001)-c(4×4) SURFACE RECONSTRUCTION

Ratchadaphon Sabrueangnet

A Thesis Submitted in Partial Fulfillment of the Requirements for the

Degree of Master of Science in Physics

Suranaree University of Technology

Academic Year 2006

ISBN 974-533-606-8

Si(001)-c(4×4) SURFACE RECONSTRUCTION

Suranaree University of Technology has approved this thesis submitted in partial fulfillment of the requirements for a Master's Degree.

Thesis Examining Committee

(Assoc. Prof. Dr. Prapun Manyum)

Chairperson

(Asst. Prof. Dr. Prayoon Songsiriritthigul)

Member (Thesis Advisor)

(Dr. Saroj Rujirawat)

Member

(Dr. Hideki Nakajima)

Member

(Assoc. Prof. Dr. Saowanee Rattanaphani)

Vice Rector for Academic Affairs

(Assoc. Prof. Dr. Sompong Thammathaworn)

Dean of Institute of Science

รัฐภาภรณ์ ทรัพย์เรืองเนตร : การจัดเรียงตัวใหม่ของผิวของผลึกซิลิคอนในระนาบ
(001) แบบ c(4×4) (Si(001)-c(4×4) SURFACE RECONSTRUCTION)
อาจารย์ที่ปรึกษา: ผู้ช่วยศาสตราจารย์ ดร.ประยูร ส่งศิริฤทธิกุล, 120 หน้า.
ISBN 974-533-606-8

ในงานวิทยานิพนธ์นี้ ได้มีการศึกษาพื้นผิวของซิลิคอนชนิด (001) บนผิวหน้าที่มีการจัดเรียงตัวใหม่แบบ c(4×4) โดยใช้เทคนิคการเลี้ยวเบนของอิเล็กตรอนพลังงานต่ำ เทคนิคไอเจอร์อิเล็กตรอนสเปกโทรสโกปี เทคนิคโฟโตอิมิตชันสเปกโทรสโกปีโดยใช้แสงซินโครตรอน และการคำนวณแบบ *ab initio* โดยอาศัยทฤษฎีฟังก์ชันแนลความหนาแน่น พบว่าพื้นผิวของซิลิคอนชนิด (001) บนผิวหน้าที่มีการจัดเรียงตัวใหม่แบบ c(4×4) จะเกิดขึ้นเมื่อให้ความร้อนแก่พื้นผิวซิลิคอนที่มีการจัดเรียงตัวใหม่แบบ (2×1) ในช่วงอุณหภูมิระหว่าง 580°C ถึง 630°C ในระบบสุญญากาศระดับสูงสุด การเปลี่ยนแปลงเฟสระหว่าง (2×1) และ c(4×4) เฟส สามารถผันกลับได้ ผลจากการวัด AES ยืนยันว่าการจัดเรียงตัวใหม่แบบ c(4×4) นี้มีความสัมพันธ์กับการมีอะตอมของคาร์บอนปนเปื้อนอยู่บนพื้นผิว นอกจากนี้ผลจากการคำนวณแสดงให้เห็นว่าแบบจำลองที่น่าจะเป็นไปได้มากที่สุดสำหรับพื้นผิวที่มีการจัดเรียงตัวใหม่แบบ c(4×4) คือแบบจำลองที่ประกอบด้วยอะตอมของคาร์บอนอยู่ที่ชั้นที่ 2 ได้ผิวที่รวมตัวเป็นกลุ่มของซิลิคอนคาร์ไบด์เล็ก ๆ

สาขาวิชาฟิสิกส์
ปีการศึกษา 2549

ลายมือชื่อนักศึกษา _____
ลายมือชื่ออาจารย์ที่ปรึกษา _____
ลายมือชื่ออาจารย์ที่ปรึกษาร่วม _____

RATCHADAPHON SAPRUEANGNET : Si(001)-c(4×4) SURFACE
RECONSTRUCTION. THESIS ADVISOR : ASST. PROF. PRAYOON
SONGSIRIRITTHIGUL, Ph.D. 120 PP. ISBN 974-533-606-8

Si(001)-c(4×4)/LEED/AES/PHOTOEMISSION/ DENSITY FUNCTIONAL
CALCULATIONS

In this thesis work, the Si(001)-c(4×4) surface reconstruction has been investigated by low-energy electron diffraction (LEED), Auger electron spectroscopy (AES), synchrotron photoemission spectroscopy (PES) and *ab initio* calculations based on density functional theory. It has been demonstrated that the Si(001)-c(4×4) surface reconstruction occurs when a clean Si(001)-(2×1) surface is heated at temperature between ~ 580°C and 630°C in ultra high vacuum environment. The transition between the (2×1) phase and the c(4×4) phase is reversible. The results of AES measurements confirm that the c(4×4) surface reconstruction is related to the presence of carbon atoms contaminating on the surface. The results from the calculations also suggest that the model consisting of carbon atoms at the second layer below the surface that form small SiC clusters is the most likely model for the c(4×4) reconstruction.

School of Physics

Academic Year 2006

Student's Signature _____

Advisor's Signature _____

Co-advisor's Signature _____

CONTENTS

	Page
ABSTRACT IN THAI.....	I
ABSTRACT IN ENGLISH.....	II
ACKNOWLEDGEMENTS.....	III
CONTENTS.....	IV
LIST OF TABLES.....	VIII
LIST OF FIGURES.....	IX
 CHAPTER	
I INTRODUCTION.....	1
1.1 Chemical and Solid State Properties of Silicon.....	1
1.2 Motivations.....	4
II THEORETICAL BACKGROUND.....	6
2.1 Electronic Structure.....	6
2.1.1 Energy Band Structure.....	6
2.1.2 Energy Band Structure of Silicon.....	12
2.2 Surface Electronic States.....	16
2.2.1 Surface and Bulk States.....	16
2.2.2 Surface of Si(001): Surface Reconstruction.....	20
2.3 Photoemission Spectroscopy (PES).....	26
2.3.1 Basic Principle.....	27
2.3.2 The Three-step Model.....	31

CONTENTS (Continued)

	Page
2.3.3 Electron Escape Depth.....	33
2.3.4 Measurement of Energy Distribution Curve.....	36
2.3.5 Angle-Resolved Photoemission.....	41
2.4 Methods of Calculation.....	47
2.4.1 Density Functional Theory.....	48
2.4.1.1 The Hohenberg-Kohn Theorem.....	48
2.4.1.2 The Single-Particle Formalism of Kohn and Sham.....	49
2.4.1.3 The Kohn-Sham Equations.....	50
2.4.1.4 The Local-Density Approximation.....	51
2.4.1.5 Generalized Gradient Approximation.....	52
2.4.1.6 Electronic Ground State.....	53
2.4.2 Pseudopotentials and The Projector-Augmented-Wave Method.....	55
2.4.2.1 Plane Waves.....	55
2.4.2.2 The Concept of Pseudopotentials.....	56
2.4.2.3 Norm-Conserving Pseudopotentials.....	59
2.4.2.4 Ultrasoft Pseudopotentials and The Projector Augmented-Wave Method.....	60
III EXPERIMENTAL.....	62
3.1 Experimental Instruments.....	62
3.1.1 Vacuum Chamber.....	62
3.1.2 Sample Holder.....	66

CONTENTS (Continued)

	Page
3.1.3 Low Energy Electron Diffraction (LEED).....	66
3.1.4 Auger Electron Spectroscopy (AES).....	69
3.1.5 Energy Analyzer.....	74
3.1.5.1 ARPES Analyzer.....	74
3.1.5.2 CLAM.....	75
3.1.6 Electron Gun.....	78
3.1.7 Ion Gun.....	78
3.1.8 Light Source: Synchrotron Radiation Source.....	79
3.2 Sample Preparation.....	79
3.3 Photoemission Measurements.....	82
3.3.1 AIPES Measurements.....	83
3.3.2 ARPES Measurements.....	83
3.4 Calculations.....	88
3.4.1 Slab-Models for Surfaces.....	88
3.4.2 Computational Details.....	90
3.4.2.1 Modeling of Si(001)-(2×1) Surface Reconstruction.....	90
3.4.2.2 Modeling of Si(001)-c(4×4) Surface Reconstruction.....	90
IV RESULTS AND DISCUSSION.....	94
4.1 Surface Reconstruction.....	94
4.1.1 Preparation of Si(001)-(2×1) Surface.....	94
4.1.2 Preparation of Si(001)-c(4×4) Surface.....	97

CONTENTS (Continued)

	Page
4.2 The Density of States (DOS).....	100
4.2.1 The Si(001)-(2×1) Surface.....	100
4.2.2 The Si(001)-c(4×4) Surface.....	103
4.3 Angle-Resolved Photoemission.....	109
4.3.1 The Si(001)-(2×1) Surface.....	109
4.3.2 The Si(001)-c(4×4) Surface.....	112
V CONCLUSION.....	114
REFERENCES.....	117
CURRICULUM VITAE.....	120

LIST OF TABLES

Table		Page
1.1	The solid state properties of silicon (Kittel, 1996). The RT and ATP denote the room temperature and atmospheric pressure, respectively.....	3
2.1	The energy levels at symmetry points as determined by Chan, Vanderbilt, and Louin (1986) (units are electron volts).....	16
3.1	Specifications of the ARUPS10 analyzer.....	75
3.2	Specifications of the CLAM2 analyzer.....	76
3.3	The machine parameters of the storages ring of the Siam Photon Source.....	81
3.4	Occupation of surface and subsurface sites identified in Fig. 3.1 by silicon or carbon atoms.....	92
4.1	Relative energies for the various configurations considered according to (3.3) in eV per c(4×4) cell.....	105

LIST OF FIGURES

Figure		Page
2.1	Schematic illustration of energy band.....	9
2.2	The energy band diagram of (a) metal, (b) semiconductor and (c) insulator.....	10
2.3	Calculated electronic densities of states compared to experiment for bulk Si.....	13
2.4	Bulk band structure of calculated by the full self-consistent LCAO approach and the variational LCAO approach.....	15
2.5	Sketch of a bulk and a surface state wave-function close to the surface (at $z=0$).....	18
2.6	Schematic illustration of the surface energy bands (upper panels) and the surface eigenfunctions (lower panels).....	21
2.7	LDA surface band structure of the Si(001)-(2×1) surface.....	22
2.8	Superpose surface Brillouin zones (SBZ) in the repeated zone scheme of the two (2×1) reconstructed domains of the Si(001) surface.....	23
2.9	Top and side views of (a) an ideal Si(001) surface, (b) Symmetric dimer model, and (c) asymmetric dimer model.....	25
2.10	Optimal surface structure of the Si(001)-(2×1) surface.....	25
2.11	Schematic diagram of spin and angle-resolved photoemission.....	29
2.12	The three-step model of photoemission.....	32
2.13	Momentum relations at the solid-vacuum interface.....	32

LIST OF FIGURES (Continued)

Figure		Page
2.14	The mean free path or escape depth of the electrons in solid.....	35
2.15	Relation between the kinetic energy of a photoelectron in vacuum and that in the field of an electrostatic energy analyzer.....	38
2.16	Schematic illustration of photoelectron EDC, corresponding energy levels and the DOS curve.....	40
2.17	Concept of angle-resolved photoemission.....	42
2.18	Energy dispersion in the nearly free electron model for photoelectrons in ARPES.....	46
2.19	Real wave-function ψ and pseudo-wave function ϕ of an electron in a solid.....	58
3.1	Photoemission system shown above in an experimental station of the BL-4 beamline.....	64
3.2	Schematic diagram of the photoemission system.....	65
3.3	The sample holder with thermocouple lines.....	67
3.4	Schematic diagram of rear view LEED setup.....	68
3.5	Decay of a core-hole by x-ray emission or the Auger process.....	70
3.6	Schematic energy level diagram illustrating the origin of the Auger effect.....	72
3.7	Auger spectrum from LVV Si in differential spectrum.....	73
3.8	Schematic diagram of CLAM2 with an electrostatic lens.....	77
3.9	The magnet arrangement of the storage ring of the Siam Photon Source.....	80

LIST OF FIGURES (Continued)

Figure	Page
3.10	Schematic diagram of AIPES measurements set-up..... 84
3.11	Azimuthal and polar rotation and translation movement of the sample controlled by manipulator.....86
3.12	Surface Brillouin zone of the two (2×1) reconstructed domains of the Si(001) surface..... 87
3.13	A schematic diagram of a supercell used to model a silicon surface..... 89
3.14	Top view of c(4×4) unit cell of the dimer-reconstructed Si(001)..... 93
4.1	Auger spectrum from LVV Si in differential spectrum. (a) Contaminated surface and (b) Clean surface..... 95
4.2	(2×1) low energy electron diffraction (LEED) pattern of Si(001) surface (a) Contaminated surface. (b) Clean well-defined surface..... 96
4.3	LEED pattern obtained at 65 eV from Si(001)-c(4×4) by annealing at 630°C for 5 minutes..... 98
4.4	LEED pattern obtained at 50 eV from Si(001)-(2×1) by annealing at 670°C for 5 minutes..... 98
4.5	Auger spectrum of Si(001)-(2×1) with a small carbon peak at around 270 eV has been taken after annealing after annealing at 630°C for 5 min..... 99
4.6	EDC's showing the change in the spectral shapes of Si(001)-(2×1) the valence band as the excitation photon energy is changed..... 101

LIST OF FIGURES (Continued)

Figure	Page
4.7	Calculated density of states compared to $h\nu = 60$ eV photoelectron energy distribution for Si(001)-(2×1)..... 102
4.8	EDC's showing the change in the spectral shapes of Si(001)-c(4×4) the valence band as the excitation photon energy is changed..... 106
4.9	Relaxed geometries (top views) of the configurations discussed in Chapter III..... 107
4.10	Relative surface energies of the considered structures as a function of the C chemical potential, as derived from the ab initio calculation at zero temperature..... 108
4.11	Angle-resolved photoemission spectra of Si(001)-(2×1) for angles of electron emission between 0° and 30°..... 110
4.12	Calculated surface band structure of Si(001)-(2×1)..... 111
4.13	Angle-resolved photoemission spectra of Si(001)-c(4×4) for angles of electron emission between 0° and 30°..... 113

CHAPTER I

INTRODUCTION

1.1 Chemical and Solid State Properties of Silicon

Silicon is an intrinsic semiconductor. The electron configuration of atomic Si is $[\text{Ne}] 3s^2 3p^2$ where $[\text{Ne}]$ represents the electron configuration of Ne. The Ne atom has a closed shell structure $1s^2 2s^2 2p^6$. In condensed matter, the electronic state is described by the energy band picture. In case of Si, the average electron configuration of an atom is $[\text{Ne}] 3s^2 3p^2$. Two valence electrons are in the 3s state and two valence electrons are in the 3p state. The valence state is totally formed by 4 electrons and they are well localized around the ionic core.

On the conventional hand, silicon is a nonmetal; it forms a bond with a metal (ionic bond) or with another nonmetal (covalent bond). In a crystal of pure silicon, there is a regular diamond lattice with the lattice constant of 5.43 Å. The solid state properties of Si are summarized in Table 1.1. Every atom in the crystal has four valence electrons. Since Fermi level locates in energy band gap, silicon behaves like an insulator at low temperatures. Silicon forms compounds with halogens and dilute alkalis. Silicon dioxide is a very common compound of silicon. High temperature makes silicon reactive with other materials. Silicon is acid-resistant substance except hydrofluoric (HF) acid. Silicon is used to make many electronic devices, such as transistors, integrated circuits, computer chips and solar cells because it is a good semiconductor. Silicon materials can be used at around high temperatures because of

its high melting point. It is used to make concrete and bricks, as a lubricant and for silicone implants. Silicon plastic is used for artificial skin grafts to protect healing skin. Silicones are products of silicon, made by hydrolyzing a silicon organic chloride. Silica (sand) is the main ingredient of glass, and is also found in the human skeleton. Silica and silicates are used in the manufacturing of cement, porcelain, glass, and glazes. A silica gel is obtained by taking out water from a precipitate of silicic acid. The gel absorbs water and is used to dry and remove the color from objects. Silicon monoxide is widely used as a protective coating on the surfaces of materials. Silicon is also used in the steel industry (silicon steel alloys). Silicon steel contains approximately 2.5-4.0% silicon compared to normal steel that has less than 0.03% silicon. Silicon is also used as an alloy in brass, bronze, and copper.

Table 1.1 The solid state properties of silicon (Kittel, 1996). The RT and ATP denote the room temperature and atmospheric pressure, respectively.

Properties	Reported Value
Crystal structure (RT)	Diamond
Lattice parameter (RT)	5.43 Å
Atomic number	14
Electron configurations	[Ne] 3s ² 3p ²
Density (RT, ATP)	2.33 g cm ⁻³
Atomic concentration (RT, ATP)	5.0 × 10 ²² cm ⁻³
Nearest-neighbor distance (RT, ATP)	2.35 Å
Cohesive energies (0K, 1 ATM)	446 kJ/mol, 4.63 eV/atom
Melting points	1687 K
Isothermal bulk modulus	0.988 × 10 ¹¹ N/m ²
Ionization energy (one electron)	8.15 eV

1.2 Motivations

The position of the atoms at the surface of material is one of the most basic questions among those who are interested in surface science. The atomic geometry is an important factor affecting the various behaviors of the surface such as chemical reactivity, surface energy, surface work functions, surface vibrations, and surface electronic states. With the advent of ultra-high vacuum technology and the development of experimental methods sensitive to the surface atomic structure, it became apparent that the arrangement of atoms at the surface of single-crystalline material are often different from those in the bulk and can be much complicated. The rearrangement of atoms at the surface, called surface reconstructions, is driven by the tendency of the surface to reform bonds broken by the formation of the surface. However, such atomic rearrangement often occurs at the expense of disruption of the bulk bonding and the creation of surface stresses. Such a surface reconstruction gives us information of the microscopic interactions at the surface. Our understanding of surface structures is intimately connected with our understanding of the microscopic behavior of the surface.

The Si(001) surface is of considerable technological interest since Si(001) wafers have been used for fabrications of most VLSI semiconductor devices. The atomic structure of the clean Si(001) surface has been attracted from experimental and theoretical point of view, because (2×1) structure was found in spite of (1×1) structure on the (001) surface. In addition, other phases were also found on Si(001), depending on sample treatment. A $c(4\times 2)$ phase can be produced by very slow cooling of the sample. The $p(2\times 2)$ phase was observed after high-temperature annealing of the sample. These various reconstructions of the Si(001) surface are due to dimerization of

the atoms in the first layer. The change from the well-known $c(2\times 4)$ or $p(2\times 2)$ reconstructions of the pure Si surface to the $c(4\times 4)$ pattern, with four dimers per unit cell, takes place after carbon deposition at 600°C . In order to explain the transformation above, the following questions must be elucidated: (i) What is the profile of C atoms in the surface and sub-surface layers? (ii) Do C atoms form C-C dimers on the surface or just Si-C dimers? (iii) Are there any defects, such as missing dimers involved in the picture? (iv) Do C atoms form particular complexes? (v) Do C atoms participate directly in the reconstruction? Regarding the last issue, published data (Miki and Sakamoto, 1997; Jemander, Zhang, Uhrberg, and Hansson, 2002) suggest that the $c(4\times 4)$ phase forms even at very low C contents, below 0.1 monolayer (ML) coverage, corresponding to less than one C atom per $c(4\times 4)$ unit cell. This means that C does not participate in the reconstruction with a periodic order, but that it can induce the $c(4\times 4)$ pattern through the strain field produced by its incorporation.

In this thesis work, the $c(4\times 4)$ reconstruction of a Si(001) surface has been studied. The technique to form Si(001)- $c(4\times 4)$ reconstruction has been established at the Siam Photon Laboratory. Different surface sensitive measurement techniques have been performed *in situ* to investigate the arrangement of atoms at the surface. The electronic structure of the reconstructed surface has also been studied by means of photoemission and calculations based on density functional theory (DFT). A complete set of various chemical and structural data is combined with *ab initio* calculations.

CHAPTER II

THEORETICAL BACKGROUND

This chapter provides the necessary background knowledge such as the electronic structures of both the bulk and surface, the theoretical aspects of photoemission spectroscopy (PES) and angle-resolved photoemission spectroscopy (ARPES), and the method of surface calculation.

2.1 Electronic Structure

2.1.1 Energy Band Structure

In solid state physics, the electronic band structure (or simply band structure) of a solid is made of the series of “forbidden” and “allowed” energy bands. The band structure determines various properties of materials such as electronic properties, optical properties, and magnetic properties. The energy states of semiconductor are well approximated by the energy-band picture. There are many atoms in a crystal and accordingly there are many electrons there. Electrons feel attractive forces from ionic cores and repulsive forces from other electrons. This is because there are many particles and the complicated interactions. Such complicated interactions, however, in principle can be simplified to a one particle potential model. Suppose one electron in crystal sees these averaged potential, $V(\mathbf{r})$, for which \mathbf{r} is the electron coordinate. Then $V(\mathbf{r})$ has the periodicity of the crystal lattice, since the atoms are aligned regularly in crystal. Therefore we have

$$V(\mathbf{r}) = V(\mathbf{r} + \mathbf{a}). \quad (2.1)$$

Here, \mathbf{a} is a lattice translation vector. The solution of the Hamiltonian equation with the potential given in (2.1) is given as

$$E = E_n(\mathbf{k}) \quad (2.2)$$

$$\psi_{n\mathbf{k}}(\mathbf{r}) = e^{i\mathbf{k}\mathbf{r}} u_{n\mathbf{k}}(\mathbf{r}). \quad (2.3)$$

Here n is a quantum number assigning the state and \mathbf{k} is the electron wave vector, defined as

$$\begin{aligned} \mathbf{k}_x &= \frac{\pi}{2a_x} \left(\frac{l}{N} \right) \\ \mathbf{k}_y &= \frac{\pi}{2a_y} \left(\frac{m}{N} \right) \\ \mathbf{k}_z &= \frac{\pi}{2a_z} \left(\frac{n}{N} \right). \end{aligned} \quad (2.4)$$

Here, a_x, a_y, a_z are lattice constants; l, m, n are integers in the range

$$-N \leq l, m, n \leq N. \quad (2.5)$$

The reciprocal lattice vector, \mathbf{K} , are defined as

$$\mathbf{K} = \left(\frac{\pi}{a_x}, \frac{\pi}{a_y}, \frac{\pi}{a_z} \right). \quad (2.6)$$

E and $\psi_{n\mathbf{k}}(\mathbf{r})$ are periodic in the \mathbf{k} space as

$$E_n(\mathbf{k}) = E_n(\mathbf{k} + \mathbf{K}) \quad (2.7)$$

$$\psi_{n\mathbf{k}}(\mathbf{r}) = \psi_{n\mathbf{k}+\mathbf{K}}(\mathbf{r}). \quad (2.8)$$

The eigenfunction given as (2.3) is called the Bloch function. Since N is a large number, \mathbf{k} is practically continuous. For a given n , $E_n(\mathbf{k})$ distributes in a range with a

width. Thus, $E_n(\mathbf{k})$ is referred to as the energy band. In case where we draw $E_n(\mathbf{k})$ as a function of \mathbf{k} , the curve is referred to as the energy band dispersion curve or just dispersion curve. The dispersion curves are illustrated schematically in Fig. 2.1. Drawing the energy dispersion curves for various n is called the energy-band mapping. Bloch functions can be assembled into localized wave packets to represent electrons that propagate freely through the potential field of the ion cores. Therefore it includes implicitly the state where the charge is fluctuating at a lattice site.

Electrons occupy an energy band successively from the low energy to the high energy. One \mathbf{k} site is occupied by two electrons with opposite spins. If a band is filled with electrons completely and the bands above it are completely empty, the corresponding material is an insulator. If a band is filled up with electrons partially and the level above it is empty, the material is a metal. The highest level of a band filled with electrons is called the Fermi level. In an insulator, the Fermi level is located in the band gap. If the band gap of a material is very narrow, typically a few eV, the material is called as semiconductor. The location of the Fermi level of a semiconductor in the band gap is determined by the locations of the levels of impurities such as donors and acceptors. The locations of the Fermi levels in three types of the solids are shown in Fig. 2.2. In the figure, shaded area represents the band occupied by electrons.

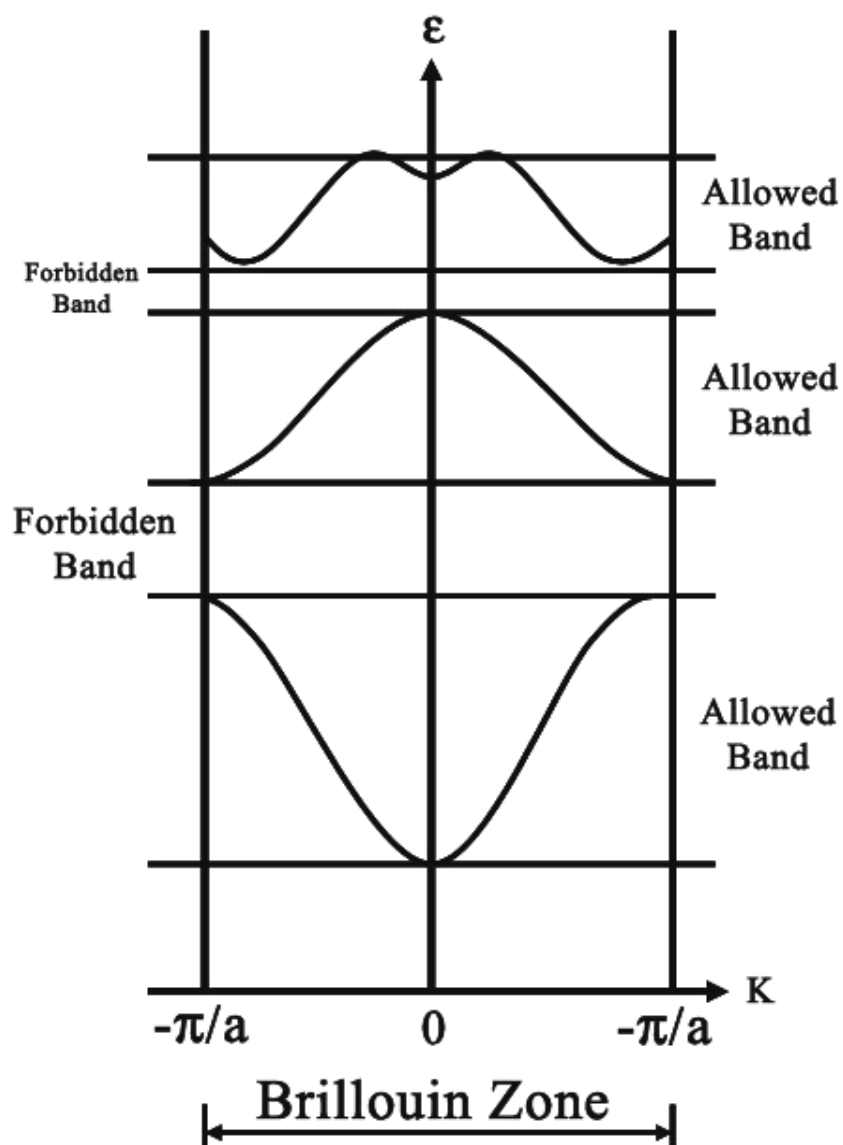


Fig. 2.1 Schematic illustration of energy bands.

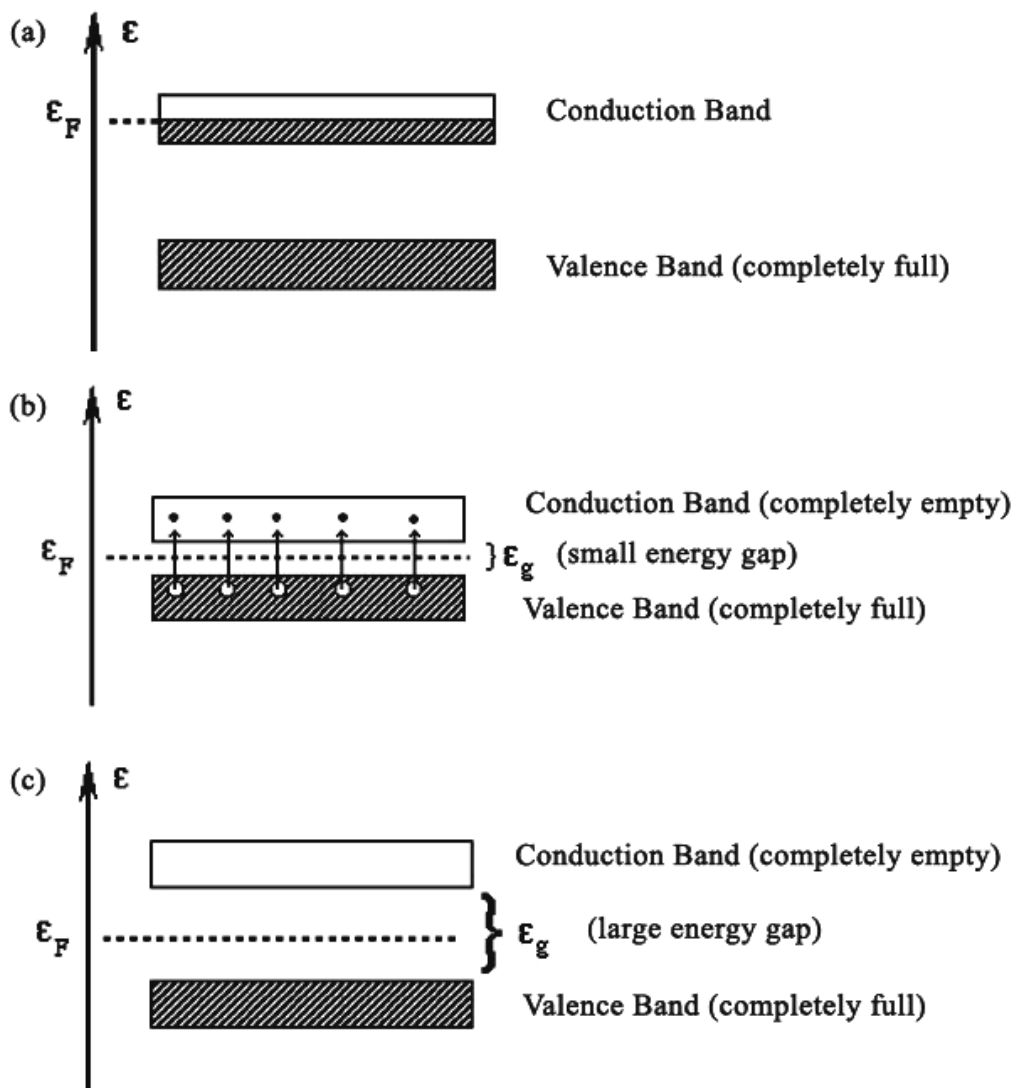


Fig. 2.2 The energy band diagram of (a) metal, (b) semiconductor and (c) insulator.

Practical calculation to obtain $E(\mathbf{k})$ is performed by several methods based on various approximations. Some approximations are very useful in understanding the essence of the energy band, although they are not used in practical calculations. One extreme case is the tight binding approximation. In this approximation, we take electrons to be bound at lattice sites and approximate the Bloch function with linear combination of atomic orbitals. Another extreme is the nearly free electron approximation where the Bloch function is formed by plane waves with different wave vectors. Better approximations were proposed such as the orthogonalized plane wave (OPW) method, the augmented plane wave (APW), and the Green function method. In order to introduce the effect of the correlation interaction, a method called $X\alpha$ method has been proposed and used. Recently, the method called the density functional calculation is quite popular. Now, the capacity and the speed of computers are quite large and high. Thus, it is possible to calculate the energy bands and associated Bloch functions with high accuracy.

An important quantity describing the energy states of solid materials is the density of states (DOS). DOS indicates the number of states in the unit energy range. This is obtained by summing up all possible states in the energy range from E to $E + dE$ and dividing the sum by dE . The relation is given as

$$D(E)dE = \frac{2}{(2\pi)^3} \int \int_E^{E+dE} d\mathbf{k} \quad (2.9)$$

$$= \frac{2}{(2\pi)^3} \int \int_E \frac{dS}{|\nabla_{\mathbf{k}} E(\mathbf{k})|}, \quad (2.10)$$

where $D(E)$ is DOS. The surface integration is carried out on the surface of a given constant energy. When the energy band calculation is made, DOS is calculated

numerically using (2.10). An example of calculated DOS curve as compared with measured photoelectron energy distribution curve for Si is shown in Fig. 2.3 (Chelikowsky and Cohen, 1976).

An important way for investigating the validity of the energy-band calculation is to compare the calculated results with those of photoemission. The partial DOS with specific orbital symmetry is proportional to the photoemission intensity as

$$N(\varepsilon_B) = A\rho_l(\varepsilon_B) \quad (2.11)$$

Also the binding energy of a peak observed in angle-resolved EDC represents the energy difference between two different energy-bands.

As shown in Fig. 2.3, the calculated DOS does not really match with the experimental photoemission data. The figure indicates some intrinsic discrepancy, in addition to the low experimental resolution, photon broadening and lifetime broadening. This suggests that more complicated calculation methods and still need to agree with experimental results.

2.1.2 Energy Band Structure of Silicon

Calculated energy band structure of Si

The calculated energy band structure of the Si has extensively been performed (Cardona and Pollak, 1966; Chelikowsky and Cohen, 1976, Chan, Vanderbilt, and Louie, 1986; Rohlfing, Krüger, and Pollmann, 1993). The calculations cover not only the bulk band structure but also the surface band structure. As an example the $E(\mathbf{k})$ curves calculated by Chan, Vanderbilt, and Louie (1986) using the wave functions formed by the linear combination of atomic orbitals (LCAO) are shown in Fig. 2.4.

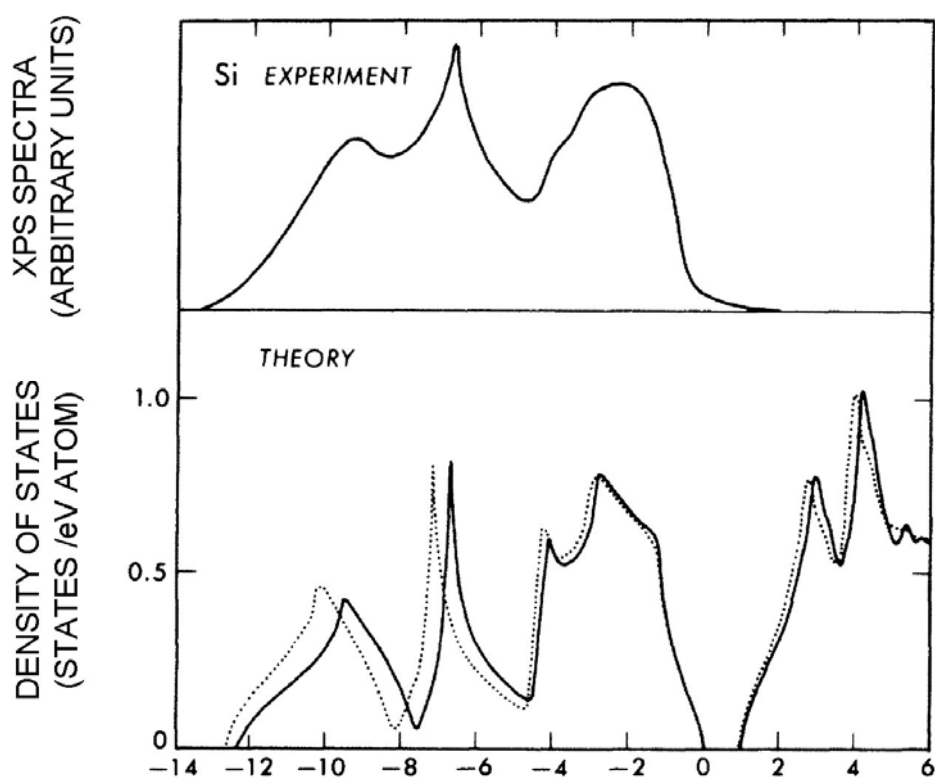


Fig. 2.3 Calculated electronic densities of states compared to experiment for bulk Si.

The experiment results was measured by Grobman and Eastman (1972). The two results are displayed: nonlocal pseudopotential (solid line) and local pseudopotential (dashed line).

For a LCAO basis set in general, they have a Bloch sum of atomic-like orbitals localized on the atomic sites of the form:

$$\phi_i(\mathbf{k}, \mathbf{r}) = \frac{1}{\sqrt{\Omega}} \sum_{\mathbf{R}} e^{i\mathbf{k} \cdot (\mathbf{R} + \boldsymbol{\tau}_i)} f_i(\mathbf{r} - \mathbf{R} - \boldsymbol{\tau}_i), \quad (2.12)$$

where Ω is the crystal volume, \mathbf{R} is a lattice vector, $\boldsymbol{\tau}_i$ is a basis vector, and f_i is a localized function. Using (2.11), the atomic orbitals are given by

$$f_{alm}(\mathbf{r}) = A_{alm} e^{-\alpha r^2} K_{lm}(r, \theta, \phi), \quad (2.13)$$

where A_{alm} is normalization constant, the K_{lm} 's (up to $l=2$) have the form $\{1, x, y, z, x^2, y^2, z^2, xy, yz, zx\}$ and the function $f(\mathbf{r})$ is normalized according to

$$\int f(\mathbf{r})^2 d^3r = 1. \quad (2.14)$$

The solid lines in Fig. 2.4 correspond to the fully self-consistent results and the dashed lines correspond to the variational results. Band energies at high-symmetry \mathbf{k} points calculated by the pseudopotential plane-wave (**PW**) method are also marked (as dots) in Fig. 2.4 for comparison. These **PW** band energies are calculated with a very high plane-wave energy cutoff of 21.5 Ry. The band energies at high-symmetry \mathbf{k} points from the present calculation are listed in Table 2.1. They are also compared with the results from a highly converged (energy cutoff of 21.5 Ry) and a not-so-well-converged (energy cutoff of 5 Ry) **PW** calculations. However, Fig. 2.4 shows that the band structure does change as full self-consistency is included. This is not surprising since there is no variation principle for the individual Kohn-Sham eigenvalues. Comparing with the **PW** band energies in Table 2.1 and Fig. 2.4, they note that the self-consistent band structure agrees very well with the high-cutoff **PW** result.

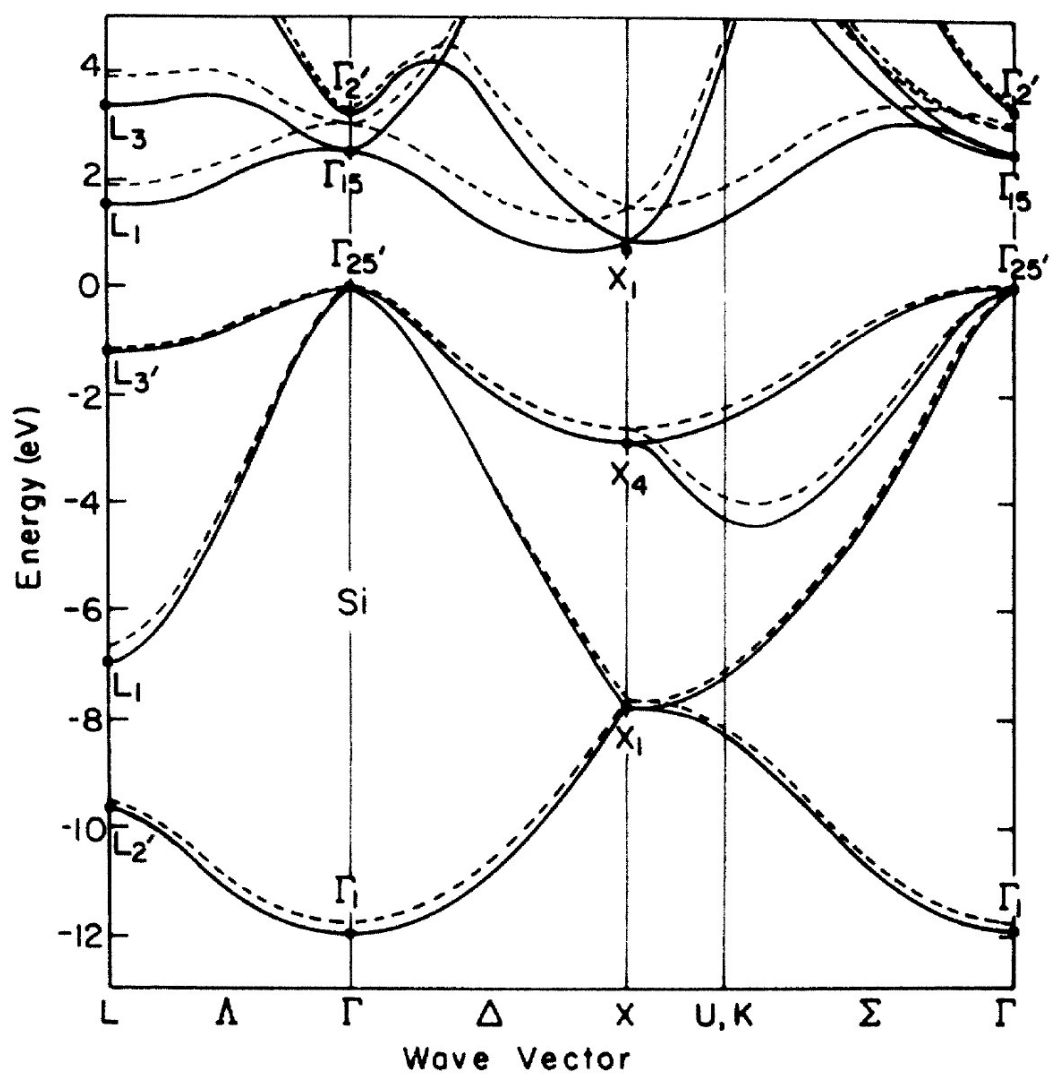


Fig. 2.4 Bulk band structures calculated by the full self-consistent **LCAO** approach (solid lines) and the variational **LCAO** approach (dashed lines). (Chan, Vanderbilt, and Louie, 1986)

Table 2.1 The energy levels at symmetry points as determined by Chan, Vanderbilt, and Louie (1986) (units are electron volts).

	Variational LCAO	Fully self-consistent LCAO	PW $E_{\text{cut}}=21.5$ Ry	PW $E_{\text{cut}}=5$ Ry
Γ_{1v}	-11.73	-11.99	-11.91	-11.21
Γ'_{25v}	0.0	0.0	0.0	0.0
Γ_{15c}	3.00	2.53	2.55	2.72
Γ'_{2c}	3.35	3.21	3.28	5.62
X_{1v}	-7.69	-7.84	-7.76	-6.88
X_{4v}	-2.64	-2.86	-2.86	-2.80
X_{1c}	1.44	0.84	0.66	1.29
L'_{2v}	-9.50	-9.65	-9.56	-8.82
L_{1v}	-6.70	-7.00	-6.96	-6.50
L'_{3v}	-1.11	-1.21	-1.20	-1.17
L_{1c}	1.89	1.54	1.50	3.36
L_{3c}	3.89	3.38	3.33	3.79

2.2 Surface Electronic States

2.2.1 Surface and Bulk States

The energy state, which is not introduced by the adsorption of foreign atoms but is inherent to the clean surface, called the intrinsic surface state. Since atoms on the surface are arranged with two dimensional symmetry, the intrinsic surface state forms two dimensional energy bands. The wave vectors have dispersion parallel to the surface only. If foreign atoms are adsorbed on the surface, the electronic state of the surface is changed. If a kind of foreign atom forms a monolayer, then this foreign atom layer gives rise to a two dimensional energy band system. In this case, the theoretical treatment of the surface is practically the same as that of the intrinsic surface state. If the concentration of the adsorbed atoms or molecules is low and they are dispersed on the surface, their energy states are similar to those of the isolated atoms or molecules.

The wave functions at the surface, of course, have to obey the symmetry parallel to the surface but the translation invariance perpendicular to the surface is broken. This symmetry breaking can actually lead to new solutions of the Schrödinger equation. Electronic states which reside only at the surface.

A simple qualitative picture is given in the following. Consider the Bloch wave functions in the solid:

$$\psi_{\vec{k}}(\vec{r}) = u_{\vec{k}}(\vec{r}) e^{i\vec{k}\vec{r}} \quad (2.15)$$

It gives solutions which are growing without bound in the crystal. If however, only the component of \vec{k} perpendicular to the surface is non-real one can try to match the solution which is exponentially growing inside the crystal with an exponential decay outside the crystal. In this way a surface-state wave-function is created. Inside the crystal, wave function can be written as

$$\psi_{\vec{k}}(\vec{r}) = u_{\vec{k}_{\parallel}}(\vec{r}_{\parallel}) e^{i\vec{k}_{\parallel}\vec{r}_{\parallel}} e^{-\kappa r_{\perp}}, \quad (2.16)$$

outside it is exponentially decaying. We write κ instead of k_{\perp} to make it clear that we do not deal with a conventional k_{\perp} vector but with a complex one. Figure 2.5 shows such a solution. The k_{\perp} of the surface state as a rod like in the Ewald construction known from LEED.

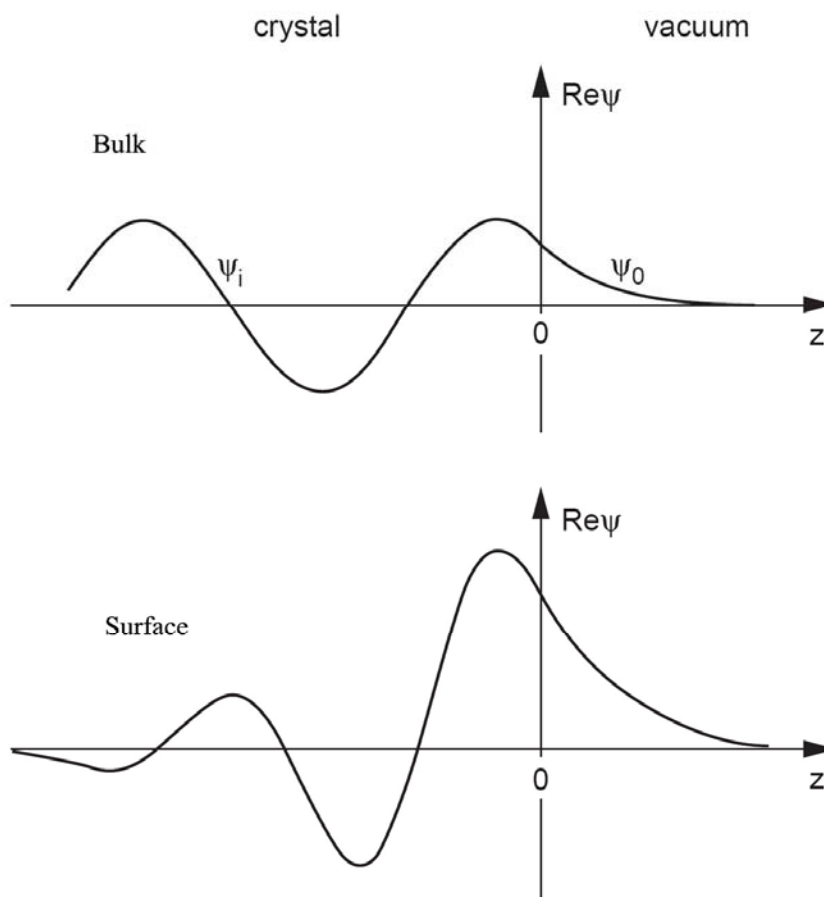


Fig. 2.5 Sketch of a bulk and a surface state wave-function close to the surface (at $z=0$). Both are matched to an exponential decay into the vacuum. The surface state also decays exponentially into the bulk.

It is important to realize that a true surface state cannot be degenerated with any bulk state. For a true surface state with $\vec{k}_{||}$ and $E(\vec{k}_{||})$ there cannot be any bulk state with the same energy and $\vec{k}_{||}$ for any value of k_{\perp} , the surface state could couple to it and penetrate infinitely into the bulk. It would not be a surface state any more. This requirement gives a necessary condition for the existence of a surface state. We can illustrate it by introducing the concept of the projected bulk band structure. Every point in the surface Brillouin zone is characterized by a $\vec{k}_{||}$. For many points along high-symmetry lines of the surface Brillouin zone is the so-called projected band structure.

If the surface energy level occurs in the band gap of the projected bulk band, the corresponding state is quite localized near the surface and the wave function decays very rapidly toward the interior of the solid as well as toward the vacuum area. The corresponding state is a bound state below the vacuum level. The energy level corresponding to this state is experimentally observable. The state is illustrated in the middle part of Fig. 2.6. This is the intrinsic surface state.

If the surface level occurs in a part within the projected bulk band, the surface state and the bulk state mix together to form a state gradually transient toward the interior of the solid. This state is referred to as the surface resonance state. This state is illustrated on the Fig. 2.6 (c).

As an example, the surface band structure of the Si(001)-(2×1), two domain reconstructed surface, as resulting from *Scattering-theoretical approach* calculations (Krüger and Pollmann, 1993), is shown in Fig. 2.7. The tilting of the dimers leads to vary significant consequences in the electronic structure of the surface. It gives rise to two distinctly different dangling bond states D_{up} and D_{down} . The

buckling decreases the energy of the D_{up} state and lifts the energy of the D_{down} state. Since D_{up} is occupied and D_{down} is empty, this energetic lowering of D_{up} leads to a lowering of the total energy.

The surface band structure of the Si(001)-(2×1), two domain reconstructed surface, exhibits a very rich spectrum of surface state bands originating from dangling bonds, dimer bonds and backbonds. The states S_1 - S_5 have backbond character and their wave functions are mostly s-like. The bands B_1 - B_5 have backbond character as well, but the related states are strongly p-like with small s and d admixtures. The surface Brillouin zones of the two (2×1) reconstructed domains of the Si(001) surface is shown in Fig. 2.8.

2.2.2 Surface of Si(001): Surface Reconstruction

Electrons in the surface layer see the potential different from electron in the bulk. Similarly, the interatomic force acting on atoms in the surface layer is also differing from that in the bulk. This is due to the break of symmetry at the surface; i.e. there is no atom on the vacuum side. Thus atoms in the surface layer are arranged in a manner different from those in the layers in the bulk. The interlayer distance is also different from that in the bulk. Atoms in a solid are located at sites where the potential is at minima. Therefore, in some cases, the atomic arrangement in the surface layer is changed by heat treatment.

The change of the atomic arrangement in the surface is referred to as the surface reconstruction. In the following section, the surface reconstruction will be described in more detail.

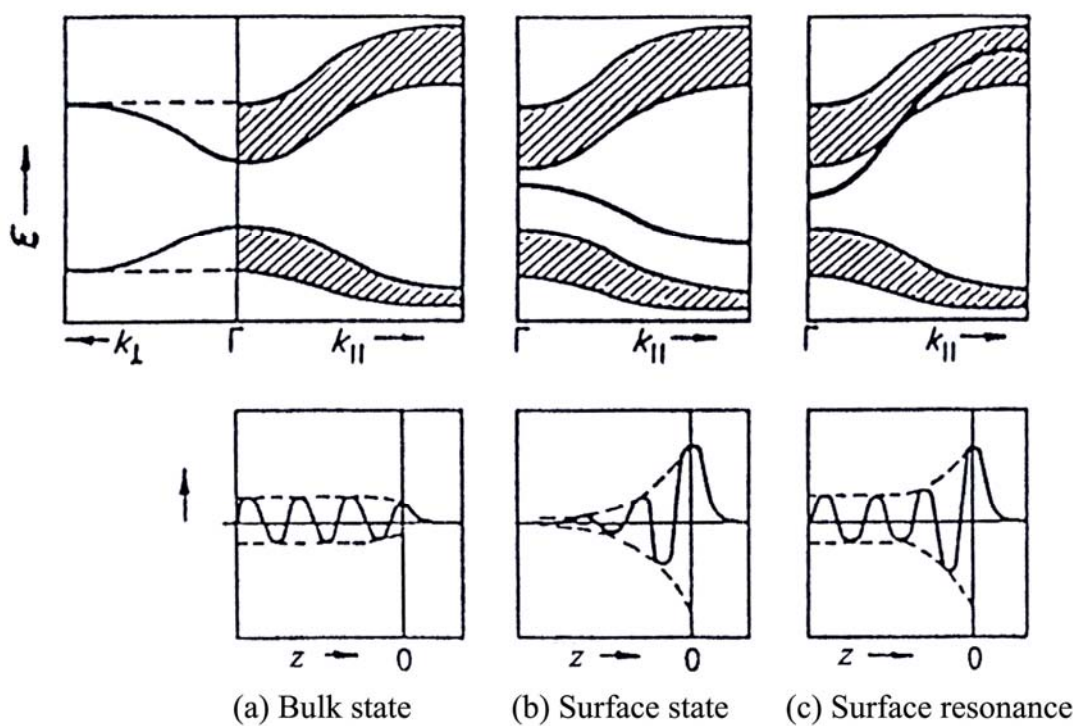


Fig. 2.6 Schematic illustration of the surface energy bands (upper panels) and the surface eigenfunctions (lower panels). The projected bulk bands (hatched part) are shown for comparison. The surface occurs at $z = 0$ (Feuerbacher and Willis, 1976).

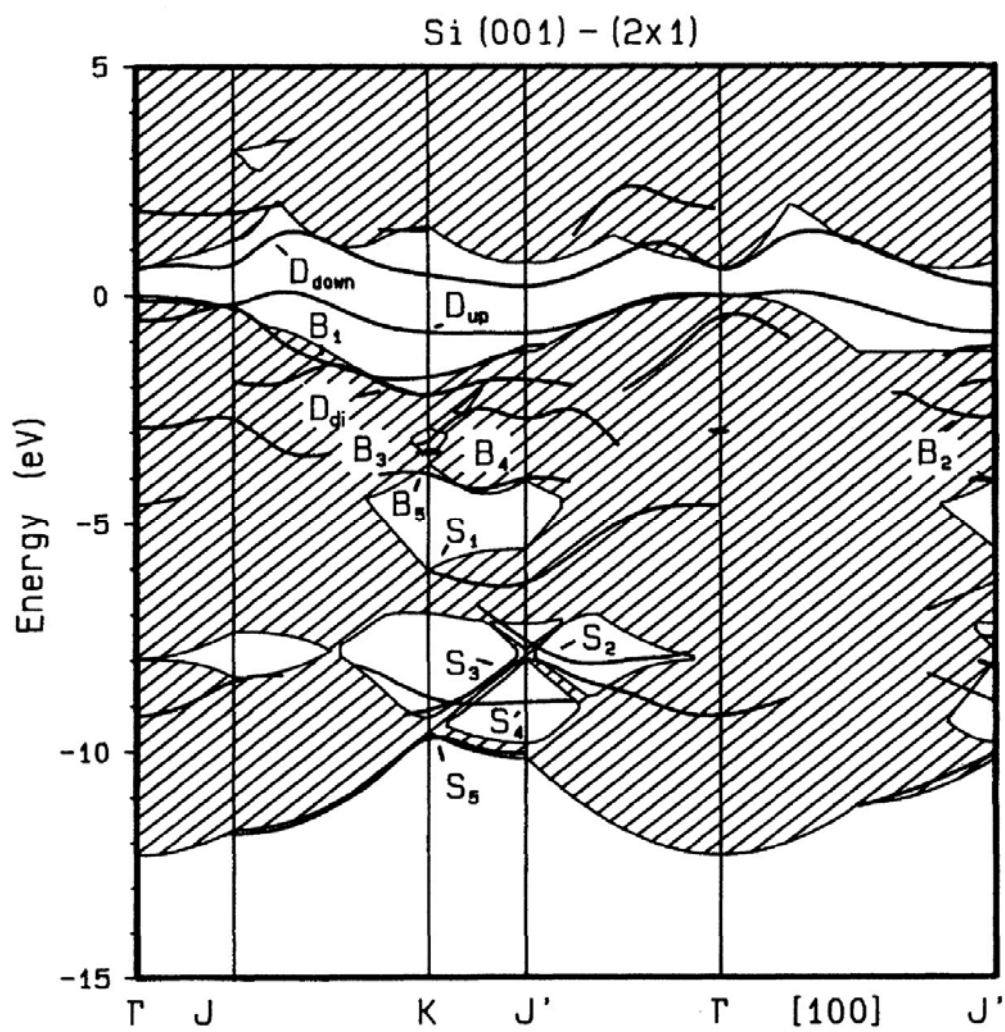


Fig. 2.7 LDA surface band structure of the Si(001)-(2x1) surface (Krüger and Pollmann, 1993).

Si (100) (2×1) two-domain
surface Brillouin zones

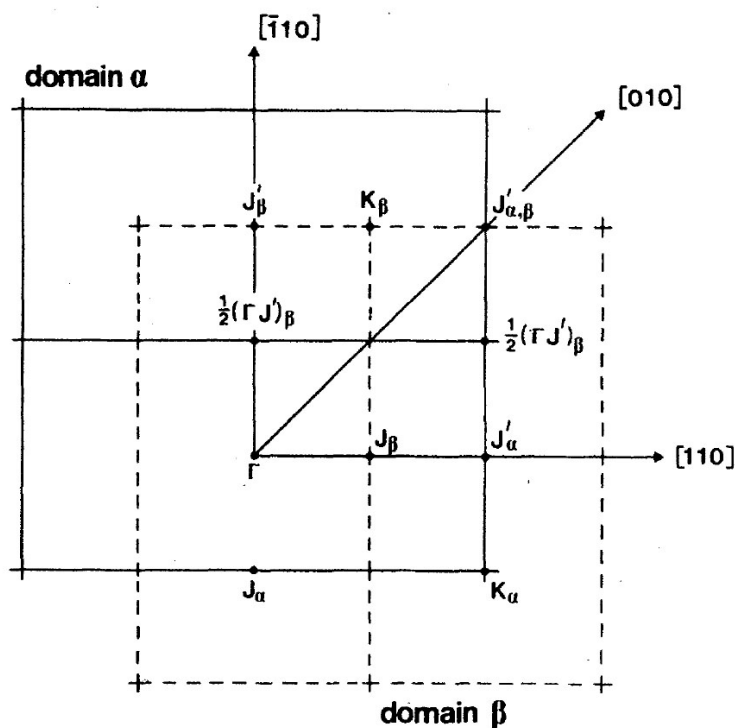


Fig. 2.8 Superposed surface Brillouin zones (SBZ) in the repeated zone scheme of the two (2×1) reconstructed domains of the Si(001) surface. The symmetry points of the (2×1) surface Brillouin zone are pointed out, with indices identifying them with domain α and domain β , respectively. The bulk azimuthal directions are also indicated. (Uhrberg, Hansson, Nicholls, and Flodström, 1981).

In a reconstruction, the atoms in the surface layers have an arrangement which is not the same as the bulk structure. Such reconstruction leads to change in the surface lattice that accompanies a change in the surface band structure, leading to the reduction of the density of states at the Fermi level. This may be understood as the surface reconstruction driven by the change in the surface state.

In case of a clean Si(001) surface, the geometrically ideal Si(001) surface is not stable. It shows a dangling-bond and bridge-bond state at each surface layer atom. The respective surface bands overlap in energy giving rise to a metallic surface. Unsaturated surface bonds are energetically unfavorable and very reactive. Their number can easily be reduced by forming surface dimers. Neighboring surface-layer atoms move towards one another until a new chemical bond is formed. These dimers form rows at the surface. In the simplest case this gives rise to a (2×1) reconstruction. The model of surface structure of Si(001) as shown in Fig. 2.9. The energy gain due to dimer formation relative to the geometrically ideal surface configuration is given by about 2 eV per dimer. The optimized structure of the Si(001)-(2×1) surface, as resulting from recent *ab initio* total energy calculations (Krüger and Pollmann, 1995; Ramstad, Brocks, and Kelly, 1995) is shown in Fig. 2.10.

The asymmetry of the dimers has two important consequences: first, the buckling opens up between the surface-induced dangling bond states yielding a semiconductor Si(001)-(2×1) surface for the asymmetric dimer model (ADM) in agreement with experiment. Second, within the symmetric dimer model (SDM), reconstructions more complex than the (2×1) cannot be explained. LEED experiments at temperatures below 200 K, however, clearly show spots that are related to c(4×2) and p(2×2) reconstructions. These higher reconstructions originate from different

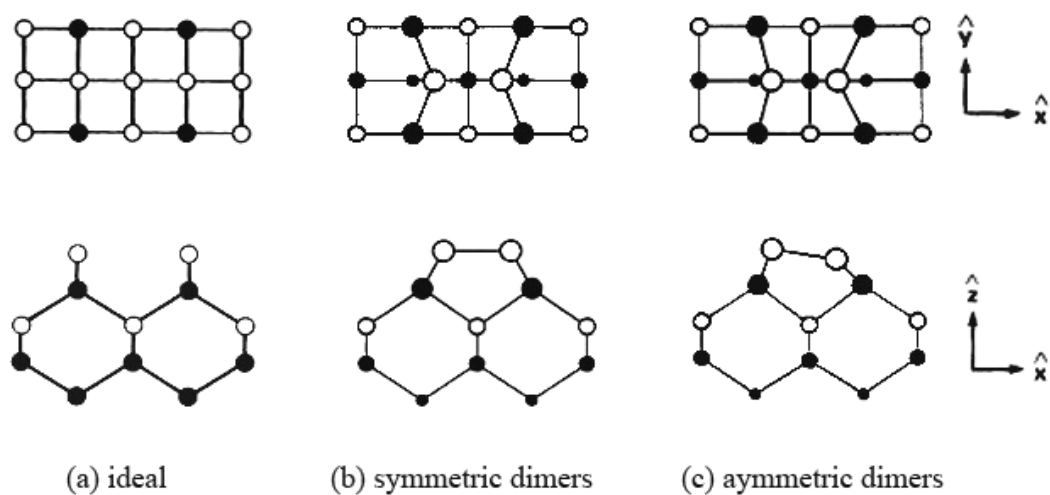


Fig. 2.9 Top and side views of (a) an ideal Si(001) surface, (b) Symmetric dimer model, and (c) asymmetric dimer model.

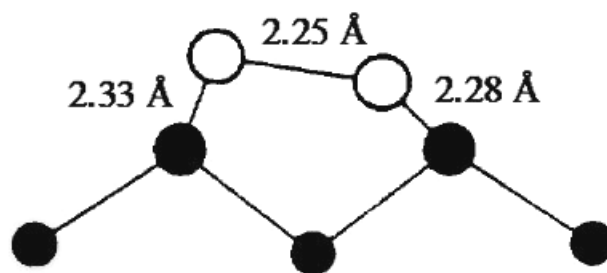


Fig. 2.10 Optimal surface structure of the Si(001)-(2×1) surface (Krüger and Pollmann, 1995).

configurations of left- and right-tilted dimers. They give an increase to small additional total energy gains of 0.05 eV per dimer from interactions between neighboring dimers in dimer row and 0.003 eV per dimer from interactions of nearest neighbor dimers in two neighboring dimer rows. It turns out that the total energy is minimal if the dimer-tilt direction alternates along and perpendicular to the dimer rows. The resulting $c(4\times 2)$ reconstruction is indeed observed at low temperatures. The related energy gain is so small, however, that the ideal $c(4\times 2)$ long range order is lost at higher temperatures.

2.3 Photoemission Spectroscopy (PES)

In this thesis, the photoemission spectroscopy technique has been used for the investigation of the electronic structure of Si(001) surface. In this section, the fundamentals of photoemission are briefly overviewed. Experimental details will be described in the next chapter.

Photoemission is widely used in the study of electronic structure of solids. It utilizes the photoelectric effect in which an electron is ejected from the occupied electron levels of the sample. In a photoemission experiment, the kinetic energy of the photoelectrons usually varies from a few electron volts up to a few hundred electron volts, depending on the photon energy used. This results in the surface sensitivity of the technique, as the inelastic mean free path of a typical photoelectron in the solid is in the range of 5-30 Å. This means that UHV is necessary to maintain a surface of adsorbates during the time scale of measurement.

Photoemission intensity gives us the information of the density of states (DOS)

as

$$n(\varepsilon_B, \nu) \propto \sigma(\nu) D(\varepsilon_B). \quad (2.17)$$

Here, $\sigma(\nu)$ is the excitation cross section at photon energy, $h\nu$. $D(\varepsilon_B)$ is DOS and ε_B is the binding energy which will be defined later.

Useful information is the energy band dispersion curve expressed as

$$\varepsilon_\alpha(\mathbf{k}_\alpha) \text{ versus } \mathbf{k}_\alpha. \quad (2.18)$$

Here, $\varepsilon_\alpha(\mathbf{k}_\alpha)$ is the energy band along a good symmetry line in the Brillouin zone.

The process of obtaining the energy band dispersion curves by photoemission is often referred to as the band mapping. Angle-resolved photoemission measurements made in the energy band mapping. The energy band mapping can be made in the spin resolved mode. However, this is not in the scope of the present thesis and its principle is not described here. Since photoelectrons have a small but tunable escape depth, it is possible to see the surface and adsorbate state as well as bulk states.

2.3.1 Basic Principle

Photoemission is the phenomenon that electrons are emitted out of matter that is exposed to light. The electrons are called *photoelectrons*. Outside the solid, electrons are easy to handle and observe. Kinetic energy, momentum and spin are measured and analyzed. For implementing these, emission angle (θ_e) and azimuthal angle (ϕ_e) of electron emission are measured as shown in Fig. 2.11. From the properties of the photoelectrons in vacuum, one can retrieve the properties of electrons inside the investigated system as described below.

(1) Energy distribution curve (EDC)

Regarding the photoemission spectrum described in (2.17), we practically measure the spectrum called the energy distribution curve (EDC). EDC is the number of primary photoelectrons, $n(\varepsilon_u, \nu) d\varepsilon$, emitted per unit time by excitation with monochromatic light with photon energy ($h\nu$).

Thus, EDC is expressed as

$$n(\varepsilon_u, \nu) d\varepsilon = \frac{N(\varepsilon_u, \nu) d\varepsilon d\nu}{I_0(\nu) d\nu} \quad (2.19)$$

$$n(\varepsilon_u, \nu) = \frac{N(\varepsilon_u, \nu)}{I_0(\nu)} \quad (2.20)$$

Here, $N(\varepsilon_u, \nu) d\varepsilon d\nu$ is the number of excited primary photoelectrons and $I_0(\nu) d\nu$ is the light intensity.

If we define the binding energy as

$$\varepsilon_B = h\nu - \varepsilon_u \quad (2.21)$$

EDC is also expressed in terms of the binding energy as

$$n(\varepsilon_B, \nu) d\varepsilon = \frac{N(\varepsilon_B, \nu) d\varepsilon d\nu}{I_0(\nu) d\nu} \quad (2.22)$$

$$n(\varepsilon_B) = \frac{N(\varepsilon_B, \nu)}{I_0(\nu)} \quad (2.23)$$

The number of photoelectrons per unit time is equivalent to photocurrents, J . Also, we measure the photocurrent in a solid angle, $d\Omega$, defined by the detector system. Thus, what we measure practically is

$$N(\varepsilon_u, \nu, \theta, \phi) d\varepsilon d\nu \frac{d\Omega}{4\pi} \quad (2.24)$$

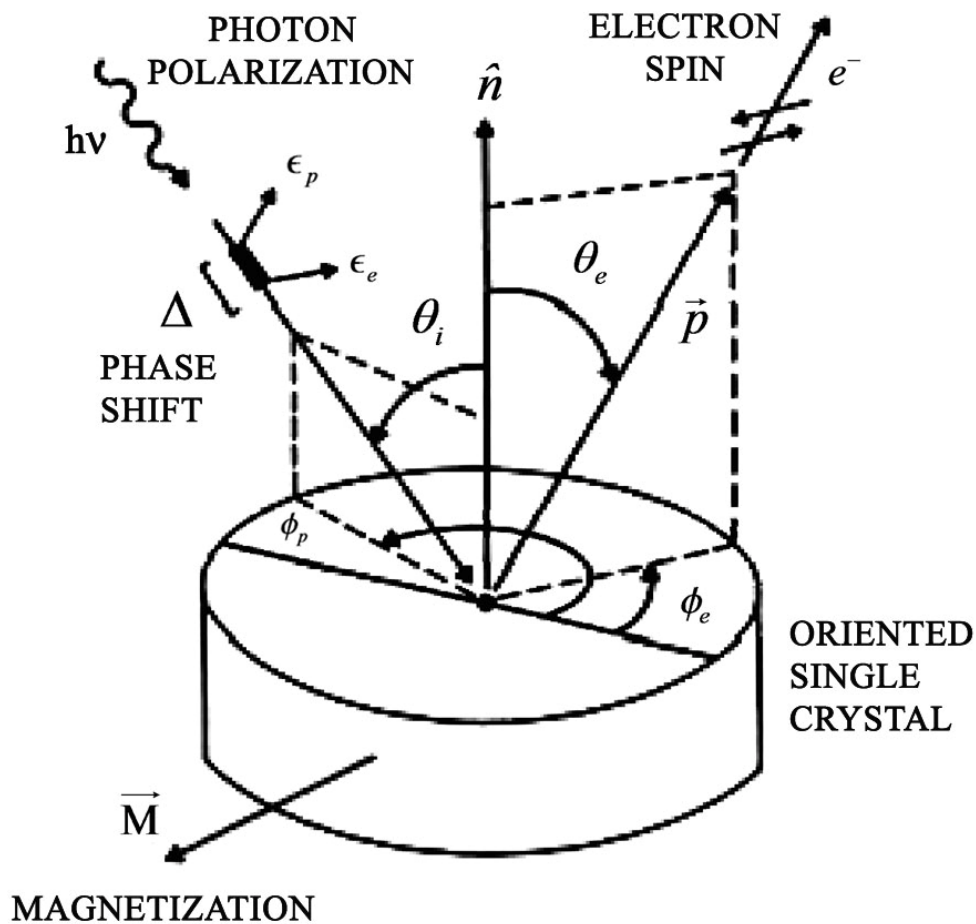


Fig. 2.11 Schematic diagram of spin and angle-resolved photoemission. This diagram is to show all the angular parameters. θ_i is the polar angle of photon incidence (incident angle). θ_e is the polar angle of photoelectron emission. ϕ_p and ϕ_e are azimuthal angles of light incidence and photoelectron emission, respectively. \mathbf{p} is the momentum of the photoelectron. \mathbf{e}_s (s-polarization) and \mathbf{e}_p (p-polarization) are electric vector components of excitation light parallel and normal to the plane of incidence, respectively.

In the actual spectrometer, we have broadening of the measured spectra owing to the overall energy resolution. Suppose the smearing of the real spectrum by resolution is given by the window function, $W(\varepsilon)$ the spectra we observe is deformed as

$$\bar{N}(\varepsilon_u, \nu, \theta, \phi) = \frac{\int_{-\infty}^{\infty} N(u, \nu, \theta, \phi) W(u - \varepsilon) du}{\int_{-\infty}^{\infty} W(u) du} \quad (2.25)$$

If we know $W(\varepsilon)$ correctly, we can deconvolute $\bar{N}(\varepsilon)$ to obtain $N(\varepsilon)$.

(2) Binding energy

We have to establish the idea with which useful pieces of information can be drawn out through the analysis of the photoemission phenomena. Many early theoretical investigations targeted this analysis.

First, consider the system consisting of N electrons. Suppose its energy is $E_g(N)$. There is a photon with an energy, $h\nu$. The system of N electrons and a photon are considered as the initial state. In the final state of the photoexcitation, the photon disappears and an electron with a kinetic energy ε_u is produced. From the energy conservation, we have

$$E_g(N) + h\nu = E_f(N-1) + \varepsilon_u \quad (2.26)$$

or,

$$h\nu - \varepsilon_u = E_f(N-1) - E_g(N) \quad (2.27)$$

From eq (2.21) can be written as

$$\varepsilon_B = E_f(N-1) - E_g(N) \quad (2.28)$$

Since $0 > E_f(N-1) > E_g(N)$, ε_B is always a positive value. It should be noted that ε_u is the kinetic energy of electron inside the sample. Thus we must find the relation between ε_u and a measurable kinetic energy of electron outside the sample.

2.3.2 The Three-step Model

An intuitive and often-used approach for photoemission is the so-called three step model. The basis for this model is illustrated in Fig. 2.12. The three steps are:

1. A photon is absorbed in the crystal by an electron. The electron is excited from an occupied initial to an unoccupied final state.
2. The excited electron is brought to the surface taking into account the direction of propagation of the final state and the mean free path.
3. Transmission of photoelectrons through the surface into vacuum.

It is important to notice that the whole system of semi-infinite solid and vacuum has a translational symmetry only parallel to the surface. Therefore the \vec{k} vector parallel to the surface $\vec{k}_{||}$ is a good quantum number and is conserved during the photoemission process.

This is not true for the perpendicular component of \vec{k} . k_{\perp} is not determined by the photoemission experiment. The most severe change in k_{\perp} happens because of the kinetic energy change which leads to a refraction at the surface barrier as shown in Fig. 2.13.

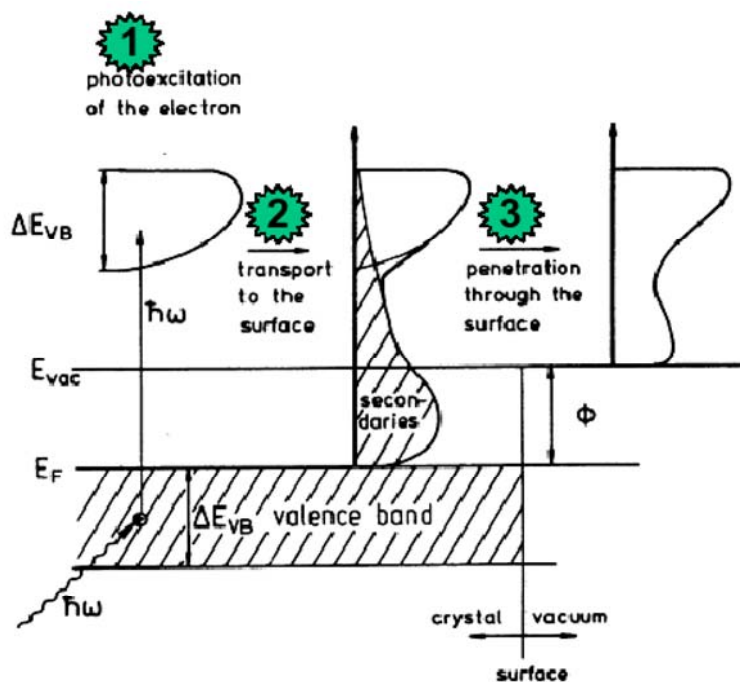


Fig. 2.12 The three-step model of photoemission: (1) photoexcitation of electrons; (2) travel to the surface with concomitant production of secondary (shaded); (3) penetration through the surface (barrier) and escape into the vacuum (Hüfner, 1996).

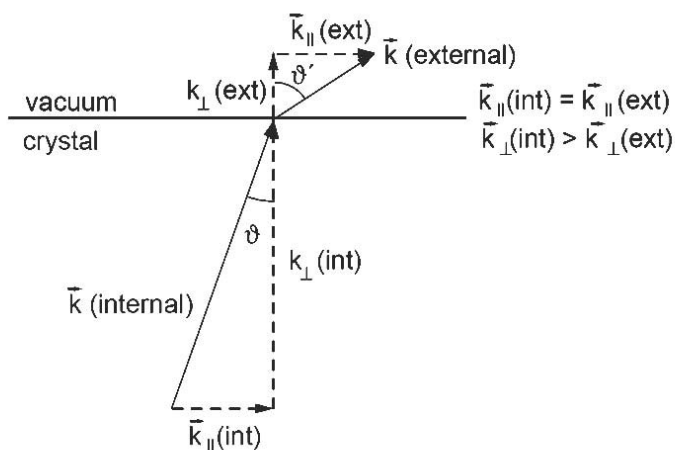


Fig. 2.13 Momentum relations at the solid-vacuum interface.

2.3.3 Electron Escape Depth

In the expression of EDC, a quasi-constant factor λ is included. This parameter is defined as the mean free path. In case of EDC, this parameter is referred to as the escape depth, the average distant that electron travels in solid without colliding with other electrons. The escape depth determines the probability for electron to be emitted from solid through the relative given below

$$N = N_0 e^{-x/\lambda} \quad (2.29)$$

Where N_0 is the number of electrons excited from the occupied state at depth x and N is the number of electron survive after traveling the distant x .

The escape depth of the electron is determined by electron-electron interaction at the energy of interest. In the present case, we are interested in kinetic energies of the electrons between about 10 and 2000 eV. The Born approximation shows that the cross-section for electron-electron scattering σ_{sc} is given by

$$\frac{d^2\sigma_{sc}}{d\Omega d\varepsilon_u} = \frac{\hbar^2}{(\pi e a_0)^2} \frac{1}{k^2} \text{Im} \left[-\frac{1}{\varepsilon(k, \varepsilon_u)} \right], \quad (2.30)$$

From (2.30) the inverse of the average escape depth λ^{-1} is obtained by integration over all energy transfers (ε_u) and momentum transfers ($\hbar k$). Thus λ^{-1} is essentially determined by the dielectric function, $\varepsilon(k, \varepsilon_u)$ which is dependent on materials. Here, ε_u is the electron energy and $\hbar k$ is its momentum. This material effect on the escape depth will be observed when the kinetic energy is comparable to the binding energy of a valence electron of ~ 10 eV. Whereas, for the $\varepsilon_u > 10$ eV, the electron in solids can be described by a free-electron gas because the binding properties are no longer

important. In this case, the inverse escape depth is described by the mean electron-electron distance r_s which is roughly equal for all materials.

Then one obtain (Hüfner, 1996),

$$\frac{1}{\lambda} \cong \sqrt{3} \frac{a_0 R}{E_k} r_s^{-3/2} \ln \left[\left(\frac{4}{9\pi} \right)^{2/3} \frac{E_k r_s^2}{R} \right] \quad (2.31)$$

where, $a_0 = 0.529 \text{ \AA}$, $R = 13.6 \text{ eV}$, and r_s is measured in units of Bohr radius a_0 . This gives us the escape depth as function of kinetic energy. The escape depth of the electrons of eq (2.31) is plotted in Fig. 2.14, the plot is called “universal curve”. The dashed curve shows a calculation of the escape depth independent of the material and the points are measured data from many element solids. Assuming that the kinetic energy of a photoelectron is not much different from the photon energy ($h\nu$), the universal curve takes its minimum of $\sim 5 \text{ \AA}$ for excitation photon energies of 50-100 eV. Hence the photoemission spectra taken at $h\nu = 50\text{-}100 \text{ eV}$ are most surface-sensitive. In this thesis, most of the experiments were carried out in the kinetic energy region between 40 and 60 eV. At these energies, the spectra are more surface sensitive. Here, we should consider the effect of the escape depth based on (2.29). Since the escape depth is 5 \AA in the energy range we are concerned with, it is much shorter than the penetration depth of light, which is in the range of $1,000 \text{ \AA}$. Therefore, we can naturally consider photoelectron as being generated uniformly in the layer near the surface. With the above-mentioned conditions, only 25% of photoelectron can escape from solid without scattering with other electron. Among these electrons, 8.3% electrons are from the first (surface) layer and 16.7% electrons are from the bulk, i.e., the layers below the second layer. Thus the ratio of the numbers of surface photoelectrons versus that of bulk photoelectrons is $4.6:3.8 = 6:5$.

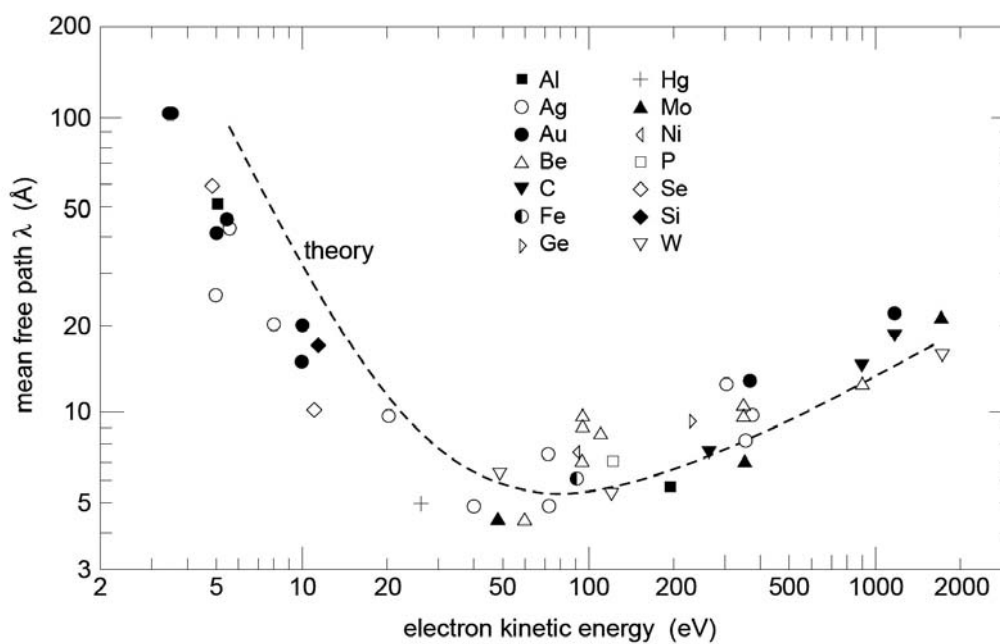


Fig. 2.14 The mean free path or escape depth of the electrons in solid. The open and close symbols represent experimental measurements and the dashed curve a calculation.

2.3.4 Measurement of Energy Distribution Curve

After simplifying assumption as the three steps model to regard the photoelectron to be retarded by the field of the electron affinity when leaves the surface and jumps deep into the vacuum. When the electron comes in the spectrometer system, the electron sees another retardation or acceleration field. From the consideration of the contact potential, it is verified that the electron comes in the spectrometer system with a kinetic energy of ε'_k given as

$$\varepsilon'_k = \varepsilon_u - \chi_s, \quad (2.32)$$

where χ_s is the work function of the spectrometer entrance point. However, the kinetic energy, ε_k of a photoelectron is assumed just to be

$$\varepsilon_k = \varepsilon_u - \chi, \quad (2.33)$$

where χ is the work function of the sample.

Electron emitted from a sample as it is irradiated with monochromatic light are collected with an electron lens, transferred to an energy analyzer and detected with an electron multiplier. As an electron jumps into an electron multiplier, the number of electrons emerging in the output of the electron multiplier is multiplied by a factor of 10^6 and pulse with measurable currents appears. A preamplifier reduces the impedance; a linear amplifies the pulse heights in an appropriate range; a counter counts the number of pulse per second. If the rate meter is inserted in a manner shown in Fig. 2.15, the number of pulse per unit time can be monitored. The number of pulsed per unit time is stored in a microcomputer. Energy analyzers are usually of the electrostatic type, where electrons are either deflected by the electrostatic field of condenser. There, only electrons with specific kinetic energy can pass though slits

after moving along the trajectory determined by the field strength. By changing the field strength, electrons are selected according to their kinetic energy. This process is called as the energy analysis. The energy analysis is made by sweeping the voltage applied to the electron lens or to the condenser. The computer controls the action of the whole system including the wavelength scanning of a monochrometer.

In Fig. 2.16, the relations among the energy levels, the DOS curve, and expected EDC are shown. On the left hand side of the figure, the energy levels are illustrated. In this part, the basic energy conservation relation expressed by (2.21) is represented. In the part adjacent to this, the energy levels are given. On the right hand side of the figure, the DOS curve associated with the energy levels are illustrated. EDC is shown there. Intrinsic EDC is accompanied by the broad background band with no structure. The background is caused by inelastic scattered electrons.

Usually, the photoelectron is retarded by lens before it enters the entrance slit of the analyzer. The relation between ε'_k and $\hat{\varepsilon}'_k$ under the presence of a retardation voltage, V_R is shown in Fig. 2.15. In Fig. 2.15, the electron lens is replaced by a retardation electrode for simplicity. In the spherical electrostatic energy analyzer, the kinetic energy of photoelectron passing through the analyzer is proportional to the voltage, V_p applied to the condenser. If the proportionality constant is referred to as α , the argument described above gives the binding energy as

$$\varepsilon_B = h\nu - \chi_s - eV_R - \alpha V_p, \quad (2.34)$$

where χ_s is the work function of the entrance aperture of spectrometer. By the simple condition of the electron motion and the application of the Gauss theorem to the analyzer, it is proved the α is given as

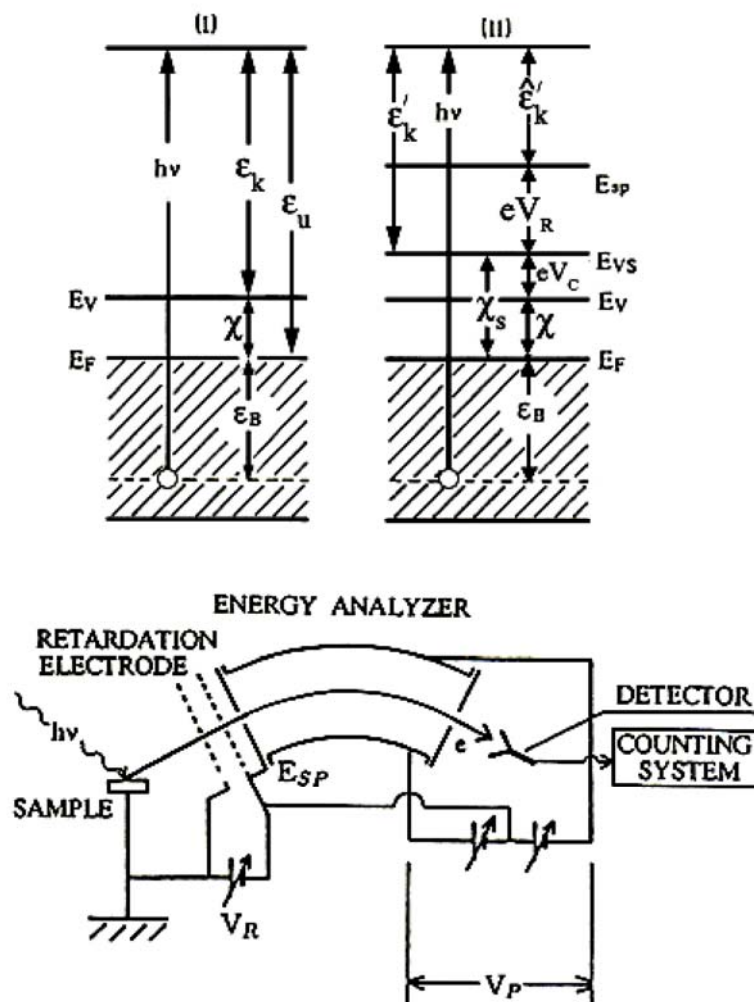


Fig. 2.15 Relation between the kinetic energy of a photoelectron in vacuum and that in the field of an electrostatic energy analyzer. (I) Energy in a sample and (II) Energy in an experiment arrangement. The part of an electron lens is illustrated as retardation electrons (Ishii, 1989).

$$\alpha = e \frac{r_1 r_2}{r_2^2 - r_1^2}, \quad (2.35)$$

where r_1 and r_2 are radii of inner and outer spheres, respectively.

If an EDC is measured on a metallic sample and a well defined Fermi edge is obtained at parameters (ν_F, V_{RF}, V_{PF}) , χ_s is given as

$$\chi_s = h\nu - eV_{RF} - \alpha V_{PF}. \quad (2.36)$$

Since α is obtained by the calibration with monochromatic electron beams using the relation

$$\alpha (eV_P - eV_{Po}) = \hat{\epsilon}'_k - \hat{\epsilon}'_{ko} \quad (2.37)$$

we have all measurable quantities on the right hand side of (2.36)

One important fact about the electrostatic energy analyzer is that the resolving power is independent of the kinetic energy. By the use of (2.35), it is easily shown that

$$\left| \frac{\hat{\epsilon}'_k}{\Delta\epsilon} \right| = \frac{R}{w} \quad (2.38)$$

where R is the diameter of the electron trajectory in the analyzer. R is given as

$$R = r_1 + r_2. \quad (2.39)$$

Thus we have

$$\frac{\hat{\epsilon}'_k}{\Delta\epsilon} = \beta \quad (2.40)$$

where β is a constant determined by the shape and the size of the energy analyzer. In many cases, β is fixed to a value around 100. Equation (2.40) indicates that $\Delta\epsilon$ is made small if we reduce $\hat{\epsilon}'_k$ by large retardation.

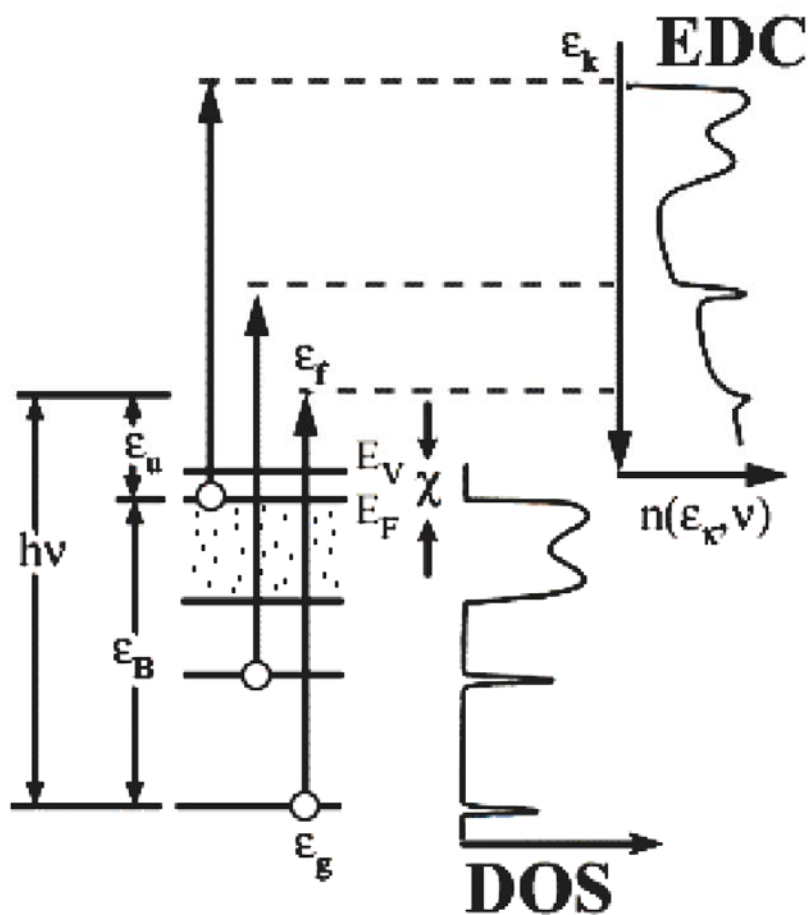


Fig. 2.16 Schematic illustration of photoelectron EDC, corresponding energy levels and the DOS curve. ϵ_f , ϵ_g , E_v , E_F are the energies for the final state, the initial state, vacuum level and Fermi level, respectively (Ishii, 1989).

2.3.5 Angle-Resolved Photoemission

As already pointed out, photoemission spectroscopy provides us with the energy-band dispersion curves, E - \mathbf{k} curves. This is achieved by the angle-resolved measurements. In Fig. 2.17, the concept of the measurements of angle-resolved photoemission is shown. A single crystal is used. For simplicity, we define the x , y and z direction as illustrated in the figure. The sample is rotatable around the x and z axes. The energy analyzer which accepts emitted electrons is also rotatable around the sample. Let θ and ϕ be the polar angle and the azimuthal angle of the direction of the emitted electrons. In the figure, the direction of the incidence of excitation light makes an angle, α , from the z axis. θ , ϕ , and α can be varied by rotating the sample and the energy analyzer. The angle-resolved photoemission spectroscopy is often abridging as ARPES.

The quantities we measure reflect the state of electrons in the solid. If we measure the kinetic energy of a photoelectron and its emission direction, we can assign the momentum it has in the vacuum. Let the momentum be \mathbf{p} . The problem is to obtain the photoelectron momentum inside the sample. From (2.33), we have

$$\varepsilon_u = \varepsilon_k - \chi. \quad (2.41)$$

Then the question is whether the electron is deflected when it passes through the surface. The practical assumption we may set up is that only the component of the momentum parallel, \mathbf{p}_{\parallel} to the surface is conserved:

$$\begin{aligned} \mathbf{p}_{\parallel} &= p \sin \theta \\ &= \hbar \mathbf{k}_{\parallel} \end{aligned} \quad (2.42)$$

Here θ is the angle of the emission direction as measured from the surface normal.

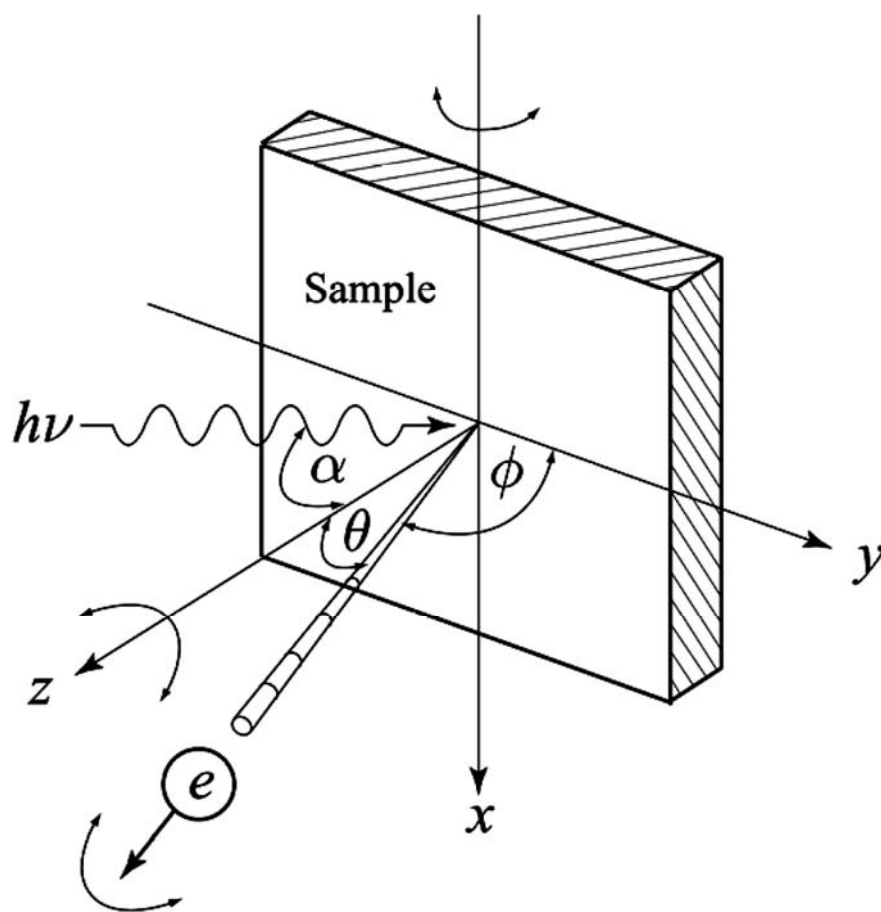


Fig. 2.17 Concept of angle-resolved photoemission. (Ishii, 1989)

Therefore, we obtain the parallel component of the electron wave vector as

$$\begin{aligned} k_{\parallel} &= \frac{1}{\hbar} \sqrt{2m\varepsilon_k} \sin \theta \\ &= 0.51(\text{\AA}^{-1}) \sqrt{\varepsilon_k (\text{eV})} \sin \theta \end{aligned} \quad (2.43)$$

$$\varepsilon_{v,\mathbf{k}} = \varepsilon_u + \chi - h\nu \quad (2.44)$$

We obtain relation

$$h\nu = \varepsilon_u + \varepsilon_B = \varepsilon_u - \varepsilon_g \quad (2.45)$$

If we use (2.45) for the energy band case and the momentum conservation, we have

$$\varepsilon_{c\mathbf{k}'} = \varepsilon_{v\mathbf{k}} + h\nu \quad (2.46)$$

$$\mathbf{k}' = \mathbf{k} + \mathbf{K}. \quad (2.47)$$

Here \mathbf{K} is a reciprocal lattice vector and \mathbf{k}' is the wave vector of the excited photoelectron. The electron wave vector is originally defined in the Brillouin zone, *i.e.*, the reciprocal lattice space. However, we obtain the wave vector in the coordinate in real space. In (2.42), we obtain \mathbf{k} with \mathbf{p} . This is correct, because the exponential factor $e^{i\mathbf{k}\mathbf{r}}$ in the Bloch function connect \mathbf{r} in the real space with \mathbf{k} in reciprocal space through the same coordinate system.

In a two dimensional crystal, electrons move in a two dimensional plane. In a case like this the component of the wave vector normal to this plane, k_{\perp} is not be a good quantum number describing the electronic state of the crystal and not important. Then, practically we have

$$\mathbf{k} = \mathbf{k}_{\parallel} \quad (2.48)$$

From (2.46), we have

$$\varepsilon_{v,\mathbf{k}} = \varepsilon_v(\mathbf{k}_{\parallel}) \quad (2.49)$$

If we measure k_{\parallel} from (2.42) and $\varepsilon_{v,\mathbf{k}}$ from EDC, we can plot (2.49). This gives us the

dispersion curve of the two dimensional energy-band. Thus, the method described above gives us the E- \mathbf{k} curve of the surface energy-band.

ARPES is quite useful for the two dimensional energy bands. On the other hand, the dispersion of the three dimensional band cannot be obtained without making further assumptions, since the component of \mathbf{k} normal to the crystal surface is not known from experimentally observed momentum, \mathbf{p} , of the photoelectron in the free space. A model that proved to work well empirically is to adopt the energy free electron approximation for the excited photoelectron. Then, the kinetic energy is given as

$$\varepsilon_u = \frac{(\hbar k)^2}{2m} - E_o, \quad (2.50)$$

where $-E_o$ is the potential energy of the interior of the crystal referenced to the Fermi level. If we rewrite (2.50) using the measurable energy, we have

$$\begin{aligned} \frac{(\hbar k)^2}{2m} &= \varepsilon_k - (E_o + \chi) \\ &= \varepsilon_u + V_o \end{aligned} \quad (2.51)$$

where V_o is the crystal potential referenced to the vacuum level. Fig. 2.18 schematically illustrates the dispersion of the energy band in the approximation described above. The band above the vacuum level is approximated by the nearly free electron band. If we find a photoelectron with a kinetic energy $p^2 / 2m$, this is equal to ε_k ; the electron is in the nearly free electron level given by (2.50) and (2.51). In this model, combining (2.43) and (2.51), we have

$$k_{\perp} = \frac{1}{\hbar} \sqrt{2m(\varepsilon_k \cos^2 \theta + V_o)} \quad (2.52)$$

$$= (0.51 \text{\AA}^{-1}) \sqrt{(\varepsilon_k \cos^2 \theta + V_o)(eV)} \quad (2.53)$$

Using (2.43), (2.44) and (2.53), we have k_{\parallel}, k_{\perp} , and $\varepsilon_{v,\mathbf{k}}$ expressed in terms of measurable quantities. Thus, if we fine V_o appropriately, we can depict the dispersion curve

$$\varepsilon_B = \varepsilon_v(\mathbf{k}) \quad (2.54)$$

In the energy band calculation, the dispersion relation is usually calculated along an axis with specific symmetry. It is rather complicated to select θ and $h\nu$ to obtain \mathbf{k} with specific symmetry. A few methods have been developed so far, but we do not discuss them any further here.

If synchrotron radiation is used as excitation light, the excitation energy is tunable and this is conveniently utilized to obtain the dispersion curve. In this method, only photoelectrons emitted normal to the crystal surface are collected. Then, $k_{\parallel} = 0$ and $\theta = 0$, and we have, from (2.52) and (2.53)

$$k_{\perp} = \frac{1}{\hbar} \sqrt{2m(\varepsilon_k + V_o)} \quad (2.55)$$

important symmetry axis of the crystal lies along the direction normal to the crystal surface, k_{\perp} give \mathbf{k} along this symmetry axis. If the energy of excitation light is changed, ε_k changes. Thus using (2.44), $\varepsilon_{v,\mathbf{k}}$ is obtained. On the other hand, \mathbf{k} is obtained from (2.55). Thus we obtain the dispersion relation given as (2.54).

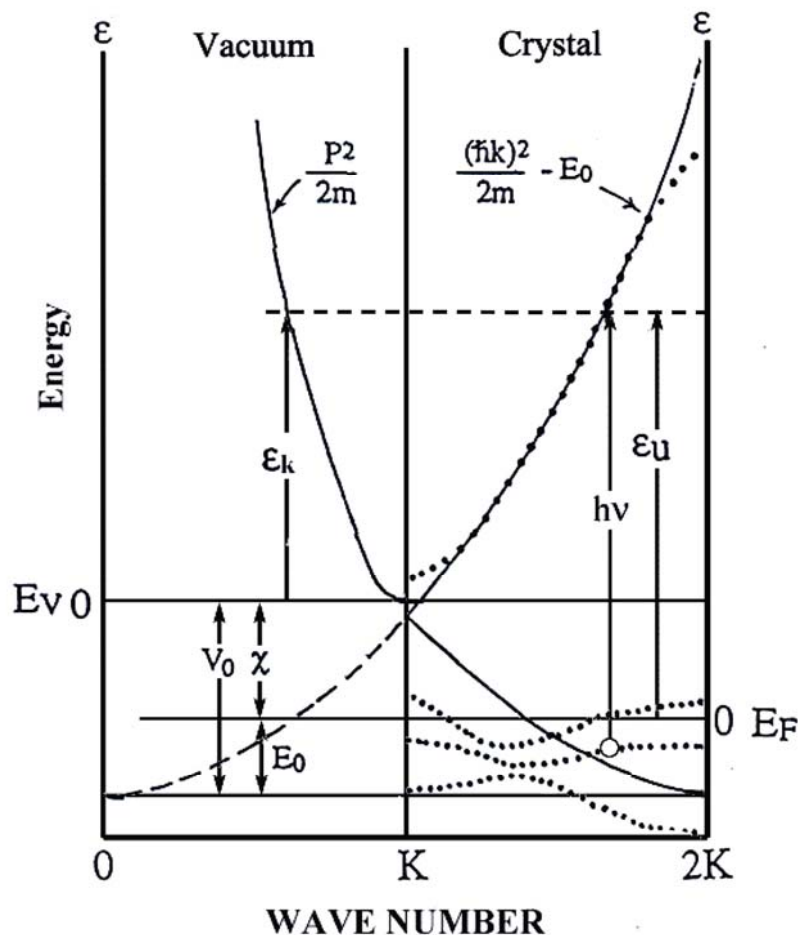


Fig. 2.18 Energy dispersion in the nearly free electron model for photoelectrons in ARPES. The right half represents the energy levels in a crystal. Curves illustrated by dots are energy-bands. Full lines are energy-band for the nearly free electron model. The left half represents the energy levels outside the crystal. K is reciprocal lattice vector. $h\nu$: Photon energy. χ : Work function. ε_u : Kinetic energy in the crystal. ε_k : Kinetic energy in a free space. E_F : The Fermi energy. E_v : Vacuum level (Ishii, 1989).

2.4 Methods of Calculation

The abundance of physical and chemical properties of surfaces finds its fundamental explanation in the arrangement of atoms, the distribution of the electrons and their response to external changes. Therefore, the understanding and quantitative prediction of the electronic structure takes a central and fundamental role in today's concept of surfaces. The quality and reliability of any electronic structure theory of surfaces depend on the ability to describe the many-body interactions accurately enough to allow quantitative predictions of physical properties. On the other hand, the theory has to allow practical calculations at a reasonable computational effort on systems which are large enough so that realistic surface models can be studied.

Since the formation of quantum mechanics in the 1920's, the two major theoretical and computational approaches have appeared namely Hartree-Fock theory and density functional theory. A third approach, quantum Monte Carlo, is promising but, has remained limited to rather small systems. Because of its applicability to a wide range of systems including metallic, semiconducting, and insulating materials and its good balance between accuracy and computational efficiency, density functional theory has become the dominant approach for electronic structure calculation of surfaces. Therefore, this section focuses on density functional methods and their applications to surface problems.

Electrons and nuclei composing a solid material are a strongly interacting many body quantum mechanical-system. It can be described by the Schrödinger equation which even for small systems is impossible to solve analytically. Therefore methods have to be applied that approximate the particular problem and solve the Schrödinger equation computationally. The program performing all the calculations in

the thesis work is a tool where these ideas are implemented. It is called VASP (Vienna Ab-initio Simulation Package) which has been developed mainly by Kresse and Furthmüller (1996). It is a complex package for performing ab-initio quantum-mechanical molecular dynamics (MD) simulations using pseudopotentials or the projector-augmented-wave (PAW) method and a plane wave basis set. This topic will provide an introduction in some of the basic ideas and concepts implemented in this program.

2.4.1 Density Functional Theory

2.4.1.1 The Hohenberg-Kohn Theorem

A great simplification of the electronic ground state energy can be made by the theorem of Hohenberg and Kohn (1964) are based on density functional theory (DFT) and the local density approximation (LDA). This theorem may be summarized as follows:

1. The total energy of a system such as a bulk solid or a surface depends only on the electron density of its *ground state*. In other words, one can express the total energy of an atomic system as a functional of its electron density

$$E = E[\rho(\mathbf{r})]. \quad (2.56)$$

2. There exists a variational principle for the above energy density functional $E[\rho(\mathbf{r})]$. Namely, if $\rho(\mathbf{r}')$ is not the ground state density of the above system, then $E[\rho(\mathbf{r}')] > E[\rho(\mathbf{r})]$.

Therefore one has to solve the variation problem

$$\delta \left\{ E[\rho] - \mu \left[\int \rho(\mathbf{r}) d\mathbf{r} - N \right] \right\} = 0 \quad (2.57)$$

where μ is the Lagrange parameter associated with the limitation of the density to yield the correct total number of electrons N . The quantity μ is actually the chemical potential. Consequently, the main problem is to find a suitable expression for the energy functional $E[\rho(\mathbf{r})]$.

2.4.1.2 The Single-Particle Formalism of Kohn and Sham

To gain a compact form of the energy functional, Kohn and Sham (1965) described the particle density ρ as a sum over the probabilities of single-particle states. With this concept it was possible to derive an eigenvalue equation for these states. We have introduced single-particle wave functions $\psi_i(\mathbf{r})$ which generate the electron density

$$\rho = \sum_i |\phi_i\rangle\langle\phi_i| \quad (2.58)$$

and energy functional can be expressed as:

$$E[\rho] = Tr \left[\left(T + V_{ion} + \frac{1}{2} V_H \right) \rho \right] + E_{xc}[\rho], \quad (2.59)$$

where T is the operator of the kinetic energy, V_{ion} is the ionic potential, V_H is the Hartree potential and E_{xc} is the exchange-correlation energy, which describes all many-particles effects that are not included in the Hartree term. The abbreviation Tr denotes the trace of a matrix.

Substituting for ρ in (2.59) from (2.58) yields

$$Tr[T\rho] = Tr \left[\sum_i -\frac{\hbar^2}{2m} \Delta |\phi_i\rangle\langle\phi_i| \right] = \sum_i \langle\phi_i| -\frac{\hbar^2}{2m} \Delta |\phi_i\rangle \quad (2.60)$$

$$Tr[V_{ion}\rho] = \int \langle\mathbf{r}| V_{ion} \rho |\mathbf{r}\rangle d\mathbf{r} = \int V_{ion}(\mathbf{r}) \rho(\mathbf{r}) d\mathbf{r} \quad (2.61)$$

$$\text{Tr}\left[\frac{1}{2}V_H\rho\right] = \frac{1}{2}\int\langle\mathbf{r}|V_H\rho|\mathbf{r}\rangle d\mathbf{r} = \frac{e^2}{2}\iint\frac{\rho(\mathbf{r})\rho(\mathbf{r}')}{|\mathbf{r}-\mathbf{r}'|}d\mathbf{r}d\mathbf{r}' \quad (2.62)$$

The crucial point is to find exact expression for E_{xc} which turns out to be not possible yet. Therefore approximations have to be done.

2.4.1.3 The Kohn-Sham Equations

If the energy functional (2.59) is minimized considering the norm of the single particle states and the corresponding Lagrange multipliers ϵ_i ,

$$L[\epsilon_i, \phi_i] = E[\rho] - \epsilon_i(\langle\phi_i|\phi_i\rangle - 1) \quad (2.63)$$

and using relations

$$\frac{\delta}{\delta\langle\phi_i|} = |\phi_i\rangle, \quad \frac{\text{Tr}\left[\frac{1}{2}V_H\rho\right]}{\delta\rho} = V_H, \quad \frac{\delta E_{xc}[\rho]}{\delta\rho} = V_{xc} \quad (2.64)$$

where V_{xc} is the exchange correlation potential, the single-particle Kohn-Sham equations can be derived.

$$\frac{\delta L}{\delta\langle\phi_i|} = (T + V_{ion} + V_H + V_{xc} - \epsilon_i)|\phi_i\rangle = (H - \epsilon_i)|\phi_i\rangle = 0 \quad (2.65)$$

These are of Schrödinger-like equations for the single particle wavefunctions $|\phi_i\rangle$.

As it is outlined in the section about the electronic ground state, these equations have to be solved self-consistently.

2.4.1.4 The Local-Density Approximation

As consequence of the Kohn-Sham theorem, the exchange-correlation energy depends on the electron density. As a simple good approximation one can assume that the exchange-correlation energy depends on the local electron density around each volume element $d\mathbf{r}$. This is called the local density approximation (LDA)

Therefore it can be expressed as

$$E_{xc}[\rho] = \int \rho(\mathbf{r}) \epsilon_{xc}[\rho(\mathbf{r})] d\mathbf{r}, \quad (2.66)$$

where $\epsilon_{xc}[\rho(\mathbf{r})]$ is the exchange-correlation energy per particle in the free and uniformly distributed electron gas with the density $\rho(\mathbf{r})$. The exchange-correlation potential is then given by

$$v_{xc}[\rho(\mathbf{r})] = \frac{\delta E_{xc}}{\delta \rho(\mathbf{r})} = \epsilon_{xc}(\rho) + \rho(\mathbf{r}) \frac{\partial \epsilon_{xc}(\rho)}{\partial \rho}. \quad (2.67)$$

In the Hartree-Fock approximation where the many-particle wavefunction is described as a Slater-determinant of single-particle orbital the exchange energy can be written exactly as

$$\epsilon_x[\rho(\mathbf{r})] = -\frac{3}{4} \left(\frac{3}{\pi} \right)^{\frac{1}{3}} \rho(\mathbf{r}) \quad (2.68)$$

The correlation energy is defined as the difference between the exact many-particle energy and the Hartree-Fock results. It is not possible to give an exact analytic result, but it is feasible to get numerical expressions which can easily be parameterized. The Random Phase Approximation (RPA), which is based on many-particle methods, is such a tool that can give an analytic expression for the correlation energy. Currently the most accurate values of the correlation energy are derived from quantum-Monte Carlo simulations for the homogeneous electron gas.

This condition is reasonably well obeyed in the conduction band of the nearly free electron metals, e.g. Na and K. However if there are strong density gradients, due to directional chemical bindings for example, much greater care is necessary using equations (2.66) and (2.68) as a starting approximation. There is another source of inaccuracy in local density calculations, namely if the cancellation of self-interaction contribution in both electrostatic and the exchange-correlation terms is incomplete.

The LDA, which used in almost all the calculations of this thesis work, provides important improvement as far as the surface structure is concerned.

2.4.1.5 Generalized Gradient Approximation

The condition of having a slowly varying particle density is generally not valid in solid state matter. Nevertheless, LDA gives, even in systems with inhomogeneous charge density, surprisingly accurate results although the value of the total energy is almost always overestimated. Therefore many so-called inhomogeneity corrections have been proposed. For densities that vary over space, Hohenberg, Kohn and Sham suggested a gradient expansion of the exchange-correlation functional:

$$E_{xc} = \int \epsilon_{xc} [\rho(\mathbf{r})] d\mathbf{r} + \int \epsilon_{xc} [\rho(\mathbf{r})] |\nabla\rho(\mathbf{r})| d\mathbf{r} \quad (2.69)$$

It can immediately be seen, that without the second term in (2.69) it would be just the local density approximation. The second-order gradient-expansion approximation (GEA) provides no systematic improvement, because it violates important sum rules that are not treated here in detail. Thus, it is unphysical and yields results worse than the LDA.

This problem was solved by the generalized gradient approximation (GGA) proposed by Perdew and Wang (1986) where the exchange functional is expressed as

$$E_{xc}^{GGA}[\rho(\mathbf{r})] = A_x \int d^3r \rho(\mathbf{r})^{4/3} F^{GGA}(s) \quad (2.70)$$

where

$$F^{GGA}(s) = -\frac{(3\pi^2)^{1/3}}{12\pi A_x} \int_0^{z_c} dz z \frac{1}{4\pi} \int d\mathbf{R} y \Theta(y). \quad (2.71)$$

s is defined as $s = \frac{\nabla\rho}{2k_F\rho}$ and k_F is the local Fermi-wavevector $k_F = (3\pi^2\rho)^{1/3}$. The

parameter $z_c = 2k_F R_c$ is determined by the condition

$$\frac{-1}{12\pi} \int_0^{z_c} dz z^2 \frac{1}{4\pi} \int d\mathbf{R} y \Theta(y) = -1, \quad (2.72)$$

and the angular integration

$$\frac{1}{4\pi} \int d\mathbf{R} y \Theta(y) = \frac{1}{2} \int_{-1}^1 d\mu (A\mu^2 + B\mu + C) \times \Theta(A\mu^2 + B\mu + C) \quad (2.73)$$

is performed analytically, and then the z integrations are performed numerically.

2.4.1.6 Electronic Ground State

Several methods within the DFT exist to find the ground-state wavefunction of the electron in the Kohn-Sham equations. The most common method uses a trial input charge density ρ^0 . This charge density is used to set up the Kohn-Sham Hamiltonian. With the solutions, the Kohn-Sham wavefunctions, new charge densities are calculated. If these are the correct ones for the system, then they are the same as the input charge densities, which will not be the case after the first run. So what is done is to mix the out coming charge density with the initial one to get a new input charge density. Then with this new charge density the Kohn-Sham equations are set up and solved again, and the whole process is repeated until a self consistent solution is found.

To find a solution for the Kohn-Sham equation in every self-consistency step the lowest eigenvalue of the Hamiltonian matrix has to be calculated. Many different methods exist for this task:

Direct Diagonalization

For small systems, the resulting eigenvalue equations can be solved efficiently using standard eigenvalue solver. Most such programs rely on the Householder algorithm and the computational time necessary to do the transformation is proportional to N^3 , where N is the total amount of particles treated in the simulation. For large systems with $N_{\text{dim}} > 5000$, standard eigenvalue solvers are usually not applicable, since the computer time becomes tremendous.

Steepest Decent Scheme

This is a very simple method for the determination of a minimum of a function. After a starting point has been chosen one repeats the search of the minimum along the local gradient of the function till a minimum has been found.

Conjugate Gradient (CG) Optimization

It is also possible to optimize the expectation value of the Hamiltonian using a successive number of conjugate gradient steps. The first step is equal to the steepest decent step. In the following step the preconditioned gradient is conjugated to the previous search section.

Residual Minimization Scheme

The disadvantage of the CG-method is that the search vector has to be orthonormalized to the current set of wavefunctions for all lower-lying eigenstates. However, instead of minimizing the expectation value $\langle \mathbf{R} | = (H - E_{app}) | \phi_{app} \rangle$ it is also possible to minimize the norm of the residual vector, without the orthonormalization of the residual vector.

2.4.2 Pseudopotentials and The Projector-Augmented-Wave Method

2.4.2.1 Plane Waves

Plane waves have the advantage of forming a complete set of basis vectors. For a periodic crystal the completeness relation reads

$$\sum_{\mathbf{G}} |\mathbf{k} + \mathbf{G}\rangle \langle \mathbf{k} + \mathbf{G}| = 1 \quad (2.74)$$

where the \mathbf{G} are the reciprocal lattice vectors of the crystal structure. Therefore it is possible to describe the Bloch wavefunction of an electron in a crystal structure in every k -point as a sum of plane waves:

$$|\phi_{n\mathbf{k}}\rangle = \sum_{\mathbf{G}} C_{\mathbf{G}n\mathbf{k}} |\mathbf{k} + \mathbf{G}\rangle \quad (2.75)$$

For that reason plane waves are used as a basis set for the representation of the electronic states in a solid. However, in practice a convergence of a plane-wave expansion of the valence orbital is found to be very slow. The reason is that according to the Pauli principle, the wavefunction of the valence electrons have to be orthogonal to the orbital of the core-electrons with lower energy.

2.4.2.2 The Concept of Pseudopotentials

Experience has shown that the tightly bound electrons nearby the ionic core practically have no contribution to the chemical bonding between the atoms. For this task only the loosely bound valence electrons in the outer region of the atoms play a major role.

Based on that knowledge it is possible to split the electron-ion potential in a solid, molecule or atom into two separate regions. This big simplification is the foundation of the concept of pseudopotentials:

1. The first part is the *core-region* where the electrons are in the direct vicinity of the core. It is defined by the cut-off radius R_c . The tightly bound core-electrons are confined to this region and are almost not influenced by the neighboring atoms. The wavefunctions of the valence electrons oscillate in this region and the potential seen by the electrons is strongly attractive.

2. The second part is the *interstitial* region, which is the rest of the solid. Here are the valence electrons, responsible for the inter-atomic binding. The potential in this region varies very slowly and the wavefunctions of the valence electrons also vary smoothly.

The pseudopotential concept consists in eliminating the nodal structure of the valence electrons and in replacing the strong electron-ion potential responsible for binding them by a weak pseudopotential. This can be achieved, at least in principle, by projecting the Schrödinger-equation onto the sub-space of Hilbert-space orthogonal to the core-orbital. Alternatively one can start by reconstructing nodeless pseudo-valence orbital matching the exact valence wavefunction at the surface of the cut-off sphere with a continuous logarithmic derivative, which is defined as:

$$X_l(r, E) = \frac{1}{\phi_l(r, E)} \frac{d\phi_l(r, E)}{dr} = \frac{d}{dr} \ln \phi_l(r, E), \quad (2.76)$$

with the angular-momentum quantum-number l , the energy E and the radial distance r . The pseudo wavefunction $\phi_l^{PS}(r)$ are constructed in such a way that they agree with the all-electron wavefunctions $\phi_l^{AE}(r)$ outside a cut-off radius R_c and that the logarithmic derivatives agree at this distance like it is shown in Fig. 2.19:

$$X_l^{AE}(R_c, \epsilon_l) = \frac{1}{\phi_l^{AE}(R_c, \epsilon_l)} \frac{d\phi_l^{AE}(r, \epsilon_l)}{dr} \Big|_{r=R_c} \quad (2.77)$$

$$= \frac{1}{\phi_l^{PS}(R_c, \epsilon_l)} \frac{d\phi_l^{PS}(r, \epsilon_l)}{dr} \Big|_{r=R_c} = X_l^{PS}(R_c, \epsilon_l) \quad (2.78)$$

where ϵ_l is energy state determined by l .

The pseudopotential is then constructed by inverting the Schrödinger-equation. Since the logarithmic derivatives of the exact and pseudo-orbital agree, the scattering properties of the pseudo- and all-electron potentials are identical for $r > R_{\text{cut}}$.

To reduce the computational effort, the states of all electrons of a specific reference atom are calculated once and the influence of the core and the core-electrons to the valence electrons is summarized in a constant core potential that will not change in future applications. If this atom is then used in a different chemical environment, only the changes concerning the valence electrons are calculated.

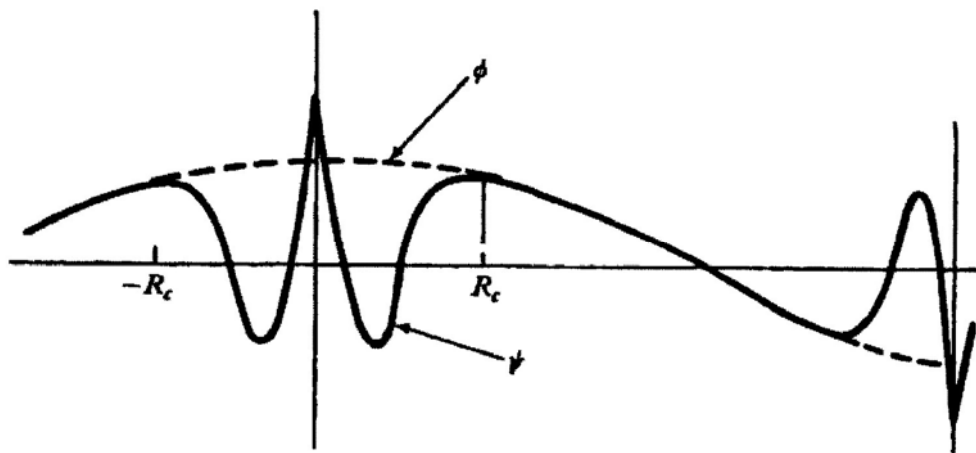


Fig. 2.19 Real wave-function ψ and pseudo-wave function ϕ of an electron in a solid.

R_c is the radius of the ion core.

2.4.2.3 Norm-Conserving Pseudopotentials

The task is to substitute the all-electron potential by a pseudopotential that has not such strong oscillations in the core region like the original potential but describes the energy eigenvalues and the potential of the solid very accurately in the interatomic region. The difficult point is that the pseudopotential must match the scattering properties of the all-electron potential not only at the energies corresponding to the bound eigenstates of the free atom, but also at all energies corresponding to the valence band in the crystal. Obviously, transferability will be improved if not only the logarithmic derivatives but also their derivatives with respect to energy are matched:

$$X'(R_c, \epsilon) = \left. \frac{d}{d\epsilon} X_l^{AE}(R_c, \epsilon_l) \right|_{\epsilon=\epsilon_l} = \left. \frac{d}{d\epsilon} X_l^{PS}(R_c, \epsilon_l) \right|_{\epsilon=\epsilon_l} \quad (2.79)$$

A theorem due to Topp and Hopfield (1973) relates $X'(R_c, \epsilon)$ to the norm of the wavefunction within a sphere with radius R_c . Hamann, Schlüter, and Chiang (1979) which was developed the concept of norm conserving pseudopotentials.

Constructing a pseudopotential $\tilde{V}(r)$, one has to consider that it should be exactly equivalent to the real potential $V(r)$ outside a certain core radius R_c . Inside this radius the pseudopotential will reproduce the scattering properties and the energy of bound valence states of the atom exactly.

2.4.2.4 Ultrasoft Pseudopotentials and The Projector Augmented-Wave

Method

In computational material science pseudopotentials with plane wave basis sets are currently among the most successful techniques. They are formal quite simple and therefore relatively easy to implement in codes based on density functional methods. Their disadvantage is that first-row elements, transition metals and rare-earth elements are computationally demanding to treat with standard norm-conserving pseudopotentials.

The “ultrasoft pseudopotential” first proposed by Vanderbilt (1990) offers a possibility to resolve the problem of plane-wave convergence even for transition metals. Vanderbilt innovations consist of two fundamental steps: (a) the norm-conservation constraint is relaxed and the differences in the charge densities calculated from the all-electron and pseudo-orbital is described in terms of a small number of localized augmentation functions. This makes it possible to construct extremely soft pseudo wavefunctions requiring only a very low cutoff energy. (b) The freedom gained by relaxing the norm-conservation constraint is used to fit the scattering properties of the all-electron functions not only at one, but at two or more reference energies spanning the entire width of the valence band. This allows perfect control of the accuracy and transferability of the ultrasoft pseudopotentials.

A different way of dealing with the pseudization problem was discovered by Blöchl (1994). He developed quite recently a concept called the projector augmented wave method (PAW), which combines ideas from the ultrasoft pseudopotential and from linearized augmented plane-waves (LAPW). The important point is that the all

electron wavefunction $|\psi_n^{AE}\rangle$ are related to the pseudo-wavefunctions $|\psi_n^{PS}\rangle$ through a linear transformation

$$|\psi_n^{AE}\rangle = |\psi_n^{PS}\rangle + \sum_i \left(|\phi_i^{AE} - \phi_i^{PS}\rangle \right) \langle \beta_i | \psi_n^{PS} \rangle. \quad (2.80)$$

Here the index i represents a short-hand notation combining the atomic site \mathbf{R}_n , the angular momentum quantum numbers $L = l, m$ and the index k referring to the reference energy ϵ_{kl} . The all-electron partial waves $|\phi_i^{AE}\rangle$ are obtained for a reference atom and the pseudopotential partial waves $|\phi_i^{PS}\rangle$ are equivalent to the all-electron partial waves outside a core radius R_c^l and match continuously onto $|\phi_i^{PS}\rangle$ inside the core radius. Through the all-electron partial waves it is ensured that the nodal structure of the wavefunction is physically correct near the nucleus, which is of great importance for simulations of first row and transition elements. The core radius R_c^l is usually chosen approximately around half the nearest neighbor distance. The projector functions $\langle \beta_i |$ are dual to the pseudo-partial waves and may be chosen as in the Ultrasoft-pseudopotential method:

$$\langle \beta_i | \phi_j^{PS} \rangle = \delta_{ij}. \quad (2.81)$$

Therefore Blöchl introduces a linear transformation from the pseudopotential to the all-electron wavefunction. As a next step the PAW total energy functional is derived in a consistent manner applying this transformation to the Kohn-Sham functional. The construction of PAW datasets is easier than the one of ultrasoft pseudopotentials because the pseudization of the augmentation charges is avoided. The PAW method works directly with the full all-electron wavefunctions and potentials.

CHAPTER III

EXPERIMENTAL

This chapter describes the experimental instruments and procedures used in this thesis work. First, the experimental instruments are described. Explanations are made on the element located along the beamline. Then, the preparation of the sample and practical experimental procedure are mentioned. Finally, the detail of surface calculation is explained.

3.1 Experimental Instruments

The experimental station of the BL4 is a photoemission system shown in Fig. 3.1. Both angle-resolved and angle-integral photoemission experiments can be performed. The photoemission consists of two main ultra-high vacuum (UHV) chambers, *i.e.*, a preparation and analysis chambers.

3.1.1 Vacuum Chamber

Photoemission measurements have to be performed in a UHV environment. With modern vacuum technology, a proper-designed vacuum system can reach vacuum pressure in a range of 10^{-10} mbar or better. Only such a low pressure will convince that a surface stays clean for a time long enough to do some experiments. The UHV system used in the experiments was equipped with a turbomolecular pump backed by rotary pump, and sputter ion pump combined titanium sublimation.

Baking of photoemission systems is essential to remove desorbed gas molecules on the interior surface vacuum chamber and the surface of tools in the vacuum system. The baking is normally done at 150 °C for at least one day. In the present experiments, whole vacuum chambers were contained in a box, the walls of which are made of thermal insulators and heating elements were contained in this oven-like shroud.

Following baking, degassing of the sample and filament parts is needed. The heating of the sample is made by electron bombardment of the sample holder for a short time. This procedure is often referred to a flash baking. Degassing of filaments is performed just by flowing current on filaments.

After UHV is achieved, the analysis of residual gases shows that they consist of gases that are not main atmospheric constituents. The dominant residuals are usually H₂, H₂O, CO and CO₂.

The two chambers are vacuum-isolated by a gate valve as illustrated in Fig. 3.2. The availability of the preparation system allows *in situ* analysis of samples treated in the preparation system. UHV environment is essential as photoemission is a surface sensitive technique. Two ion pumps and two titanium sublimation pumps are used to obtain UHV in the preparation and analysis chambers with typical based vacuum pressure of $\sim 2 \times 10^{-10}$ mbar. A turbo-molecular pump is used for extra pumping during cleaning surface of samples and for loading samples into the analysis chamber. The analysis chamber is connected to the end of the BL4 via a line-of-sight valve. This provides possibility to disconnect the experimental station from the beamline without breaking the UHV condition.



Fig. 3.1 Photoemission system shown above is an experimental station of the BL4 beamline.

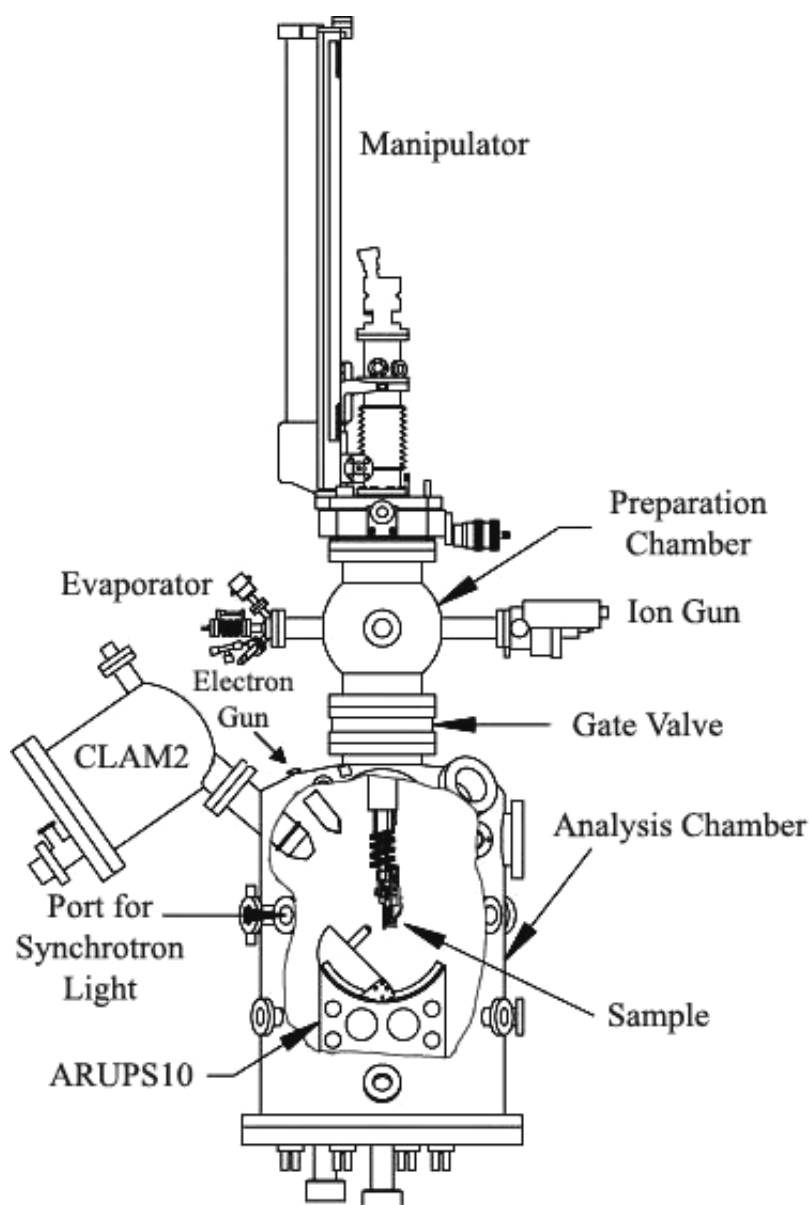


Fig. 3.2 Schematic diagram of the photoemission system. CLAM2 and ARUPS10 energy analyzers are the main instruments.

3.1.2 Sample Holder

The sample holder system was attached to the bottom of manipulator arm. In addition, the sample holder has to be designed as compact as possible to allow the sample to be positioned come to the light beam. The manipulator consist of a three-axis positioning for XYZ translation, the polar rotation (θ) of the sample, and a sample stage capable of azimuthal rotation (ϕ) of the sample. The manipulator is also equipped with heating and cooling facilities to control the temperature of the sample. A sample is heated by electron bombardment. Electrons from the filament impinge the sample and activate the impurity removing from the surface of the sample. The sample temperature was measure by thermocouple and a pyrometer. The sample holder is shown in Fig. 3.3.

3.1.3 Low Energy Electron Diffraction (LEED)

LEED is the oldest surface science technique and is used to study the structure of crystalline surfaces. Low-energy electrons, with incident energy from 30-300 eV, they have a wavelength given by the de Broglie relation which varies from 2.7 Å to 0.5 Å in this case. This fits nicely into the range of distances between atoms in solids and can therefore strongly diffract from them. The recording and analysis of the diffraction pattern can tell us the arrangement of the atoms on the surface. The sharpness of the pattern is related to the extent of order of the atoms on the surface.

Fig. 3.4 shows a schematic diagram of the experimental setup for LEED measurements. The instrument is a Thermo VG Scientific RVL-900 rear view LEED incorporating the LEG24 high current miniature electron gun. The electron gun can be operated over the energy range from 5 to 100 V for LEED measurements.

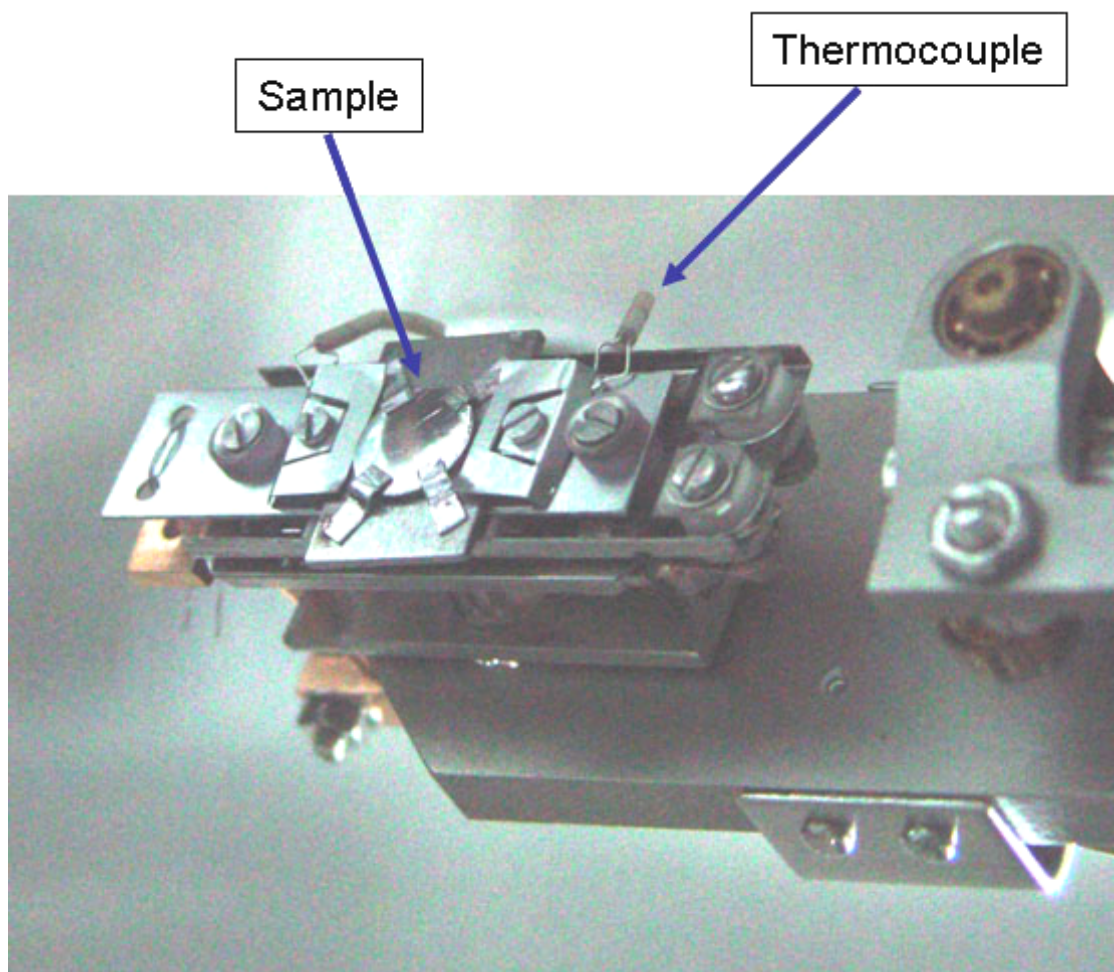


Fig. 3.3 The sample holder with thermocouple lines.

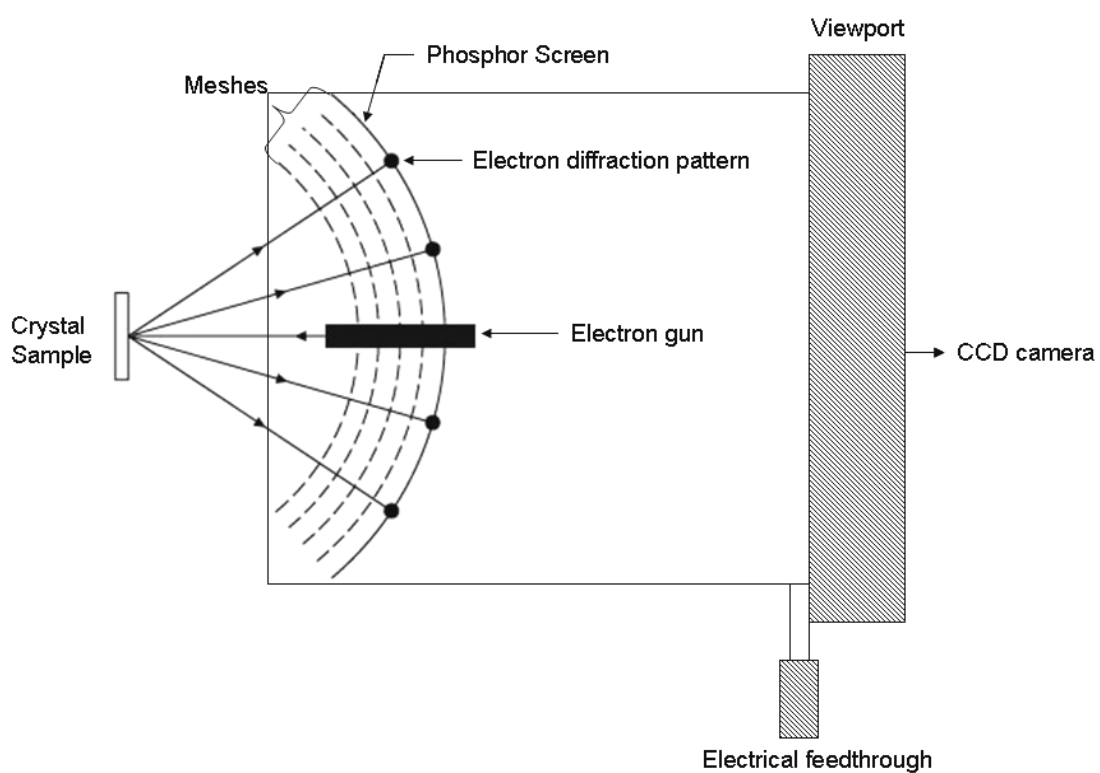


Fig. 3.4 Schematic diagram of rear view LEED setup.

The measurements are normally carried out in an UHV environment to achieve well-defined surface condition. From the LEED pattern, we can obtain information on the symmetry, surface unit-cell dimensions, and quality of the surface layers. To observe LEED pattern, a crystal with clean and well-defined surface is placed normal to the LEED screen, which is a fluorescent screen prevent electrons that are inelastically backscattered from the crystal to reach the screen. The voltage difference between the screen and the grid located just in front of the screen accelerates the elastically backscattered electrons to hit the screen.

3.1.4 Auger Electron Spectroscopy (AES)

Auger spectroscopy is a powerful analytical technique to check the cleanness of the freshly prepared sample surface and the concentration of elements at the surface in UHV system. AES characterizes the top 10-50 Å of the material with detection limits of ~0.25 atomic percent.

The Auger effect was discovered by Pierre Auger in 1923 as shown in Fig. 3.5. The process starts form an atom with a core hole in the level A. This core hole is filled by an electron from the level B. The remaining energy is used to kick out an electron from the level C. The kinetic energy of an Auger electron is then

$$E_{kin} = E_A - E_B - E_C - \Phi \quad (3.1)$$

This formula is not a very good one because it is only based on the atomic levels. Actually we are concerned with a transition from an atom with one core hole to an atom with two core holes. One often takes this into account by inserting the average between the Z and $Z+1$ energy levels for E_B and E_C into (3.1).

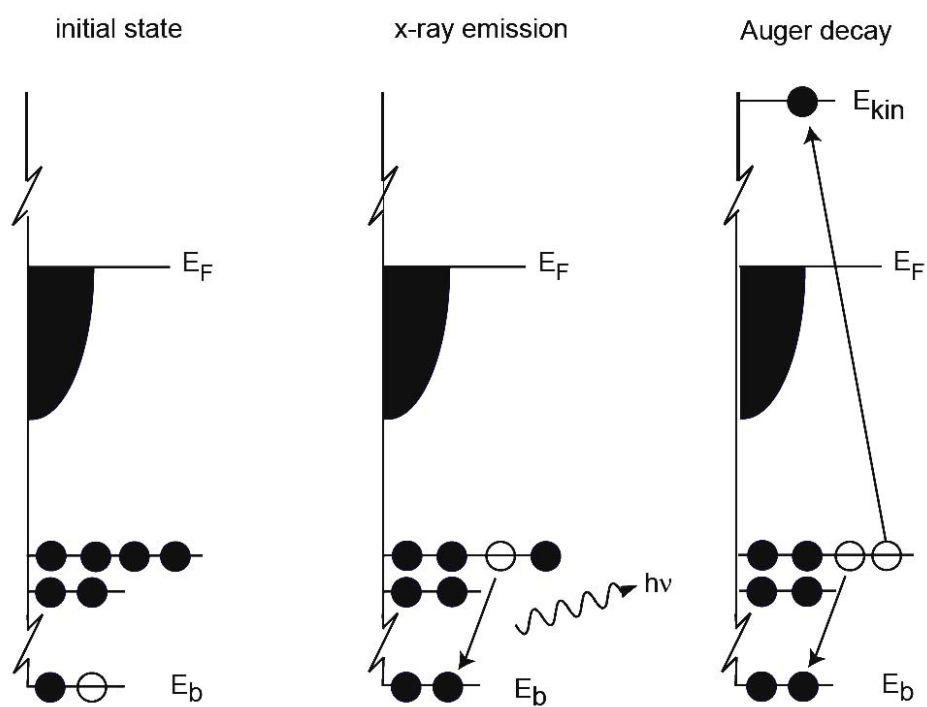


Fig. 3.5 Decay of a core-hole by x-ray emission or the Auger process.

The nomenclature used to describe an Auger transition is derived from X-ray terms. The inner electron shell being the K , and higher shells being L, M, N, O and V are used to denote valence states. For example the strong KLL Auger is formed by an initial hole produced in K -shell. Followed by an electron from outer L -shell (L_1 in this case) falls into this hole. This electron transfer it is transition energy to another electron in L -shell (L_3 in this case), which leaves the system with well-defined kinetic energy used to identify this atom as (Auger electron) as shown in Fig. 3.6. The Auger transition nomenclature can be made more rigorous by including with the X-ray terms, the partial terms for the angular momentum. For s, p and d terms 1, 2, 3, 4 and 5 are used, e.g. KL_1L_2 .

The AES system consists of an UHV system, an electron gun to bombard the sample surface and an electron energy analyzer to collect and analyze the secondary electron distribution. Auger spectra are normally displayed in one of two ways. The direct spectrum is the relation of E versus $N(E)$ where E is the Auger electron energy. However, the derivative spectra, $d[N(E)]/dE$, as shown in Fig. 3.7. The direct Auger spectrum consists of weak emission band that overlaps a huge broad background band. Thus, the real emission band cannot be easily resolved. If the derivative curve is plotted, the broad background bands that indistinct the Auger emission band. Thus, the real emission band cannot be easily resolved.

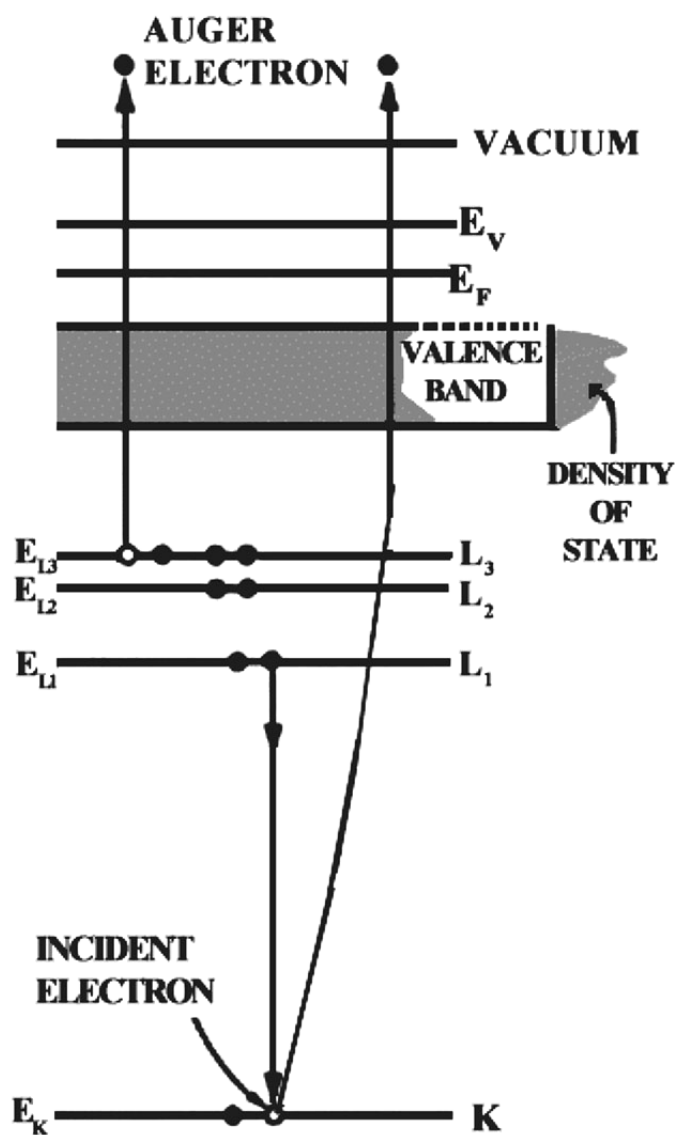


Fig. 3.6 Schematic energy level diagram illustrating the origin of the Auger effect.

The Auger process in this figure is the KL_1L_3 process.

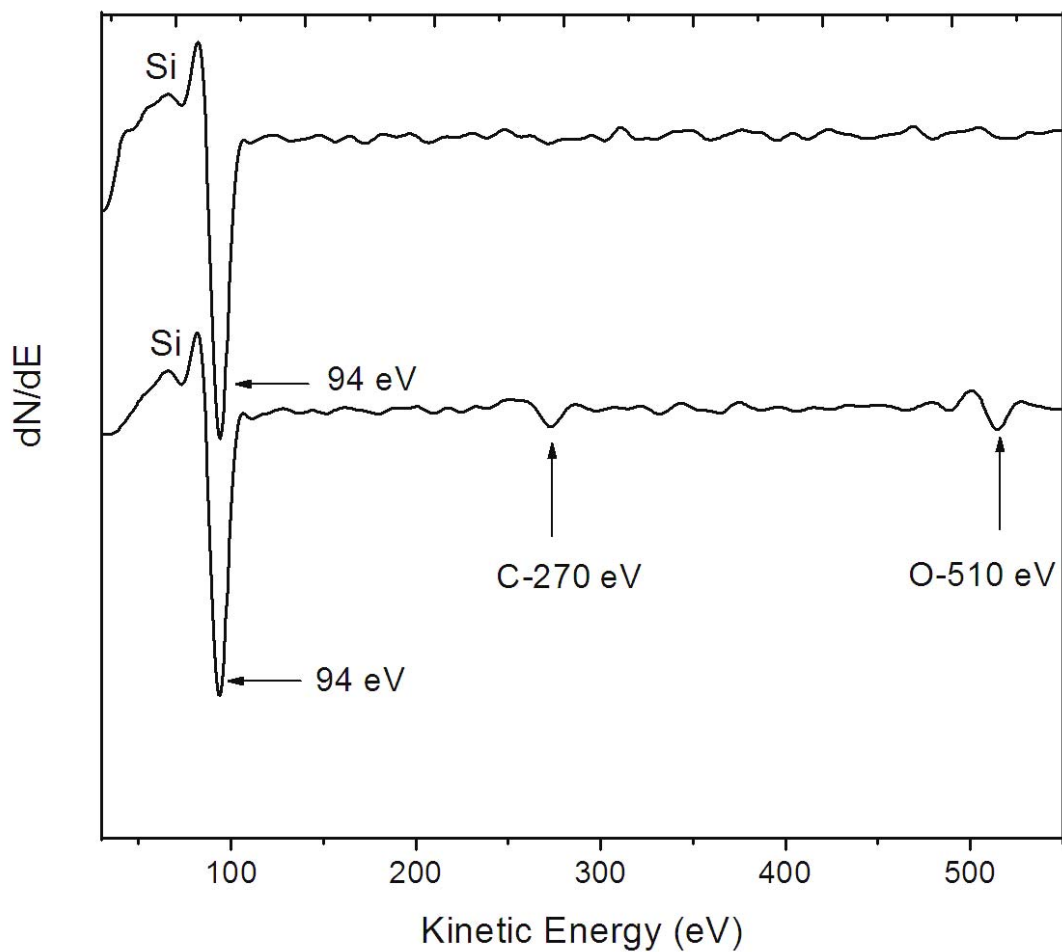


Fig. 3.7 Auger spectrum from LVV Si in differential spectrum. The upper graph is the graph from the clean Si(001)-(2 \times 1) structure. The lower graph represents the graph with contamination.

3.1.5 Energy Analyzer

Different types of energy analyzer have been developed in the past. It is agreed among scientists in the field of electron spectroscopy that a concentric hemispherical analyzer (CHA) is the most suitable type for photoemission studies. This type of analyzer provides important features such as high-energy resolution, high transmission and compatibility to UHV. In addition, an electron static lens can be integrated into the analyzer allowing longer working distances and controllable size of the analyzed area.

The analysis chamber is provided with two CHA electron energy analyzers manufactured by Thermo VG Scientific (U.K.). The two analyzers are an ARUPS10 analyzer and a CLAM2 analyzer.

3.1.5.1 ARPES Analyzer

ARUPS10 is a hemispherical analyzer with a mean radius of 75 mm. The analyzer is installed on a goniometer allowing the rotation of the analyzer around the sample position. Thus, the ARUPS10 analyzer is used for angle-resolved photoemission measurements. The specifications of the ARUPS10 analyzer are summarized in Table 3.1.

3.1.5.2 CLAM

CLAM2 analyzer is a concentric hemispherical energy analyzer with a mean radius of 100 mm. It is used for angle-integral photoemission measurements. The controller of the analyzer provides different mode of measurements. Thus, the CLAM2 analyzer is not only used for photoemission measurement but also AES measurements. The specifications of the CLAM2 analyzer are summarized in Table 3.2.

Table 3.1 Specifications of the ARUPS10 analyzer.

Analyzer	75 mm mean radius, hemispherical 180° with 30 mm hemisphere gap
Lens	Multi-element transfer lens, electrically switchable acceptance angle from $\pm 0.4^\circ$ to $\pm 2.0^\circ$
Detector	Multi-channel Detector
Energy Resolution	Variable from <10 meV to >2 eV
Goniometer	2-axis: 360° polar rotation, 100° azimuthal rotation, 0.1° precision angle readouts

Table 3.2 Specifications of the CLAM2 analyzer.

Analyzer	hemispherical 150° with 100 mm mean radius
Lens	2 element transfer lens can be used in two distinct modes
Detector	Single channel electron multiplier
Slit size	1/1 or 1/3 CRR values: 1, 2, 4, 10, 40, and 100
Energy Resolution	CAE values: continuous 0-400 eV (manual) or 2, 5, 10, 20, 50, 100, and 200 eV (computer controlled)
Working distant	Flange to sample distance, 240 mm

Fig. 3.8 shows a schematic of CLAM2. An electrostatic lens, which consist with two elements, is used to define the optics of electron emitted from the sample and be transported to the entrance slit of the analyzer. Before electrons entering the entrance slit, they experience a retarding or accelerating voltage to allow electrons with desired kinetic energy to pass through the analyzer and detected by the detector, which is located behind the exit slit. The resolution is defined by the pass energy. The electron-energy distributions are obtained by measuring the electron detected by the detector as a function of the retarding of accelerating voltage.

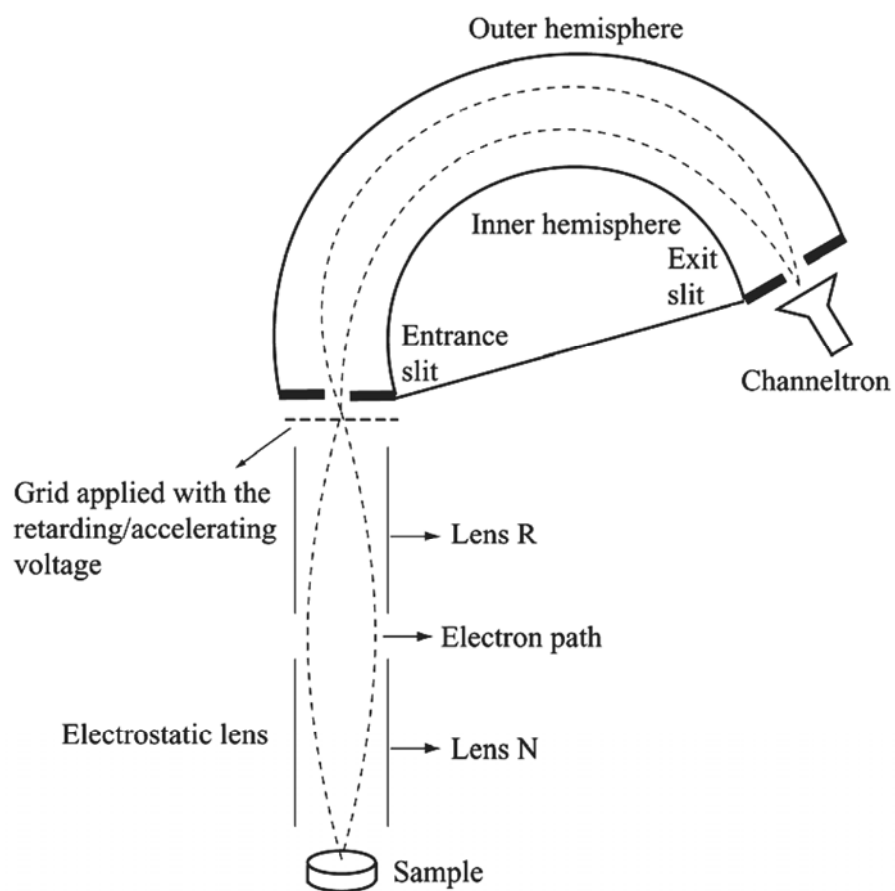


Fig. 3.8 Schematic diagram of CLAM2 with an electrostatic lens.

3.1.6 Electron Gun

In this work, electron guns are used as an electron source for the AES. The electron gun is LEG63 from Thermo VG Scientific (U.K.). The LEG63 is a medium resolution 5 keV electron source designed for pulse-counting Auger electron spectroscopy. The gun consists of a filament, grid, lenses, apertures, and scanning quadrupoles. The spot size is less than 50 μm at 10 nA. The recommended working distance is 60 mm.

For AES measurements, the sample is located just in front of the CLAM2 analyzer. A cone of Auger electrons emitted from the sample with appropriate kinetic energy pass through the entrance and exit slits of the analyzer when the potential difference is applied to the hemispheres. A channeltron located after the exit slit is used to detect the electrons. Electron-energy distributions can be obtained by slowly sweeping the analyzer deflection voltage of the hemispheres.

3.1.7 Ion Gun

The ion gun is an instrument for the sample cleaning by ion sputtering technique. The EX03 from Thermo VG Scientific (U.K.) was used in this thesis work. The gases species can be used for this model of ion gun are Ar, Ne, Kr, and Xe. Ar gas was selected for the sample cleaning processes. The energy of the gun can be varied between 300 eV to 3 keV. The Ar gas can be fed into the ion gun via a needle valve. The working distant is 100 mm but it can be in the range of 50-200 mm. The operating pressure should be less than 1×10^{-5} mbar.

3.1.8 Light Source: Synchrotron Radiation Source

Synchrotron light is an electromagnetic wave emitted from relativistic charged particles moving with a curve motion. A synchrotron light consists of two main parts, *i.e.*, the injection system and storage ring. The synchrotron light source used in this thesis work is the Siam Photon Light (SPL) source at the National Synchrotron Research Center (NSRC) of Thailand as shown in Fig. 3.9. The injection system produces a beam of electrons with energy up to 1.0 GeV and then injects into the storage ring. The machine parameters of the storage ring are shown in Table 3.3. The storage ring comprises of a series of magnet lattices which are designed to keep electrons circulating in the vacuum chambers of the storage ring. In the bending magnet, synchrotron light is emitted when electrons are experienced with the Lorentz force due to the presence of a dipole magnetic field perpendicular to the electron orbit.

Utilization of synchrotron in photoemission measurements expands the scope of many research fields. This is because of the special properties of synchrotron light together with the development of beamline instruments.

3.2 Sample Preparation

Since photoemission is a surface sensitive phenomenon, we have to prepare a clean well-defined surface in the photoemission experiments especially in case of semiconductor sample. The contamination of the surface of a solid material is brought about by impurity atoms or ions from the residual gas in the sample chamber or the impurity ions contained in the bulk material. The important impurity species are oxygen and carbon. The carbon originates in organic molecules in the residual gas.

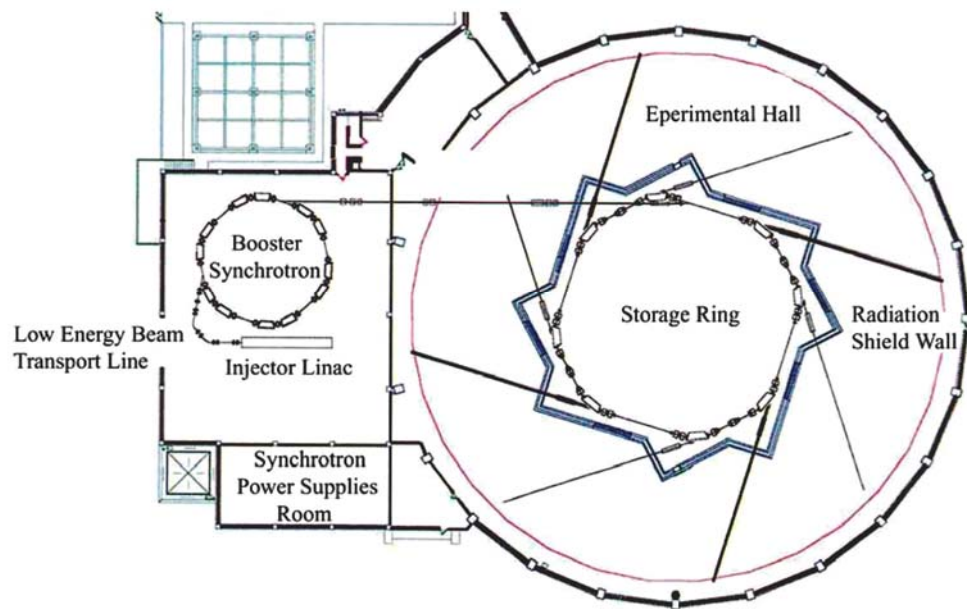


Fig. 3.9 The magnet arrangement of the storage ring of the Siam Photon Source.

Table 3.3 The machine parameters of the storages ring of the Siam Photon Source.

Parameters of storage ring	
Electron energy	1.0 GeV -1.2 GeV
Circumference	81.3 m
Stored beam current (nominal)	100.0 mA
Magnet lattice	Double Bend Achromat (DBA)
Superperiod	4
Length of straight section	5.2 m \times 4
Max RF voltage, V_{RF}	120 kV
RF frequency, f_{RF}	118 MHz
Harmonic number	32
Energy loss per turn	65.94 keV
Synchrotron oscillation frequency, f_s	13.5 kHz
Betatron tune, ν_x/ν_y	4.75/2.82

The preparation of the good sample is really essential to carry out the correct experiments. Therefore, in this section we describe some details of the sample preparation. The purity-type Si(001) substrate was first treated chemically with an RCA (Radio Corporation of America) (Kern and Puotinen, 1970) cleaning procedure ($\text{NH}_4\text{OH}:\text{H}_2\text{O}_2:\text{DI} = 1:1:5$, $\text{HF}:\text{DI} = 1:50$ and $\text{HCl}:\text{H}_2\text{O}_2:\text{DI} = 1:1:6$) to obtain a clean

protective oxide layer. After chemical cleaning, the sample was fixed to a molybdenum sample holder. The sample surface was further cleaned vacuum in the sample preparation chamber of the photoemission measurement system in the experimental station of the BL4 beamline.

To remove of foreign atoms contaminating the surfaces, the sample is heated at elevated temperature. Heating the specimen makes absorbed atoms come off by the thermal excitation. In ultrahigh vacuum it was thoroughly outgassed at $\sim 500^{\circ}\text{C}$ and then annealed at $\sim 850^{\circ}\text{C}$ for 10 min produced a sharp (2×1) two-domain LEED pattern and no impurities from AES spectra.

The $c(4\times 4)$ reconstruction is obtained, on clean $\text{Si}(001)-(2\times 1)$ wafers, by annealing at temperature between 580°C - 630°C , maintaining this temperature for 5 min, and then cooling down to room temperature, a $c(4\times 4)$ LEED pattern was shown.

3.3 Photoemission Measurements

The photoemission measurement was performed by using synchrotron radiation at BL4 beamline at the National Synchrotron Research Center (NSRC) of Thailand. The work function of the electron energy analyzers has been determined from gold spectra using He I radiation. The work functions were 4.27 and 4.30 eV for the CLAM2 and the ARUPS10, respectively. The procedure of photoemission measurement is as follows:

3.3.1 AIPES Measurements

AIPES EDC measurements were carried out with the set-up as shown in Fig. 3.10. The Si(001) sample was aligned in such a way that the electric vector of the incident light was parallel to the surface of the sample, *i.e.*, the light direction is perpendicular to the surface of the sample. The CLAM2 analyzer is fixed to the photoemission chamber at the angles of 50° and 40° with respect to the direction of the incident light in the horizontal and vertical directions, respectively.

EDC's were measured with the excitation photons with energy between 40-60 eV. The spectra were normalized to the incidence photon flux measured by the drain current of a gold mesh located between the sample and the rear focusing mirror of the beamline. The data acquisition system for AIPES measurement is a home-developed system (Samred Kantee, Supat Klinkhieo, and Prayoon Songsiriritthigul, 2005).

3.3.2 ARPES Measurements

The ARUPS10 analyzer was used for the ARPES measurements. The VGX900 data acquisition software provided by the maker of the analyzer, (VG Microtech, Computer Program, 1998) was used. The drain current of the Au mesh could not be measured, thus the current of the electron beam in the storage ring was used for the normalization EDC's instead.

For ARPES measurement, the accurate alignment of the sample and the analyzer with respect to the direction of the excitation photon beam is importance. The manipulator provides azimuthal and polar rotation of the sample, shown in Fig. 3.11. Accurate adjustment of the sample orientation can be obtained using the LEED pattern as instruction.

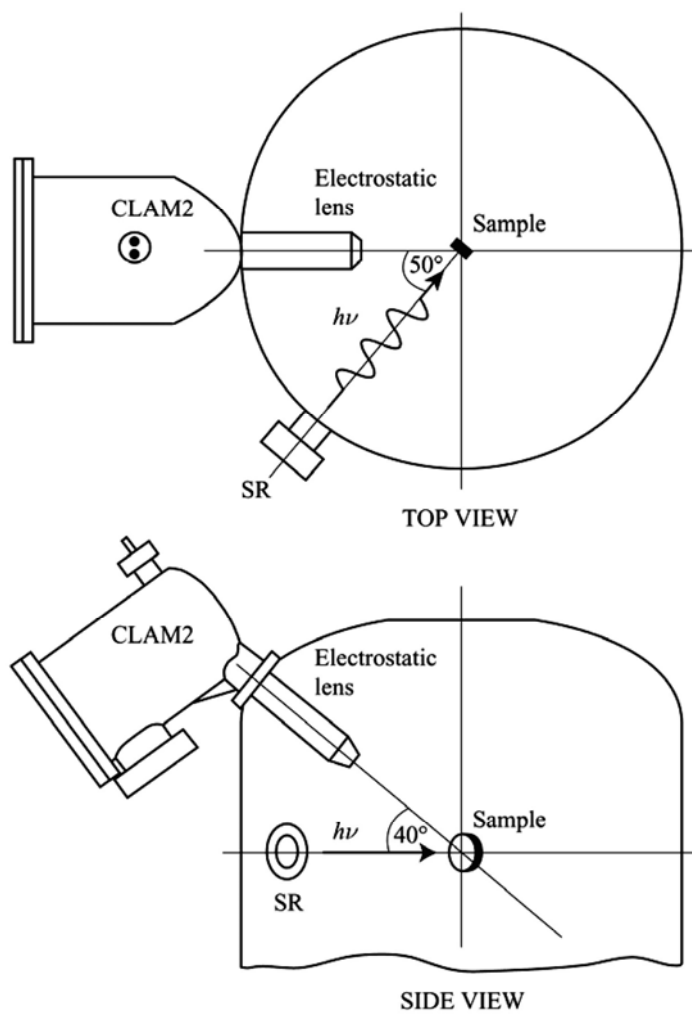


Fig. 3.10 Schematic diagram of AIPES measurements set-up.

This alignment allows simple measurement procedure to obtain EDC's along each symmetry line by one movement of the ARUPS10 analyzer. Photons with energy of 40 eV were used for the excitation in the EDC measurements.

The normal emissions ARPES were also performed. The sample was aligned with the angle of incidence of the photon beam of 45° with respect to the normal of the sample surface. The difference angle of incidence allowed polarization dependence of the sample to the excitation light to be studied.

In off-normal emission measurement, the surface band structure was mapped along $\Gamma - J_\beta - J'_\alpha$ directions of the surface Brillouin zone with the angles of emission (θ_e) between of 10° - 30° . The relation of the surface Brillouin zone is shown in Fig. 3.12.

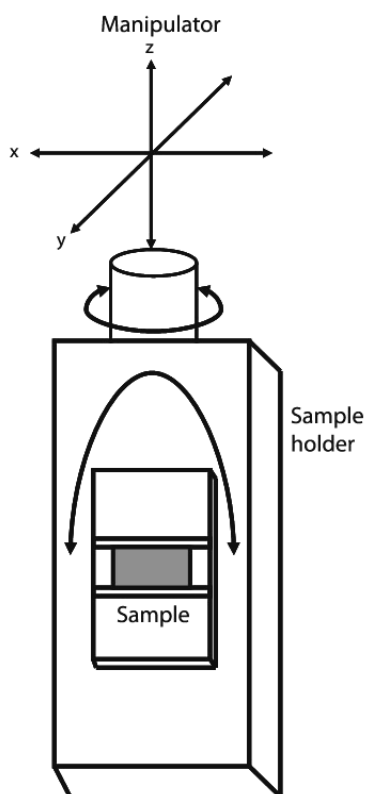


Fig. 3.11 Azimuthal and polar rotation and translation movement of the sample controlled by manipulator.

Si (100) (2×1) two-domain
surface Brillouin zones

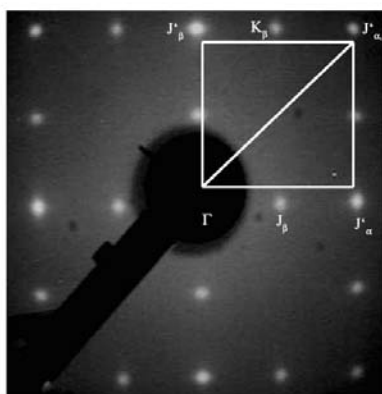
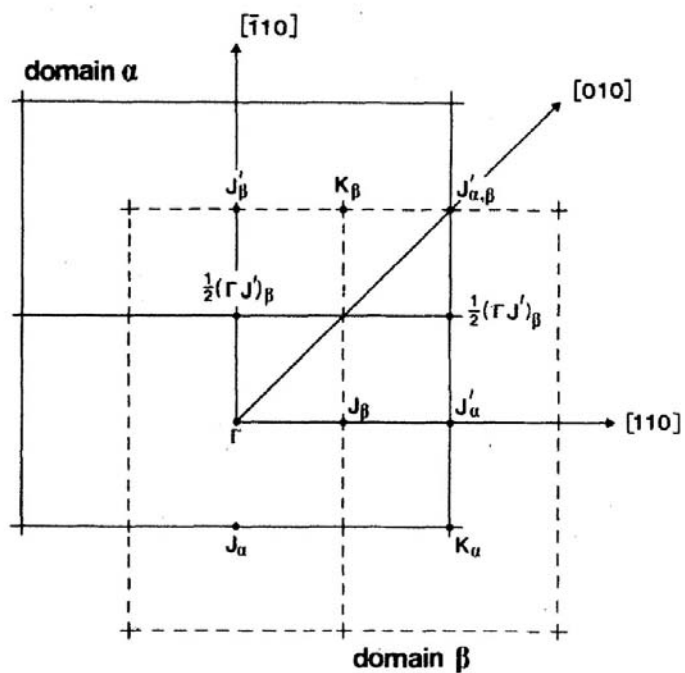


Fig. 3.12 Surface Brillouin zone of the two (2×1) reconstructed domains of the Si(001) surface. LEED pattern of the clean Si(001)-(2×1) surface is presented for comparison.

3.4 Calculations

3.4.1 Slab-Models for Surfaces

In the bulk calculations a unit cell was entered which was reproduced in all directions according to the periodic boundary conditions. The same concept can be used to generate a surface structure, with the trick to construct a supercell instead of the unit cell, which implicitly contains a surface. A simple supercell as shown in Fig. 3.13. Reproducing this kind of cell in all directions ends up in an alternating structure of slabs of silicon atoms and vacuum layers.

From the bottom to the top the structure of the supercell is the following:

It starts with several layers of silicon atoms corresponding to the bulk structure. Their positions are fixed; therefore the program is not allowed to move them in any direction. Since these atoms are far away from the surface, it can be assumed that they behave like atoms in the bulk and therefore this simplification is reasonable.

The following silicon layers in the supercell have the bulk unit cell set-up structure as well, with the difference that they are able to relax. Due to specific structure effects, these atoms will change their position compared to the bulk. Especially relaxations in the positive or negative direction perpendicular to the surface are expected.

The last part of the cell is a vacuum layer, thick enough to inhibit any interactions between the Si surface and the bulk atoms of the next supercell.

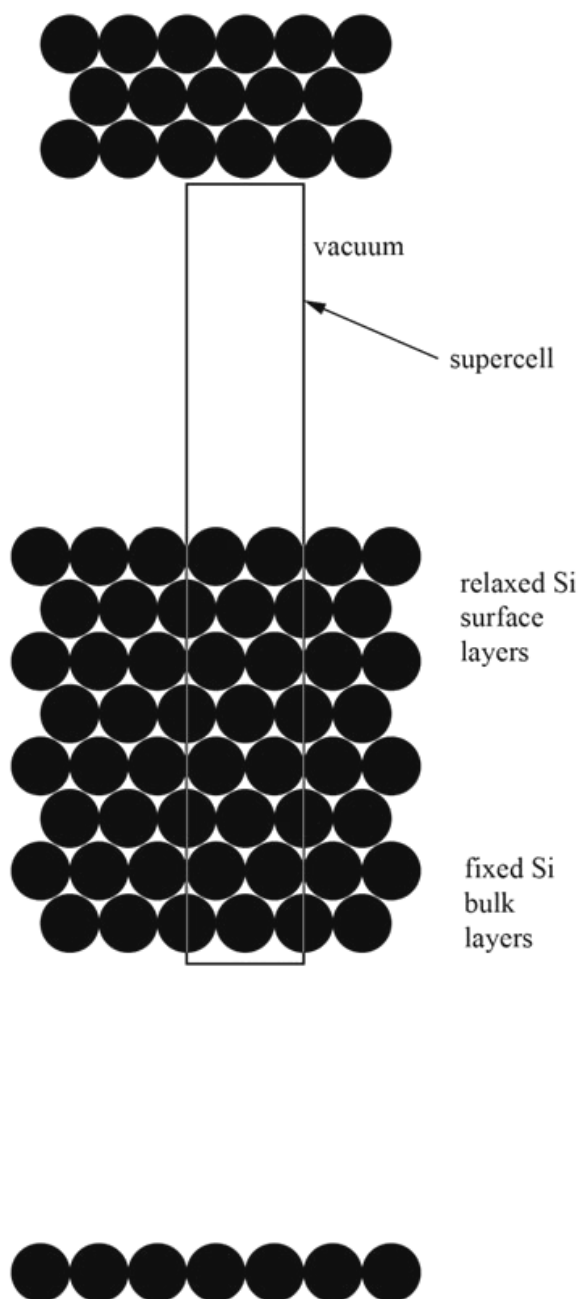


Fig. 3.13 A schematic diagram of a supercell used to model a silicon surface.

3.4.2 Computational Details

The first-principle calculations were performed using the commercial Vienna *ab initio* simulation package (VASP) code, based on density functional theory (DFT). The exchange and correlation energy and potential were calculated using the local-density approximation (LDA) functional. The cut-off energy of the plane waves is 290 eV, theoretical lattice constant of 5.39 Å, and ultrasoft pseudopotentials. To sample the Brillouin zone, k-point grids corresponds to $2 \times 2 \times 1$ k-points in the surface cell were used. The k-point mesh was generated by the automatic generation scheme according to Monkhorst and Pack.

3.4.2.1 Modeling of Si(001)-(2×1) Surface Reconstruction

The Si(001)-(2×1) surface was modeled by a repeated slab geometry, having ten layers of Si atoms and a terminating H layer at the bottom. The two Si layers above the H atoms is kept fixed during the simulation, with the positions of H chosen in such a way to mimic the bulk Si-Si bonds. The other eight Si layers are allowed to move. The repeated slabs are separated by 9.6 Å of vacuum.

3.4.2.2 Modeling of Si(001)-c(4×4) Surface Reconstruction

The dimerized Si(001)-p(2×2) surface was modeled by ten layer slab separated by 9.6 Å vacuum. The bottom surface was passivated by hydrogens. The Si atoms in the bottom two layers and the H atoms were fixed. We investigated a large number of configurations with $n = 1-6$ substitution carbon atoms located in surface or subsurface sites. Due to the relatively small thickness of our slab, we did not consider carbon incorporation below the fourth layer.

All configurations studied in this work have the $c(4 \times 4)$ periodicity. The configurations are named N, N being the number of C atoms in the $c(4 \times 4)$ unit cell. Five different models were considered with different amounts of carbon atoms incorporated in the Si lattice (Table 3.4).

The stability of the proposed models was examined by calculating the surface free energy $F(N)$ of the model N,

$$F(N) = E_{tot}(N) - n_{Si}(N)\mu_{Si} - n_C(N)\mu_C \quad (3.2)$$

where $E_{tot}(N)$ is the calculated total energy of configuration N, n_x and μ_x are the number of atoms and the chemical potential for atomic type X (X = Si or C), respectively. The values of the chemical potentials to start with are the cohesive energies per atom of the respective bulk crystal, $\mu_C = -7.37 \text{ eV}$ and $\mu_{Si} = -4.63 \text{ eV}$.

Since it is not possible to calculate the absolute surface energy for the Si(001) surface due to a lack of inversion symmetry, all calculated surface energies are given with respect to the pure Si(001) surface (configuration 0). Therefore we write the equation above as

$$F(N) = E_{tot}(N) - n_{Si}(N)\mu_{Si} - n_C(N)\mu_C - F(0) \quad (3.3)$$

Table 3.4 Occupation of surface and subsurface sites identified in Fig. 3.14 by silicon or carbon atoms.

Configuration (X)	Position of C atoms
1	1
2	1,11
3	2,5,11
4	1,4,5,11
5	7,8,9,10,11

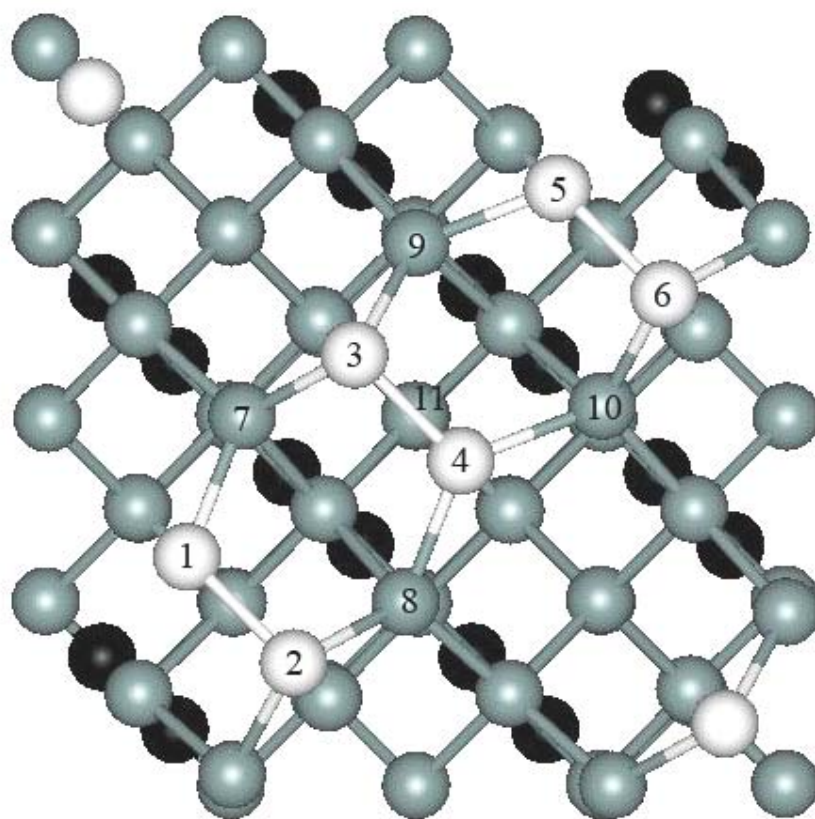


Fig. 3.14 Top view of a $c(4\times 4)$ unit cell of the dimer-reconstructed Si(001). Dimer atoms are shown in white. The numbers denote sites where C substitutes Si atoms in the configurations discussed in this work.

CHAPTER IV

RESULTS AND DISCUSSION

The various aspects of the experiments performed in this work and their results are described in the following sections. They can be grouped into the preliminary sample preparation procedures, experiments, calculations and the analysis of the results.

4.1 Surface Reconstruction

4.1.1 Preparation of Si(001)-(2×1) Surface

Fig. 4.1 shows AES spectra taken from the Si(001) sample before and after cleaning by RCA cleaning and heating. The main impurities on the surface were carbon and oxygen atoms as shown in Fig. 4.1a. The LVV Si spectrum measured on the clean surface is shown in Fig. 4.1b.

The clean and well-defined (001) surface was also confirmed by LEED measurements. The LEED pattern reflects the atomic arrangement of the surface. If the surface is contaminated, we cannot obtain a clear diffraction pattern. Therefore, the LEED pattern also makes the good indication of the perfectness of the surface. Fig. 4.2 shows the LEED patterns of the contaminated and clean Si(001)-(2×1) surface.

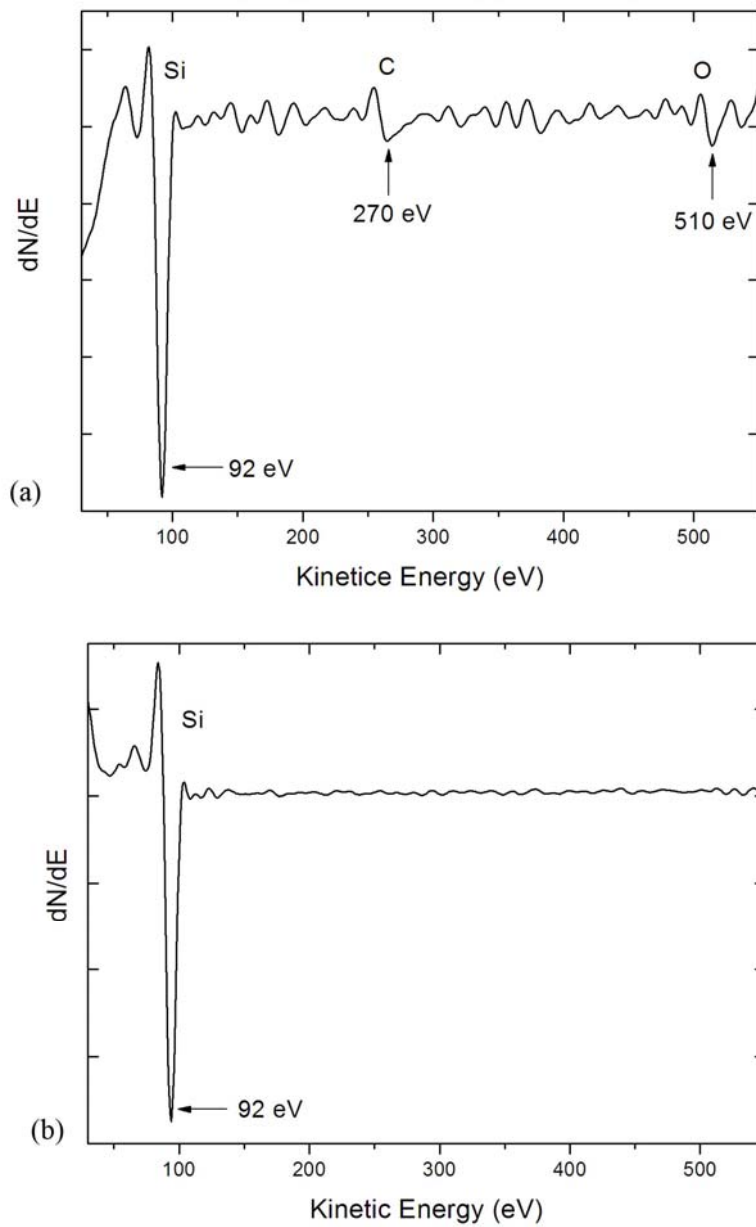
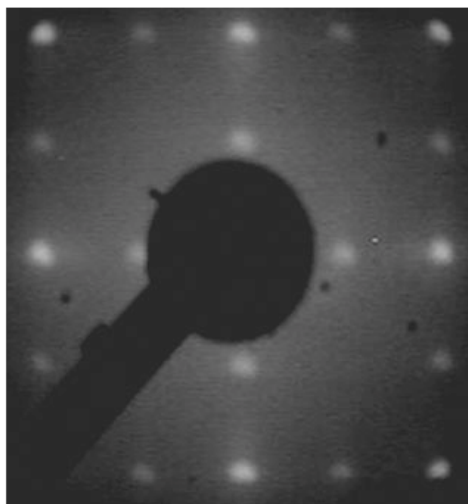
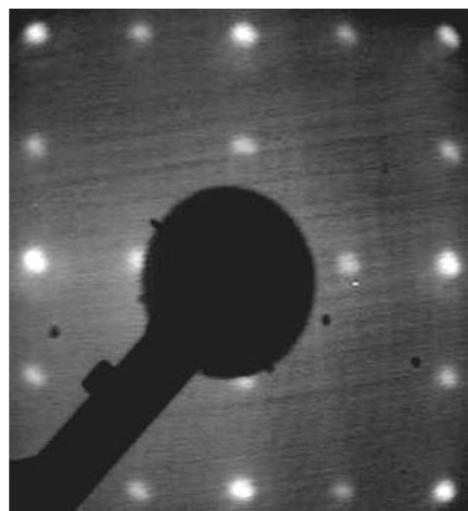


Fig. 4.1 Auger spectrum from LVV Si in differential spectrum. (a) Contaminated surface and (b) Clean surface.



(a)



(b)

Fig. 4.2 (2×1) low energy electron diffraction (LEED) pattern of Si(001) surface.

(a) Contaminated surface. (b) Clean well-defined surface. $E_p = 60$ eV.

4.1.2 Preparation of Si(001)-c(4×4) Surface

After annealing a Si(001) sample with a well established (2×1) surface reconstruction at 630°C for 5 minutes at a background pressure of 2×10^{-9} mbar, patches of the c(4×4) reconstruction appear. The transformation between the (2×1) and c(4×4) reconstructions has been observed by AES and LEED. Starting from a (2×1) reconstructed Si(001) surface then annealing at 630°C the (n/4) streaks appear in the LEED (Fig. 4.3). Upon heating the sample above 630°C the (n/4) streaks in the LEED pattern disappear and the (2×1) reconstruction appear (Fig. 4.4).

Fig. 4.5 shows an AES spectrum where a small carbon peak develops at 630°C, which confirms that the c(4×4) surface reconstruction is related to carbon. The appearance of the carbon peak in AES coincides with the onset of (n/4) streaks of c(4×4) spots in LEED. It can be ruled out that the c(4×4) reconstruction is caused by regular carbon arrangement in the top layer. A rough estimation of the carbon contents from the peak heights of the AES spectra gives a carbon content of only a few percent.

In the experiments, some phenomena have been found:

- (1) The crucial step for obtaining the c(4×4) pattern is maintaining the sample at a relatively narrow temperature range, i.e., from 580°C-630°C, for 5 min.
- (2) The transition between c(4×4) and (2×1) is reversible. The c(4×4) can convert into (2×1) if the sample is heated to above 630°C. The transition from (2×1) to c(4×4) can occur by thermal annealing between 580°C-630°C.
- (3) The LEED spots of (2×1) coincide with the integral and half-order spots of c(4×4) structure exists in the form of small domains accompanied by the (2×1) structure on the remaining portions of surface.

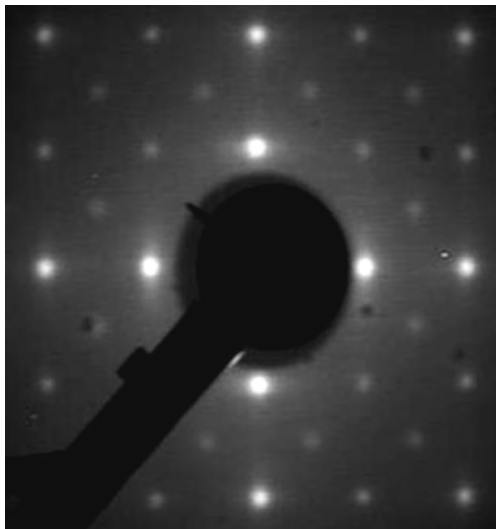


Fig. 4.3 LEED pattern obtained at 65 eV from Si(001)-c(4×4) by annealing at 630°C for 5 minutes.

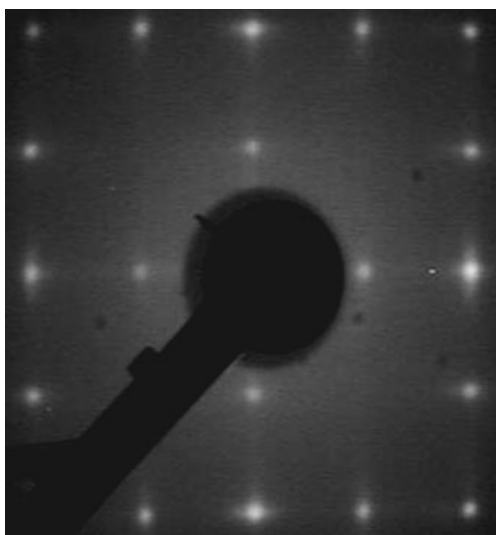


Fig. 4.4 LEED pattern obtained at 50 eV from Si(001)-(2×1) by annealing at 670°C for 5 minutes.

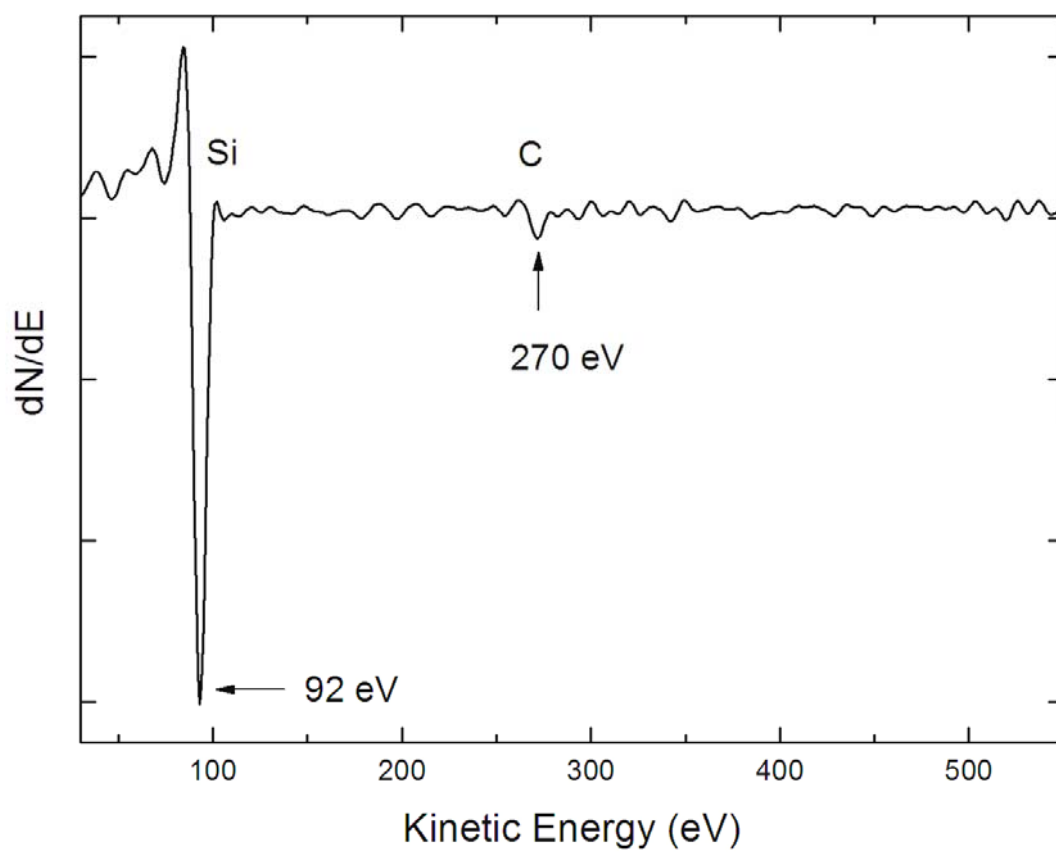


Fig. 4.5 Auger spectrum of Si(001)-(2×1) with a small carbon peak at around 270 eV has been taken after annealing at 630°C for 5 min.

4.2 The Density of States (DOS)

4.2.1 The Si(001)-(2×1) Surface

The valence band angle-integrated photoemission spectra for Si(001)-(2×1) are shown in Fig. 4.6 for two photon energies, $h\nu = 40$ eV and 60 eV. The abscissa represents the binding energy of emitted electrons and the ordinate the electron intensity. The features in the spectra are indicated by vertical bars. The experimental data contain significant contributions due to surface states over the entire ~ 12 eV width of the valence band. An approximate separation of the raw data into bulk and surface contributions results in a significantly improved bulk “density of states” as well as the identification by photoemission of additional surface states. The surfaces exhibited photoemission spectra surface state peaks at 0.58 and 0.78 eV binding energy below E_F for $h\nu = 40$ and 60 eV, respectively. This peak is sensitive to gas adsorption. The others features indicated by arrow heads are contributions from bulk related to the density of states.

To make the mentioned narrowing of the surface DOS visible, a layer resolved local DOS for eight layers was plotted comparison with experiment in Fig. 4.7 together with the one for the bulk. When comparing the calculated the DOS for the surface with photoemission results, the main peak A denoted the surface state close to calculation is found. The photoemission data at peaks B and C seem to agree with the DOS in deep layer rather than the surface DOS. The somewhat improved agreement we obtain between the surface-region density of states and the photoemission spectrum is believed due primarily to the inclusion of more bulklike layers in the volume over which this quantity is integrated in the present calculation. These yield a better approximation to the escape-depth weighting of bulk and surface contributions.

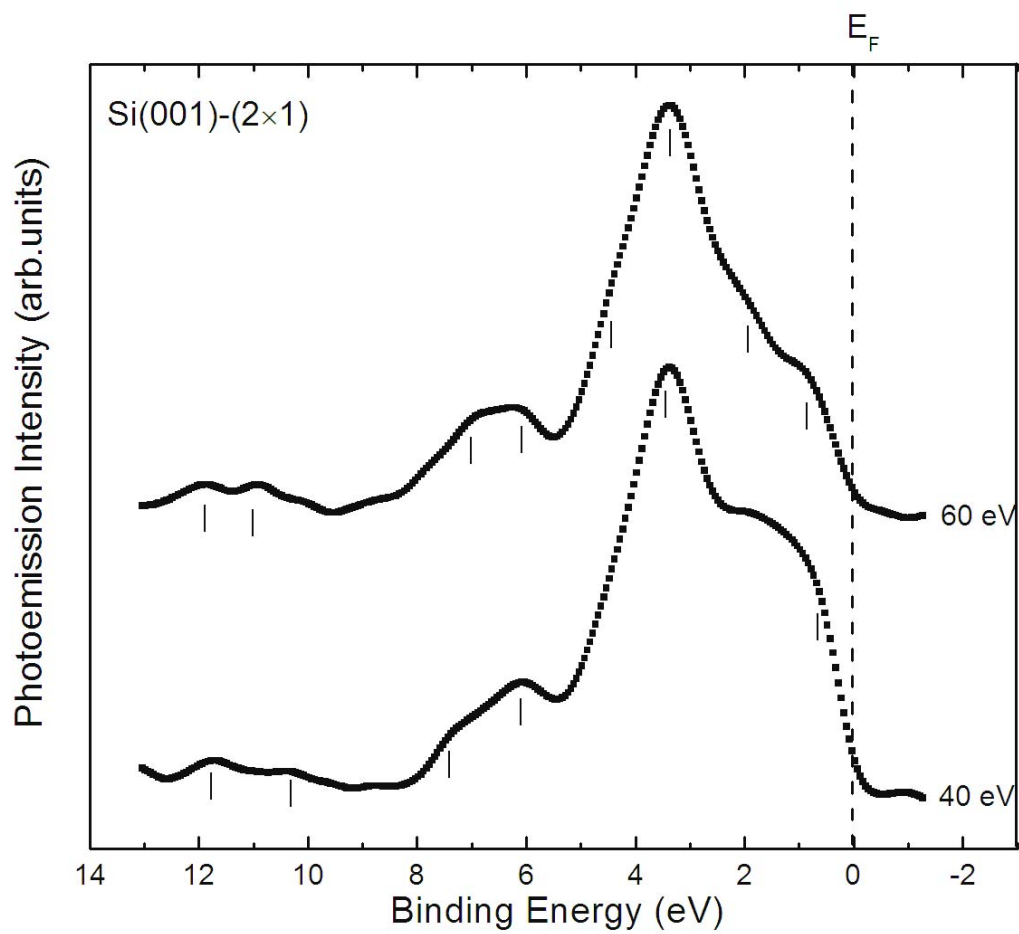


Fig. 4.6 EDC's showing the change in the spectral shapes of Si(001)-(2x1) the valence band as the excitation photon energy is changed. Vertical bars indicate major features in the spectrum.

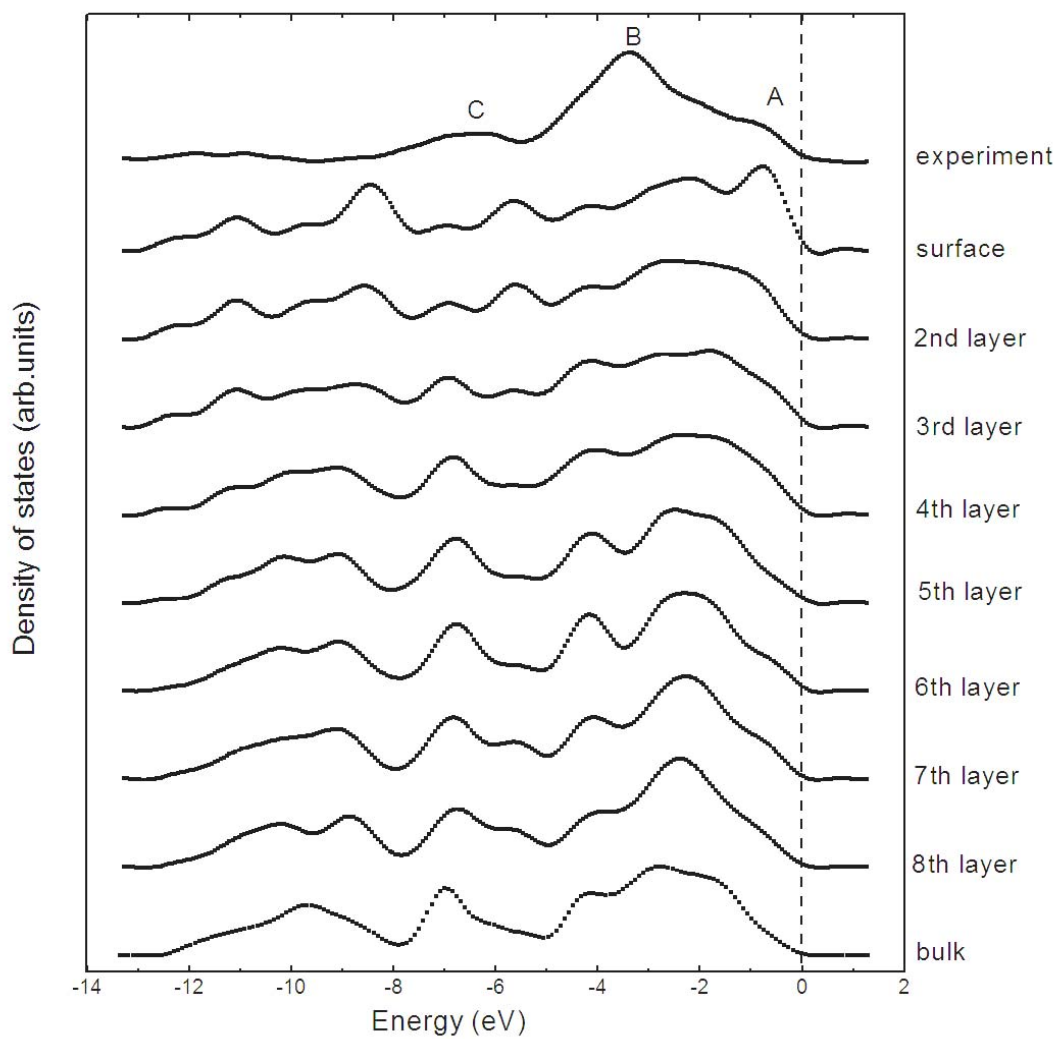


Fig. 4.7 Calculated density of states compared to $h\nu = 60$ eV photoelectron energy distribution for Si(001)-(2 \times 1).

4.2.2 The Si(001)-c(4×4) Surface

Fig. 4.8 are shown the angle-integrated spectra for the c(4×4) surfaces for two photon energies, $h\nu = 40$ eV and 60 eV. The abscissa represents the binding energy of emitted electrons and the ordinate the electron intensity. The features in the spectra are indicated by vertical bars. We can observed the surface state peak at position 0.53 and 0.73 eV binding energy below E_F for $h\nu = 40$ and 60 eV, respectively. When compare with the (2×1) reconstruction the surface state shift toward the low binding energy. The features near 2.0 and 3.3 eV binding energy below E_F for $h\nu = 40$, which may account for the c(4×4) dimer dangling bond and dimer bond signatures, respectively (Simon et al., 2001). This feature cannot be seen clearly for the (2×1) reconstruction.

Structural properties and energetics

The relaxed geometries for all six configurations described in Chapter III are shown in Fig. 4.9, where μ_C is taken as the energy of a C atom in diamond. Their relative energies are given in Table 4.1. We compare cells of different C content, discussing the dependence of the energies on C chemical potential.

The calculated dimer bond length for configuration 0 is 2.32 Å. The bonds between the dimer atoms and the second layer atoms are 2.36 Å. In model 1, it contains single C atom at the first layer. The C-Si dimer bond is 1.78 Å. The Si-Si dimer neighboring the Si-C dimer is shorter, its length being 2.28 Å. The other Si-Si dimer have same length as the dimers on pure Si(001). In model 2, one C atom is at the surface and the other is incorporated in layers 4 under the dimer rows. The C atom in the forth layer forms four bonds of lengths 1.93, 1.94, 1.96 and 1.96 Å. In model 3, two C atom forms Si-C dimer and one C atom in the fourth layer. In model 4, three C

atom forms Si-C dimer and one C atom in the fourth layer. Finally, model 5 (Remediakis et al., 2004) contains four C atoms at second layer, forming a small SiC cluster below a Si-Si dimer and the other C atom in the fourth layer. The C atoms lying between the two dimers that have come close to each other form bonds of lengths between 1.87 and 1.97 Å, with angles between 115° and 128°; apparently, they are in a close sp^2 hybridized state with the surrounding Si atoms. The arrangement of C atoms is thus qualitatively different from that of bulk SiC, where π bonding is absent.

To compare configurations with different C content, we use eq (3.3). This implies that the surface is in equilibrium with a reservoir of C atoms small clusters, whose cohesive energies are in the range from 0 and -7.37 eV. These limits correspond to two extreme situations: In the first, the atomic reservoir for carbon atoms is a gas of free carbon atoms; in the second, the atomic reservoir is bulk diamond or graphite. In Fig. 4.10, we show the energies of all configurations as a function of μ_C . We observe that the first transition happens for $\mu_C = -7.37$ eV. From this point, model 4 is the energetically favorable one, up to $\mu_C \approx -6.2$ eV where model 5 becomes the one having the lowest energy.

Table 4.1 Relative energies for the various configurations considered according to eq (3.3) in eV per c(4×4) cell.

Configuration (X)	Relative Energy
0	0.00
1	0.77
2	1.66
3	2.70
4	3.33
5	2.14

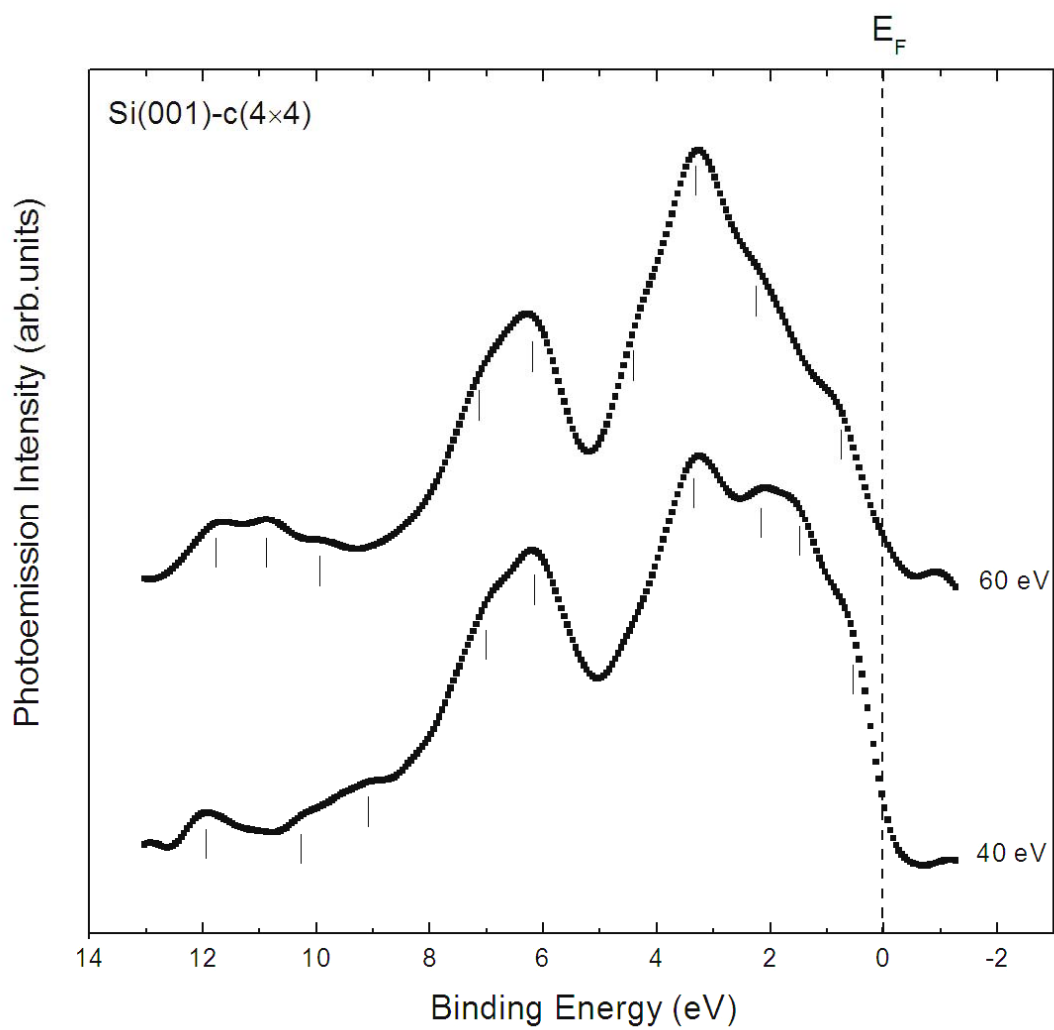


Fig. 4.8 EDC's showing the change in the spectral shapes of Si(001)-c(4x4) the valence band as the excitation photon energy is changed. Vertical bars indicate major features in the spectrum.

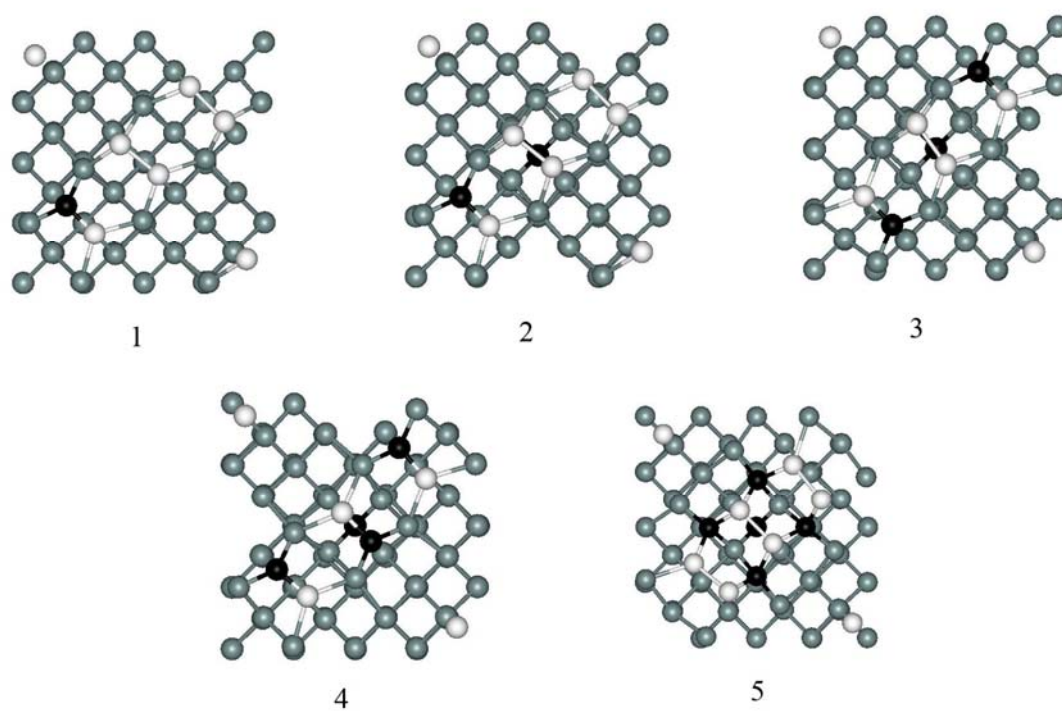


Fig. 4.9 Relaxed geometries (top views) of the configurations discussed in Chapter III. Si surface atoms are shown as grey spheres; Si dimer atoms are shown as white spheres, and C atoms are represented by black spheres.

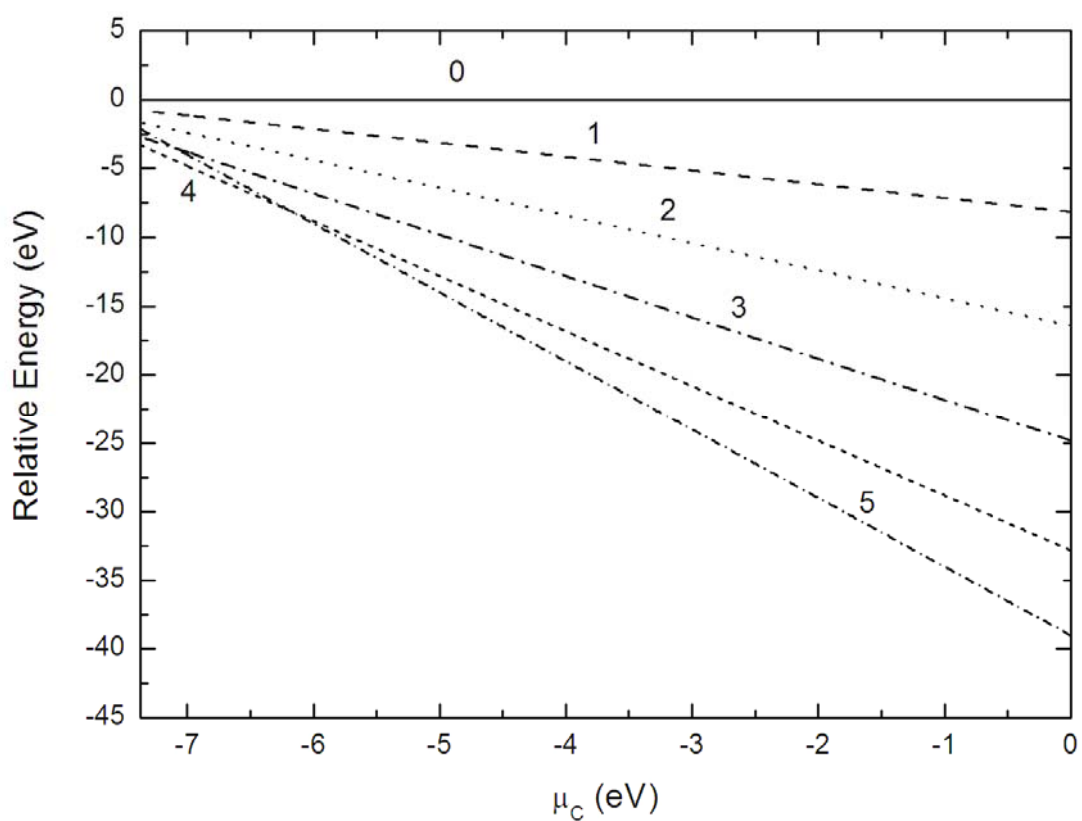


Fig. 4.10 Relative surface energies of the considered structures as a function of the C chemical potential, as derived from the *ab initio* calculations at absolute temperature. Energies are given in eV per $c(4\times 4)$ unit cell.

4.3 Angle-Resolved Photoemission (ARPES)

4.3.1 The Si(001)-(2×1) Surface

In Fig. 4.11 we show angle-resolved photoemission spectra for the Si(001)-(2×1) reconstructed surface measured along $\bar{\Gamma}-\bar{J}$ line of the surface Brillouin zone. The excitation energy was 40 eV with incidence angle of 45°. The abscissa represents binding energy while the ordinate represents photoemission intensity in arbitrary units. The emission angles were varied between 0° and 30°. The features in the spectrum are indicated by alphabetic notations A through D. Peak A exists just below E_F , the location is 0.55 eV below E_F for $\theta_e = 0^\circ$ disperses downwards to 0.65 eV below E_F for $\theta_e = 30^\circ$ ($k_{||} \sim 1.5 \text{ \AA}^{-1}$), while $k_{||}$ for the J'_α symmetry point equal to 0.82 \AA^{-1} . In calculating $k_{||}$ we have used the value of 4.3 eV for the work function. Structure A is the well-known surface state associated with the dangling bonds on the (2×1) reconstructed surface. Structures B, C and D are the spectra are regarded as due to bulk emission.

In Fig. 4.12 we have plotted the surface bands energy as given by the first-principle calculation in the local density approximation for the asymmetric dimer model. It gives rise to two distinctly different dangling bond states D_{up} and D_{down} . The buckling lowers the energy of the D_{up} state and lifts the energy of D_{down} state. Since D_{up} is occupied and D_{down} is empty, this energetic lowering of D_{up} leads to a lowering of the total energy.

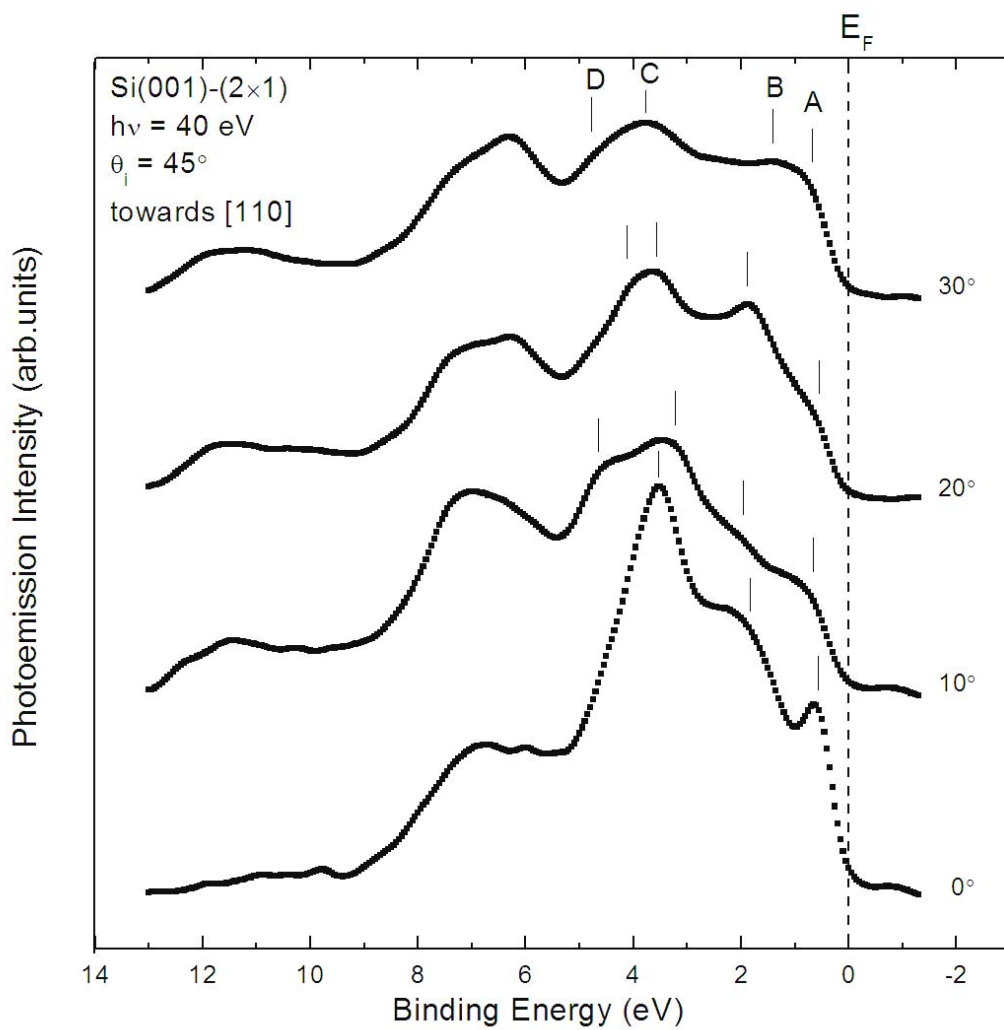


Fig. 4.11 Angle-resolved photoemission spectra of Si(001)-(2x1) for angles of electron emission between 0° and 30°. \vec{k}_\parallel for emitted electrons is directed along the [110] azimuthal direction.

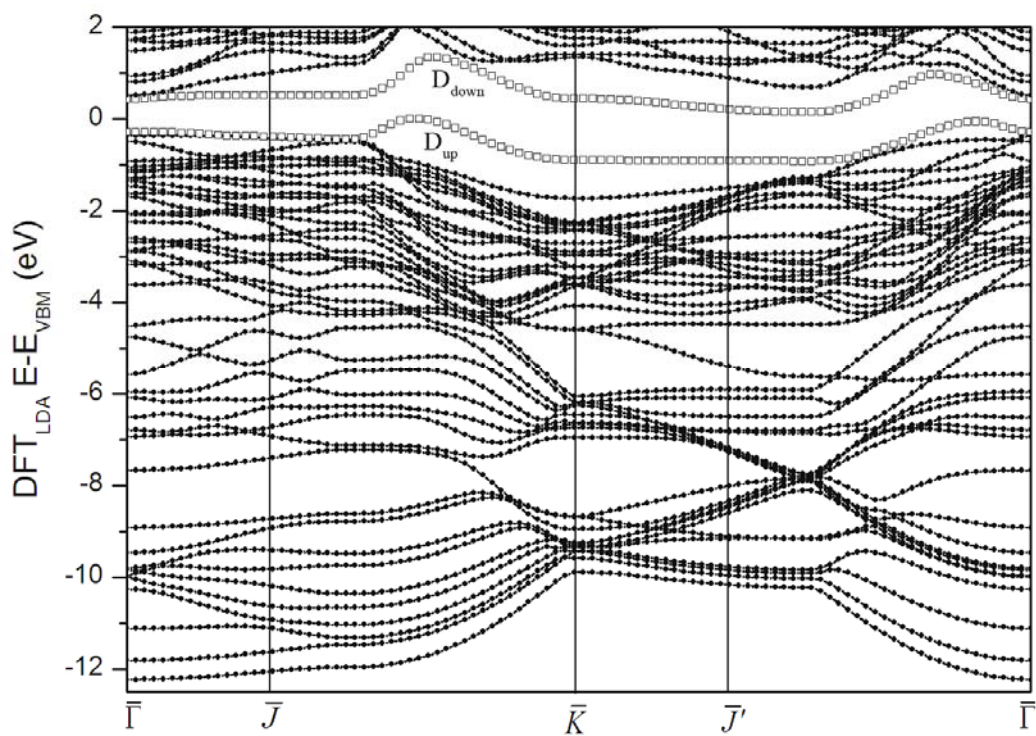


Fig. 4.12 Calculated surface band structure of Si(001)-(2x1).

4.3.2 The Si(001)-c(4×4) Surface

In Fig. 4.13, the spectra measured on the c(4×4) surface are shown. The spectra were measured along $\bar{\Gamma} - \bar{J}$ line or [110] direction of the surface Brillouin zone. The emission angles were varied between 0° and 30°. Excitation light is incident at an angle of 45°. In case of normal emission, c(4×4) reconstructed surface show prominent feature at 1.7 eV binding energy below E_F , which are not clear for the (2×1) reconstructed surface. The contribution from the emission angle is 10°, seems to be resolved in two features in the region below 3 eV binding energy below E_F , which difference is found in the spectra of the (2×1) reconstructed surface. The spectra were obtained with an emission angle 20°, the spectrum near 4 eV shift toward low binding energy when comparing to (2×1) reconstructed surface. Finally, the contribution for emission angle 30° we observed the new features at around 1.7 and 4.6 eV. The new features is not found in the (2×1) reconstructed surface.

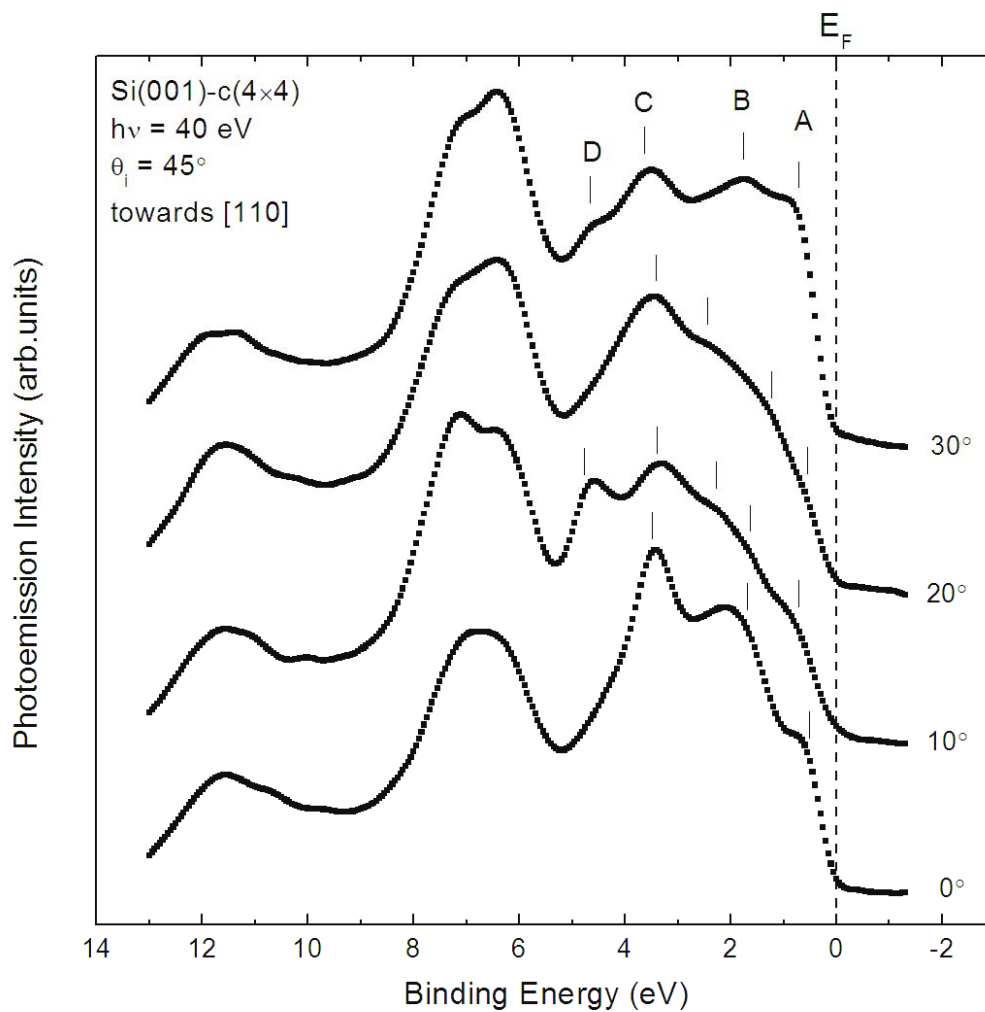


Fig. 4.13 Angle-resolved photoemission spectra of Si(001)-c(4×4) for angles of electron emission between 0° and 30°. $\vec{k}_{||}$ for emitted electrons is directed along the [110] azimuthal direction.

CHAPTER V

CONCLUSION

The findings of this thesis work can be summarized as follow:

- The $c(4\times 4)$ reconstruction has been investigated by means of experimental techniques probing both electronic and crystallographic structures and by *ab initio* calculations.
- The $c(4\times 4)$ surface can be obtained by heating $\text{Si}(001)-(2\times 1)$ surface at temperature between 580°C - 630°C . The transition between (2×1) and $c(4\times 4)$ is reversible. The transition from (2×1) to $c(4\times 4)$ can occur by thermal annealing between 580°C - 630°C . The $c(4\times 4)$ can convert into (2×1) if the sample is heated to above 630°C .
- The LEED spots of (2×1) coincide with the integral and half-order spots of $c(4\times 4)$ structure exists in the form of small domains accompanied by the (2×1) structure on the remaining portions of surface.
- The AES spectra shown a small carbon peak develops at 630°C , which confirms that the $c(4\times 4)$ reconstruction is related to carbon.
- In all angle-integrated spectrum for the (2×1) and $c(4\times 4)$ surface, clear difference of the spectral shape is found between the data obtained with excitations at 40 eV and those at 60 eV.
- The measured angle-integrated spectral shape of the $c(4\times 4)$ reconstructed surface with excitation energy at 40 eV shows the feature near 2.0 eV below E_F seem

to be resolved in two features, as expected for the presence at the surface of both Si-Si and Si-C dimers.

- *Ab initio* calculations show that the model 4, characterized by arrangement of three Si-C dimers at surface layer and one C atom in the fourth layer is the favored structure in the range of C chemical potential from -7.37 eV up to -6.2 eV where the model 5, characterized by arrangement of C atoms at second nearest-neighbor distances, becomes the one having the lowest energy.

- The measured angle-resolved spectral shape of the (2×1) surface, the surface state peak near 0.6 eV below E_F is observed.

- In the angle-resolved photoemission spectral shape of the c(4×4) reconstructed surface shows the new features appear in the photoemission spectra near 1.7 and 4.6 eV below E_F . The new features is not found in the (2×1) reconstructed surface.

REFERENCES

REFERENCES

- Blöchl, P. E. (1994). Projector augmented-wave method. **Phys. Rev. B** 50 (24): 17953-17979.
- Cardona, M., and Pollak, F.H. (1966). Energy-band structure of Germanium and Silicon: The k-p Method. **Phys. Rev.** 142 (2): 530-543.
- Chan, C. T., Vanderbilt, D., and Louie, S. G. (1986). Application of a general self-consistency scheme in the linear combination of atomic orbitals formalism to the electronic and structural properties of Si and W. **Phys. Rev. B** 33 (4): 2455-2464.
- Chelikowsky, J. R., and Cohen, M. L. (1976). Nonlocal pseudopotential calculations for the electronic structure of eleven diamond and zinc-blende semiconductors. **Phys. Rev. B** 14 (2): 556-582.
- Feuerbacher, B., and Willis, R. F. (1976). Photoemission and electron states at clean surfaces. **J. Phys. C: Solid State Phys.** 9: 169-216.
- Grobman, W. D., and Eastman, D. E. (1972). Photoemission valence-band densities of states for Si, Ge, and GaAs using synchrotron radiation. **Phys. Rev. Lett.** 29 (22): 1508-1512.
- Hamann, D. R., Schlüter, M., and Chiang, C. (1979). Norm-conserving pseudopotentials. **Phys. Rev. Lett.** 43 (20): 1494-1497.
- Hohenberg, P., and Kohn, W. (1964). Inhomogeneous electron gas. **Phys. Rev.** 136 (3B): 864-871.
- Hüfner, S. (1996). **Photoelectron spectroscopy** (2nd ed). Berlin: Springer-Verlag.

- Ishii, T. (1989). Solid state spectroscopy in the vacuum ultraviolet and soft x-ray region. In H. Winick, D. Xian, Ming-han Ye and T. Huang (eds). **Applications of synchrotron radiation** (pp 371-514). New York: Gordon and Breach Science Publishers.
- Jemander, S. T., Zhang, H. M., Uhrberg, R. I. G., and Hansson, G. V. (2002). STM study of the C-induced Si(100)-c(4×4) reconstruction. **Phys. Rev. B** 65 (11): 115321-115328.
- Kern, W., and Puotinen, D. A. (1970). Cleaning solutions based on hydrogen peroxide for use in silicon semiconductor technology. **RCA Rev.** 31: 187-206.
- Kittel, C. (1996). **Introduction to Solid State Physics** (7th ed). USA: John Willey & Sons, Inc.
- Kohn, W., and Sham, L. J. (1965). Self-consistent equations including exchange and correlation effects. **Phys. Rev.** 140 (4A): 1133-1138.
- Kresse, G., and Furthmüller, J. (1996). Efficient iterative schemes for *ab initio* total-energy calculations using a plane-wave basis set. **Phys. Rev. B** 54 (16): 11169-11186.
- Krüger, P., and Pollmann, J. (1993). Ab initio calculations of Si, As, S, Se, and Cl adsorption on Si(001) surfaces. **Phys. Rev. B** 47 (4): 1898-1910.
- Krüger, P., and Pollmann, J. (1995). Dimer reconstruction of Diamond, Si, and Ge(001) surfaces. **Phys. Rev. Lett.** 74 (7): 1155-1158.
- Miki, K., Sakamoto, K., and Sakamoto, T. (1997). Is the c(4×4) reconstruction of Si(001) associated with the presence of carbon? **Appl. Phys. Lett.** 71 (22): 3266-3268.

- Perdew, J. P., and Wang, Y. (1986). Accurate and simple density functional for the electronic exchange energy: Generalized gradient approximation. **Phys. Rev. B** 33 (12): 8800-8802.
- Ramstad, A., Brocks, G., and Kelly, P. J. (1995). Theoretical study of the Si(100) surface reconstruction. **Phys. Rev. B** 51 (20): 14504-14523.
- Remediakis, I. N., Guedj, C., Kelires, P. C., Grützmacher, D., and Kaxiras, E. (2004). Modeling of the carbon-rich c(4×4) reconstruction on Si(100). **Surf. Sci.** 554 : 90-102.
- Rohlfing, M., Krüger, P., and Pollmann, J. (1993). Quasiparticle band-structure calculations for C, Si, Ge, GaAs, and SiC using Gaussian-orbital basis sets. **Phys. Rev. B** 48 (24): 17791-17805.
- Samred Kantee, Supat Klinkhieo, and Prayoon Songsiriritthigul (2005). Data acquisition system for the angle-integral photoemission system at the Siam Photon Laboratory. **Suranaree J. Sci. Technol.** 12 (3): 223-230.
- Simon, L., et al. (2001). Atomic structure of carbon-induced Si(001)-c(4×4) reconstruction as a Si-Si homodimer and C-Si heterodimer network. **Phys. Rev. B** 64 (3): 035306-035314.
- Topp, W. C., and Hopfield, J. J. (1973). Chemically motivated pseudopotential for Sodium. **Phys. Rev. B** 7 (4): 1295-1303.
- Uhrberg, R. I. G., Hansson, G. V., Nicholls, J. M., and Flodström, S. A. (1981). Experimental studies of the dangling- and dimer-bond-related surface electron bands on Si(100) (2×1). **Phys. Rev. B** 24 (8): 4684-4691.
- Vanderbilt, D. (1990). Soft self-consistent pseudopotentials in a generalized eigenvalue formalism. **Phys. Rev. B** 41 (11): 7892-7895.

CURRICULUM VITAE

Miss. Ratchadaphon Sabrueangnet

Date of birth: 20 August 1981

Place of birth: Bangkok, Thailand

Nationality: Thai

Education

Academic year

1999-2002 Khon Kaen University, Khon Kaen, Thailand.

Bachelor of Science (Physics)

2004-2006 Suranaree University of Technology, Nakhon Ratchasima,
Thailand.

Master of Science (Physics)

Academic Experience

2003 Research Assistant, National Metal and Materials Technology
Center, Thailand Science Park, Pathumthani, Thailand.